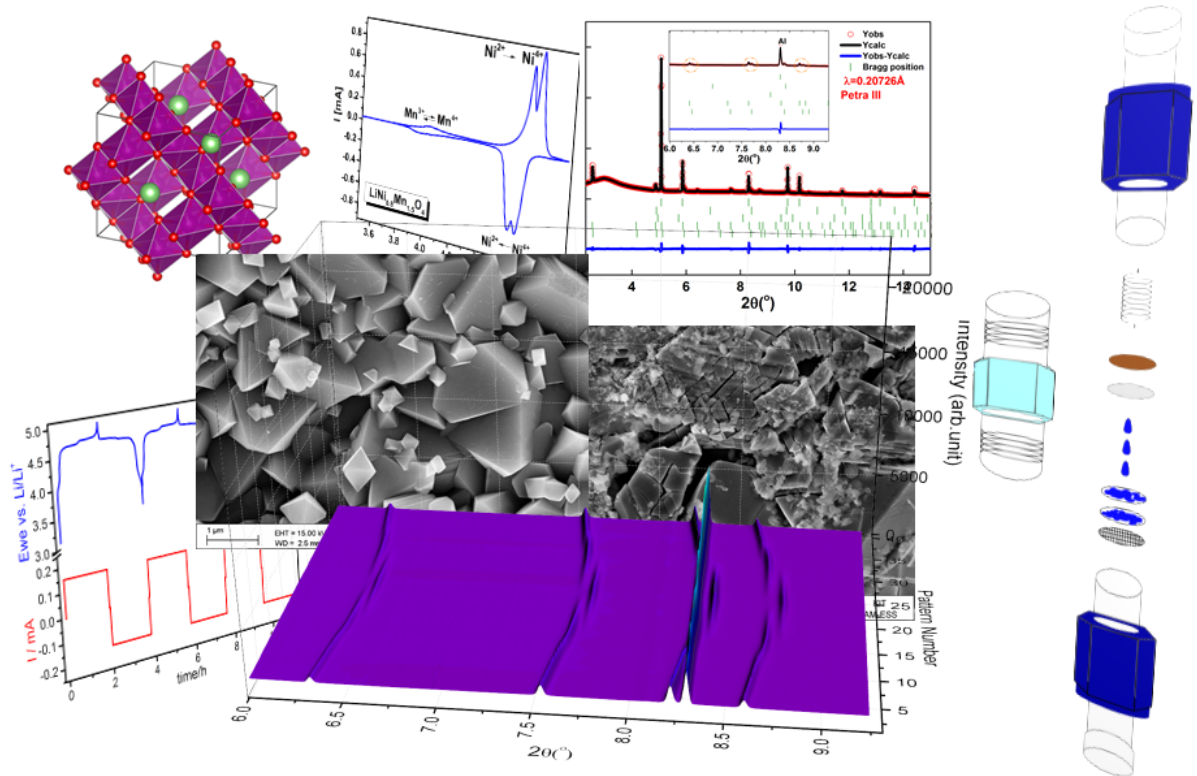# Influence of M-doping (M= Ru, Fe, La, Nd, Sm) on the Performance of Lithium Nickel-Manganese Spinels as High-Voltage Cathode Materials for Lithium Ion Batteries

PhD Dissertation

Nilüfer KIZILTAŞ-YAVUZ

Einfluss von M-Dotierung (M = Ru, Fe, La, Nd, Sm) auf die Leistung der Lithium Nickel-Mangan Spinelle als Hochspannungskathodenmaterialien für Lithium Ionen Batterien

Zur Erlangung des akademischen Grades eines

DOKTORS DER NATURWISSENSCHAFTEN

(Dr. rer. nat.)

Fakultät für Chemie und Biowissenschaften

Karlsruher Institut für Technologie (KIT) - Universitätsbereich

genehmigte

DISSERTATION

von

M. Sc. Nilüfer KIZILTAŞ-YAVUZ

aus

Ankara, TURKEI

Dekan: Prof. Dr. Peter ROESKY

Referent: Prof. Dr. Helmut EHRENBERG

Korreferent: Prof. Dr. Rüdiger-A. EICHEL

Tag der mündlichen Prüfung: 16/04/2015

KARLSRUHE INSTITUTE OF TECHNOLOGY

FACULTY OF CHEMISTRY AND BIOSCIENCES - INSTITUTE OF INORGANIC CHEMISTRY

INSTITUTE OF APPLIED MATERIALS (IAM) - INSTITUTE OF ENERGY STORAGE SYSTEMS (ESS)

Influence of M- doping (M= Ru, Fe, La, Nd, Sm) on the Performance of Lithium Nickel-Manganese Spinels as High-Voltage Cathode Materials for Lithium Ion Batteries

Submitted by:

Nilüfer

KIZILTAŞ-YAVUZ

Date of Oral Exam : 16/04/2015

Referee:

Prof. Dr. Helmut EHRENBERG

Co-referee:

Prof. Dr. Rüdiger-A. EICHEL

Karlsruhe, 2015

Contents

Abbreviations, Constants, Symbols

a	Ratio of the activities of products and reactants
BET	Brunauer-Emmett-Teller surface analysis technique
C-rate	Charge-discharge rate
CV	Cyclic Voltammetry
dE	First derivative of voltage of working electrode
DMC	Dimethyl carbonate
DSC	Differential Scanning Calorimetry
dQ	First derivative of specific capacity
e	Charge of one electron
$\mathbf{E}^{\circ}$	Standard electrode potential
$\mathbf{E}_{cathode}$	Positive electrode potential
$\mathbf{E}_{anode}$	Negative electrode potential
EC	Ethylene carbonate
$\mathbf{E}_{we}$	Voltage vs. working electrode
F	Faraday constant
GCPL	Galvanostatic Cycling with Potential Limitations

h	hours
I	Current
ICP-OES	Inductively coupled plasma - optical emission spectroscopy
LiPF$_6$	Lithium hexafluorophosphate
M	Molecular mass of active material
m	Amount of active mass involved in the reaction
n	Number of electrons
N$_A$	Avogadro number
NMP	N-Methylpyrrolidone
OCV	Open circuit voltage
P	Power
ppm	Parts per million- milligrams per liter (mg/L)
PVdF	Polyvinylidenfluoride
q	Charge
R	Universal gas constant
RT	Room Temperature
SEI	Solid Electrolyte Interface
SEM	Scanning electron microscopy
T	Temperature
t	Time
TG	Thermogravimetry
XRD	X-ray diffraction

$\Delta \mathbf{G}^{\circ}$ Standard Gibbs free energy

Additional Abbreviations used for the materials

LNMO-800 $^{\circ}$C $LiNi_{0.5}Mn_{1.5}O_4$ material synthesized at 800 $^{\circ}$C

LNMO-1000 $^{\circ}$C $LiNi_{0.5}Mn_{1.5}O_4$ material synthesized at 1000 $^{\circ}$C

LNRMO-800 $^{\circ}$C $LiNi_{0.4}Ru_{0.05}Mn_{1.5}O_4$ material synthesized at 800 $^{\circ}$C

LNRMO-1000 $^{\circ}$C $LiNi_{0.4}Ru_{0.05}Mn_{1.5}O_4$ material synthesized at 1000 $^{\circ}$C

LNF$_{0.2}$MO $LiNi_{0.4}Fe_{0.2}Mn_{1.4}O_4$ material synthesized at 1000 $^{\circ}$C

LNF$_{0.3}$MO $LiNi_{0.35}Fe_{0.3}Mn_{1.35}O_4$ material synthesized at 1000 $^{\circ}$C

LNF$_{0.4}$MO $LiNi_{0.3}Fe_{0.4}Mn_{1.3}O_4$ material synthesized at 1000 $^{\circ}$C

LNLa$_{0.01}$MO $LiNi_{0.495}La_{0.01}Mn_{1.495}O_4$ material synthesized at 1000 $^{\circ}$C

LNLa$_{0.05}$MO $LiNi_{0.425}La_{0.05}Mn_{1.5}O_4$ material synthesized at 1000 $^{\circ}$C

LNNd$_{0.01}$MO $LiNi_{0.495}Nd_{0.01}Mn_{1.495}O_4$ material synthesized at 1000 $^{\circ}$C

LNNd$_{0.05}$MO $LiNi_{0.425}Nd_{0.05}Mn_{1.5}O_4$ material synthesized at 1000 $^{\circ}$C

LNSm$_{0.01}$MO $LiNi_{0.495}Sm_{0.01}Mn_{1.495}O_4$ material synthesized at 1000 $^{\circ}$C

LNSm$_{0.05}$MO $LiNi_{0.425}Sm_{0.05}Mn_{1.5}O_4$ material synthesized at 1000 $^{\circ}$C

List of Figures

List of Tables

xxvi

Zusammenfassung

Lithium-Ionen-Batterien sind heutzutage aufgrund ihrer gleichzeitig hohen Energie- und Leistungsdichte für viele Anwendungen besonders gut geeignete Energiespeicher. Die Entwicklung und Verbesserung der eingesetzten Kathodenmaterialien sind Gegenstand intensiver Forschung, um Lithium-Ionen-Batterien an spezielle Anwendungen anzupassen. In dieser Arbeit wird das Hochvolt-Kathoden Material $LiNi_{0.5}Mn_{1.5}O_4$ und seine Metall- (Ru, Fe, La, Nd und Sm) dotierten Derivate untersucht. In den mittels eines Zitronensäure unterstützten Sol-Gel Verfahrens synthetisierten Materialien wird der Einfluss der Dotiermetallionen auf die Struktur, das elektrochemische Verhalten und den wirksamen elektrochemischen Mechanismus untersucht. Es werden zwei verschiedene Kalzinierungsendtemperaturen (800 °C und 1000 °C) zur Synthese der $LiNi_{0.5}Mn_{1.5}O_4$ und $LiNi_{0.4}Ru_{0.05}Mn_{1.5}O_4$ Materialien verwendet. Die Kalzinierungstemperatur von 800 °C wurde für die anderen metalldotierten $LiNi_{0.5}Mn_{1.5}O_4$-Proben ausgelassen, da diese im Vergleich zu den Hochtemperatur-Derivaten eine schlechtere elektrochemische Leistung aufweisen. Die Struktur und Morphologie der Materialien wurden mittels Röntgenpulverbeugung, Neutronenbeugung, Röntgenabsorptionsspektroskopie (XAS) und Rasterelektronenmikroskopie untersucht.

$LiNi_{0.5}Mn_{1.5}O_4$ Materialien bilden eine kubische Spinellstruktur mit Raumgruppe $Fd\bar{3}m$ und liegen nach der Synthese mit einer Nebenphase mit Kochsalzstruktur vor (Ni_6MnO_8). Die Ru-Dotierung unterdrückt die Bildung dieser zusätzlichen Neben-

phase. $LiNi_{0.4}Ru_{0.05}Mn_{1.5}O_4$ Materialien sind phasenrein und haben ebenso eine kubische Spinellstruktur mit der Raumgruppe $Fd\bar{3}m$. Durch Neutronenbeugung sowie Ru K-Kanten Röntgenabsorptionsspektroskopie konnte bestätigt werden, dass Ru im Spinell eingebaut wird. Die Materialien, die bei 1000 °C synthetisiert werden, haben eine höhere Leistungsdichte als die bei 800 °C synthetisierten. $LiNi_{0.4}Ru_{0.05}Mn_{1.5}O_4$-1000 °C zeigt bei Raumtemperatur eine bessere Zyklenstabilität und Strombelastbarkeit als $LiNi_{0.5}Mn_{1.5}O_4$-1000 °C. Nach 300 Zyklen bei einer C/2 Zyklierung verbleiben noch 84 % der anfänglichen Speicherkapazität. Dieser Wert is höher als für das undotierte $LiNi_{0.5}Mn_{1.5}O_4$-1000 °C von 79.5 %. Des Weiteren liefert die Ru-dotierte Probe eine höhere Entladungkapazität bei hohen C-Raten (136 mAh g^{-1} bei 20 C) als das Ausgangsstoff Material (122 mAh g^{-1} bei 20 C). Die Strukturuntersuchungen während der elektrochemischen Zyklierung zeigten, dass beide Materialien bei Li-Ein und Auslagerung einen Phasenübergang zwischen zwei Spinellphasen durchlaufen.

Ähnlich dem $LiNi_{0.4}Ru_{0.05}Mn_{1.5}O_4$, enthalten Fe-dotierte $LiNi_{0.5}Mn_{1.5}O_4$-Proben die Nebenphase mit Kochsalzstruktur nicht. Jedoch enthalten sie zusätzlich geringe Mengen von Li_2MnO_3 ($C2/m$) mit Schichtstruktur und von Spinell-Fe_3O_4 ($Fd\bar{3}m$). Die Fe-Dotierung im Spinell der Hauptphase wurde durch Neutronenbeugung sowie durch NMR- und Mössbauerspektroskopie bestätigt. Unter allen Fe-dotierten Kathoden und dem Ausgangsstoff $LiNi_{0.5}Mn_{1.5}O_4$, hat das $LiNi_{0.4}Fe_{0.2}Mn_{1.4}O_4$ die beste Speicherkapazität (92 %) nach 300 Zyklen sowie die höchste Anfangskapazität (134 mAh g^{-1}) bei Raumtemperatur. Das $LiNi_{0.4}Fe_{0.2}Mn_{1.4}O_4$ besitzt ebenfalls bei 55 °C eine höhere Speicherkapazität. Die gelieferten Kapazitäten bei hohen C-Raten (insbesondere bei 10 C und 20 C) sind in Bezug auf die erreichte Kapazität bei C/2 für alle Fe-dotierten Proben höher als für das etablierte Vergleichsmaterial $LiNi_{0.5}Mn_{1.5}O_4$. Fe-dotierte Proben zeigen außerdem ein anderes strukturelles Verhalten während der Zyklierung. Statt einer Koexistenz zweier Spinellphasen ändert sich die Zusasmmensetzung entsprechend einer festen Lösung kontinuierlich. Zudem liefert die *in situ* Synchrotonbeugung keinen Hinweis auf eine elektrochemische Aktivität der Neben-

phasen.

Die Analyse der Neutronenbeugung an La, Nd und Sm-dotiertem $LiNi_{0.5}Mn_{1.5}O_4$ zeigt, dass diese Elemente nicht in die Spinellstruktur eingebaut werden. Darüber hinaus enthalten sie neben der Nebenphase mit Kochsalzstruktur zusätzliche oxidische Phasen, die La, Nd oder Sm beinhalten. Die strukturellen Änderungen während der Zyklierung zeigen, dass nur die Hauptphase mit Spinellstruktur elektrochemisch aktiv ist.

Die Auswirkung der Massenbeladung auf Elektroden und Morphologie der Proben wird ebenfalls ausführlich erörtert.

Abstract

The Li-ion batteries are particularly suitable energy storage systems in several applications because of their simultaneous high energy and high power densities. Developing and improving appropriate cathode materials are in the focus of research in order to adapt lithium-ion batteries for specific applications. In this work the high-volt cathode material $LiNi_{0.5}Mn_{1.5}O_4$ and its metal (Ru, Fe, La, Nd and Sm) doped derivatives are synthesized using a citric acid assisted sol-gel method and the influence of the dopant metal ion on the structure, electrochemical performance as well as the underlying electrochemical mechanism are investigated. Two different final calcination temperatures (at 800 °C and 1000 °C) are used to synthesize $LiNi_{0.5}Mn_{1.5}O_4$ and $LiNi_{0.4}Ru_{0.05}Mn_{1.5}O_4$ materials. The 800 °C calcination temperature was then omitted for other metal doped $LiNi_{0.5}Mn_{1.5}O_4$ samples as they exhibit inferior electrochemical performance compared to their high-temperature derivative. The structure and morphology of the materials are investigated using X-ray, synchrotron and neutron powder diffraction techniques, X-ray Absorption Spectroscopy (XAS) as well as scanning electron microscopy.

$LiNi_{0.5}Mn_{1.5}O_4$ materials have cubic spinel structure with the space group $Fd\bar{3}m$ and they contain a rock-salt (Ni_6MnO_8) impurity phase. The Ru-doping suppresses the formation of this additional rock-salt phase. Ru-doped samples are phase pure and have also cubic spinel structure with the space group $Fd\bar{3}m$. It was confirmed by neutron diffraction as well as Ru K-edge XAS studies that Ru is present inside the

spinel material. The material synthesized at 1000 °C has better performance than the one at 800 °C. LiNi$_{0.4}$Ru$_{0.05}$Mn$_{1.5}$O$_4$-1000 °C has superior cycling stability as well as rate capability at room temperature compared to the parent LiNi$_{0.5}$Mn$_{1.5}$O$_4$-1000 °C. It has 84 % capacity retention after 300 cycles when cycled at C/2, which is higher than that of the parent LiNi$_{0.5}$Mn$_{1.5}$O$_4$-1000 °C (79.5 %). Moreover, Ru-doped sample delivers a higher discharge capacity at high C-rate (136 mAh g^{-1} at 20 C) than the parent material (122 mAh g^{-1} at 20 C). The structural investigations during electrochemical cycling show that both materials possess a phase-transition mechanism of Li intercalation/deintercalation through two spinel phases ($Fd\bar{3}m$).

As similar to the LiNi$_{0.4}$Ru$_{0.05}$Mn$_{1.5}$O$_4$, Fe-doped LiNi$_{0.5}$Mn$_{1.5}$O$_4$ samples do not contain the rock-salt impurity phase. However, they contain additional Li$_2$MnO$_3$ with a layered structure ($C2/m$) and spinel Fe$_3$O$_4$ ($Fd\bar{3}m$) phases. Fe-doping in the spinel material was confirmed by neutron diffraction, NMR and Mössbauer spectroscopy. Among all Fe doped cathodes and the parent LiNi$_{0.5}$Mn$_{1.5}$O$_4$, the LiNi$_{0.4}$Fe$_{0.2}$Mn$_{1.4}$O$_4$ has the best capacity retention (92 %) after 300 cycles as well as the highest initial capacity (134 mAh g^{-1}) at room temperature. The LiNi$_{0.4}$Fe$_{0.2}$Mn$_{1.4}$O$_4$ exhibits a higher capacity retention at 55 °C as well. The delivered capacities at high C-rates (especially at 10 C and 20 C) with respect to the capacity delivered at C/2 are superior for all Fe-doped samples compared to the parent LiNi$_{0.5}$Mn$_{1.5}$O$_4$. Fe-doped samples show a different structural evolution during cycling, which is described as a solid-solution mechanism. Moreover, there is no evidence from *in situ* synchrotron diffraction for any electrochemical activity of the impurity phases.

The neutron diffraction analyses of La, Nd and Sm doped LiNi$_{0.5}$Mn$_{1.5}$O$_4$ show that these elements are not inserted inside the spinel structure. In addition, besides the rock-salt impurity phase, they contain additional La, Nd or Sm containing phases. Structural evolution during cycling confirmed that only the main spinel phase is electrochemically active.

The effects of mass loadings on the electrodes and the morphology of the samples will also be discussed in detail.

Chapter 1

Introduction

Due to the rapid increase in the use of portable computers, mobile phones, video cameras, electronic devices, electrical vehicles etc., the urge for developing batteries with the lightest combination of anode and cathode, which also deliver high cell voltage and capacity, increases day by day. The latest and highest performance secondary battery system which fulfills these requirements is the lithium-ion (Li-ion) system, which was developed in the late 1970's and is now the fastest growing battery system in the world.

Developing and improving the appropriate cathode materials are essential points to adopt the lithium-ion batteries for their commercial applications. Among all the cathode materials, the Mn-based spinel materials are potential candidates for high energy density battery applications due to their high operating voltage and relatively high capacity [1, 2]. Moreover, they exhibit high-rate performance as a result of the 3D lithium-ion diffusion through the path formed by 8a tetrahedral and 16c octahedral sites [3–5].

The Ni-doped Mn spinel with the composition $LiNi_{0.5}Mn_{1.5}O_4$ (LNMO) is a highly promising cathode material which shows an impressive electrochemical performance like large reversible capacity at a high operating voltage around 4.7 V where the re-

versible $Ni^{2+} \rightleftharpoons Ni^{4+} + 2e^-$ redox reactions take place. In the completely stoichiometric $LiNi_{0.5}Mn_{1.5}O_4$ spinel, the oxidation states of Ni and Mn are +2 and +4, respectively, and no Mn ions exist in their trivalent state. However, usually a small amount of Mn^{3+} remains as a result of oxygen deficiency in the crystal lattice after the high temperature synthesis process [2, 6–8]. Mn^{3+} is well-known as a Jahn-Teller ion causing structural instability [9–12] but the effect of the amount of Mn^{3+} in LNMO is argumentative. Additionally, the electrochemical performance especially at high rates still needs to be improved to meet the required power density [13–15].

It has already been reported that cation doping on LNMO spinel enhances the reachable practical capacity, cycling stability and the cycling performance at high C-rates [6, 13, 14, 16]. The aim of this work is to investigate the effect of different cation dopings in LNMO on structure, electrochemical performance and Li-intercalation/de-intercalation mechanism in detail. The structural and morphology investigations are carried out by *ex situ* and *in situ* high resolution powder diffraction using synchrotron radiation and scanning electron microscopy, respectively. Elemental and thermal analyses are performed with Inductively Coupled Plasma-Optical Emission Spectroscopy (ICP-OES) and thermogravimetry, respectively. The electrochemical investigations are performed at room temperature (RT) as well as at 55 °C. The electrochemical mechanisms with respect to the structural changes for selected cases will also be discussed.

Chapter 2

Basic Concepts and Principles of Batteries

2.1 Introduction to Batteries

A battery converts the chemical energy directly into electric energy using an electrochemical reduction-oxidation (redox) reaction and consists of one or more electrochemical units (galvanic cell). A galvanic cell has two electrodes (the anode which releases the electrons and the cathode which accepts the electrons) and they are dipped in an electrolyte (ionic conductor, which provides the medium for transferring charge (ions) inside the cell between the anode and cathode).

Depending on the principle of operation, there are two main categories of batteries. One of them are primary batteries, which are used only once and discarded (chemical reactions, which take place in primary cells, are not easily reversible and active materials may not return to their original forms) and the other one are secondary batteries, which can be recharged (by applying electrical current, which reverses the chemical reactions that occur during its use) and used many times. It should be noted that the terms "anode" and "cathode" cannot be properly defined as by convention in

the case of rechargable batteries. Therefore, they should always be defined with respect to the discharging process or else the electrodes might be mentioned as positive and negative electrodes for higher and lower potentials, respectively.

2.2 Overview of Rechargable Lithium ion Batteries

The anode and the cathode in rechargable batteries have to sustain many charging and discharging processes and the structural changes should be reversible during cycling. The electrodes are surrounded by the electrolyte but a separator material is used to separate them mechanically to prevent internal short-circuiting. The separator is permeable to the electrolyte in order to maintain the ionic conductivity but impermeable to electrons.

The electrical capacity stored in Li-ion battery systems is related to the amount of Li ions inserted/extracted from the electrodes. The reason of using lithium in batteries in the first place is that it is the lightest metal among all metals and it is good reducing agent with standard electrochemical potential (Li/Li^+= -3.05 V). However, using metallic lithium in lithium ion battery is difficult because metallic lithium is expensive, additionally, it will tend to dendrite growth during cycling which will cause poor electrochemical performances and safety issues. For that reason, instead of metallic lithium, the anode in the lithium ion batteries is a lithium insertion compound with low standard potential of lithium insertion.

Even if the lithium ion batteries have their drawbacks, as need for additional protection against over charging/discharging or thermal runaway can occur under abnormal situations (crushing, puncturing etc.), they have many advantages, as well. The advantages of lithium ion batteries are:

✓ They have no memory effect (low maintenance)

✓ They have high energy density and potential (results in high capacity)

✓ Low self-discharge

✓ Different types of lithium ion battery systems are available that can be adopted to specific applications.

For a Li-ion cell, charging and discharging processes are shown in Figure 2.1.
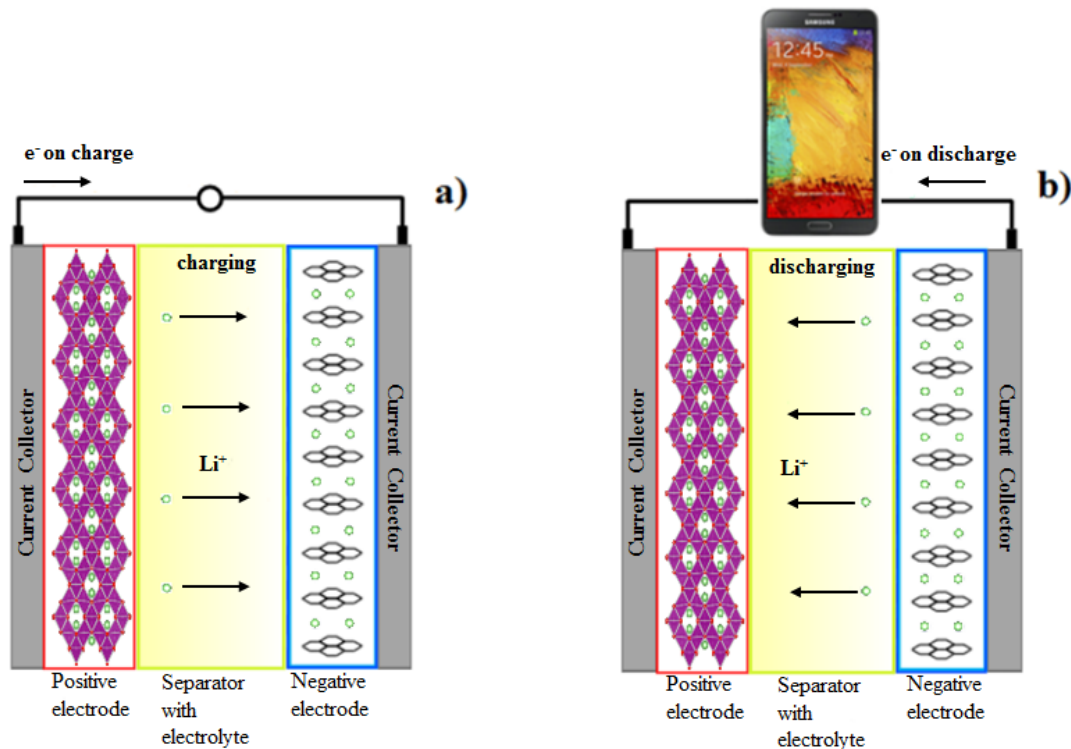
Figure 2.1: Electrons and ions-transport during a) charging and b) discharging in a Li-ion cell.

When the cell is connected to the external load, the discharging process takes place where electrons flow from the anode, which is oxidized, to the cathode, which accepts electrons and is reduced. At the same time the cations (+) flow to the cathode to complete the electric circuit. This process happens spontaneously. When the cell is recharged by connecting to a power supply, electrons flow the reverse way, and at the positive electrode oxidation occurs and at the negative electrode reduction occurs. As it was mentioned, this process occurs only if the cell is forced externally. According to

definition, the anode is the electrode where oxidation takes place and the cathode is the electrode where the reduction takes place during discharge.

The main components in Lithium ion batteries are;

✓ Cathode Materials; transition metal oxides i.e $LiCoO_2$ with layered structure, $LiMn_2O_4$ with spinel structure, $LiFePO_4$ with olivine structure and silicates etc.

Since this work focuses on $LiNi_{0.5}Mn_{1.5}O_4$ (and its derivatives by doping) positive electrode materials having the highest potential, they are named as "cathode materials". The equation 2.2.1 shows the charge/discharge reaction of $LiNi_{0.5}Mn_{1.5}O_4$, which occurs at a high potential of ~ 4.7 V (vs. Li/Li^+).

$$LiNi_{0.5}Mn_{1.5}O_4 \rightleftharpoons Li_{1-x}Ni_{0.5}Mn_{1.5}O_4 + xLi^+ + xe^- \quad (0 \leq x \leq 1) \qquad (2.2.1)$$
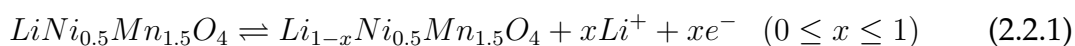
✓ Anode Materials; carbon based (i.e graphite, hard/soft carbon) and noncarbon alloys (i.e Li, Si, Sn, lithium alloys).

✓ Electrolytes must have good ionic conductivity but not be electronically conductive, because of internal short-circuiting. They must be non reactive with the electrode materials and should have only little change in properties with change in temperature. Additionally, they should be safe in handling and have low cost. $LiPF_6$ (lithium hexafluorophosphate) is the one with the lowest disadvantages from all known candidate salts considering all mentioned properties and good candidate for liquid organic electrolytes. The liquid organic electrolytes consist of such lithium salt and organic solvents such as, ethylene carbonate (EC), propylene carbonate (PC), dimethyl carbonate (DMC), diethyl carbonate (DEC), ethyl methyl carbobante (EMC) etc. The other classes of electrolytes are ionic electrolytes (also known as ionic liquids which are salts in liquid form at below 100 °C) and polymer electrolytes (which are formed by distributing the salt into a polymer and have less ionic conductivity compared to other electrolytes).

2.3 Important Definitions for Batteries

- **Cell Voltage (U):** The voltage is the driving force in an electrical circuit. This driving force causes the movement of free electrons through the circuit and is described as the potential differences (ΔE) of the cathode and the anode.

$$U = E_{cathode} - E_{anode} = \Delta E \text{ in V} \tag{2.3.1}$$

  ✓ Open circuit voltage: The voltage of a cell or a battery which is neither on charge nor on discharge (i.e., disconnected from a circuit).

  ✓ Closed circuit voltage: The voltage of a cell or a battery which is connected to a circuit and producing current into it.

- **Charge (q):** An ampere is a unit of electrical **current (I)**, which is defined as a rate of charge flow in an electric circuit, measured in Coulombs/second. The charge is the amount of current transferred in a unit of time (t).

$$Q = I \times t \text{ in Ampere-hour(Ah)} \tag{2.3.2}$$

- **Current Density:** The ratio of total current (A) and the surface area of the electrode where this current flows (A/cm^2).

- **Capacity (Q):** The capacity is the amount of charge, which is measured in Ampere-hours (Ah). The capacity per mass of reactants (Ah/kg) is called specific capacity.

- **Current Rate (C-Rate):** A common method for indicating the discharge and also the charge current of a battery is the *C rate*, which is numerically equal to the Ah (Ampere-hour) rating of the cell.

✓ 1 C means transfer of all of stored energy in one hour. In other words, 1C rate means that the entire battery will be discharged in 1 hour by the discharge current.

✓ 0.25 C (C/4) means full transfer of stored energy in 4 hours (25 % transfer in one hour) or 0.1 C (C/10) means full transfer of stored energy in 10 hours (10 % transfer in one hour) etc.

Discharge rates determine the battery capacity. The higher the discharge rate, the lower the cell capacity and vice versa.

- **Specific Power:** The amount of current that a battery can deliver per unit mass (m) or volume (V) of the cell.

$$P = \frac{U \cdot I}{m} \text{ in Watt/kg or} \tag{2.3.3}$$

$$P = \frac{U \cdot I}{V} \text{ in Watt/l} \tag{2.3.4}$$

- **Energy:** The output capability of a battery measured in Watt-hour (W=UxQ, Wh).

✓ Volumetric energy density (Energy density in Wh/L).

✓ Gravimetric energy density (Specific energy in Wh/kg).

- **Resistivity:** Electrochemical characteristics of the system which limits the amount of current that flows in it (in ohm, Ω).

- **Faraday Constant (F):** Quantity of charge per mole of electrons.

$$F = eN_A \text{ (96485.3 C/mol or 26.801 Ah/mol)} \tag{2.3.5}$$

$e \approx 1.602 \times 10^{-19}$ C and $N_A \approx 6.02 \times 10^{23}$ mol^{-1}

- **Cycle:** One sequence of a complete charging and discharging process.

2.4   Thermodynamic and Kinetic Aspects

The reactions that happen in the electrochemical system are based on thermodynamic and kinetic aspects. When the reactions occur, the system will start to release its free energy (Gibbs free energy, ΔG^o) which can be used to do work and is at standard conditions (at 25 ^{o}C temperature and 1 bar pressure) expressed as;

$$\Delta G = -nFE \ \ or \ \ \Delta G^o = -nFE^o \tag{2.4.1}$$

n: amount of electrons involved in the reaction

F: Faraday constant

E: cell potential under non-standard conditions in V

E^o: standard cell potential in V

The relationship between the Gibbs free energy under standard and non-standard conditions is given by van't Hoff isotherm as:

$$\Delta G = \Delta G^o + RTlna \tag{2.4.2}$$

$$-nFE = -nFE^o + RTlna \tag{2.4.3}$$

$$E = E^o - \frac{RT}{nF}lna \rightarrow \textbf{Nernst Equation} \tag{2.4.4}$$

R: gas constant (8.314 J mol^{-1}K^{-1})

T: temperature

a: ratio of the activities of products and reactants

The quantity of the electricity (nF) is directly proportional to the mass of active material involved in the reactions and the current (hence to the capacity) which is expressed by Faraday's law as;

$$Specific \ Capacity \ (\frac{Ah}{g}) = \frac{It}{m} = \frac{nF}{M} \tag{2.4.5}$$

$$m = \frac{ItM}{nF} \qquad (2.4.6)$$

I: current (ampere)

t: time (h)

m: amount of active mass involved in the reaction (gram)

M: molecular mass of active material (g/mol)

The electrochemical reactions inside the cell and hence capacity and performances are effected by the kinetic limitations depending on the redox reactions, resistance of the cell components and mass transportation during cycling. When the current flows inside a circuit, the voltage will differ from the open circuit voltage (E°) because of mentioned limitations. The situation is known as polarization or overvoltage given by the difference between the open circuit voltage and terminal cell voltage which exists when the current flows. Due to different kinetic effects, the polarization can be categorized into three groups;

- ✓ *Ohmic Polarization* occurs because of the resistance of all cell components like; electrolyte and electrodes and the contact between them, current collectors, terminals, the films formed on the electrode surfaces etc.

- ✓ *Activation Polarization* occurs because of the limitation of charge transfer (redox reactions) at the electrode/electrolyte interface.

- ✓ *Concentration Polarization* occurs due to the changes of the availability of the active species as a result of redox reactions. Limited diffusion of active species into/from electrodes give rise to concentration polarization.

The overvoltages cause differences of the cell voltage and therefore capacity compared to equilibrium state. The more the overvoltages in the batteries the more the reduced battery efficiency. Therefore keeping the overvoltages as low as possible is essential point.

Chapter 3

Aim of the Work

3.1 LiNi$_{0.5}$Mn$_{1.5}$O$_4$ Spinel Cathode

LiNi$_{0.5}$Mn$_{1.5}$O$_4$ (LNMO) is a highly promising cathode material due to the large reversible capacity at a high operating voltage around 4.7 V where the reversible $Ni^{2+} \rightleftharpoons Ni^{4+} + 2e^-$ redox reactions take place.

Two different crystallographic modifications exist for LNMO with respect to its synthesis temperatures: cation-ordered spinel (*P4$_3$32* space group) where the transition metal ions (Mn and Ni) occupy distinct Wyckoff sites (*12d* and *4b*, respectively) and cation-disordered spinel (*Fd$\bar{3}$m* space group) where the transition metal ions are randomly distributed and display shared occupancy at the same Wyckoff site (*16d*) [5, 17, 18]. The cation-disordered structure is also known as oxygen deficient structure, which is obtained at high annealing temperatures ($\geq$650 °C). On the other hand the cation-ordered structure can be obtained at low annealing temperatures ($<$650 °C) [19]. These two structures are shown in Figure 3.1. For LNMO (*P4$_3$32*) with a primitive cubic cell, the manganese ions are regularly distributed in *12d* sites, and nickel ions in *4b* sites. The oxygen ions occupy the *24e* and *8c* positions, while the lithium ions are located in the *8c* sites. For LNMO with a face-centered structure (*Fd$\bar{3}$m*), the lithium

ions are located in the *8a* sites of the structure, the manganese and nickel ions are randomly distributed in the *16d* sites. The oxygen ions which are cubic-close-packed (ccp) occupy the *32e* positions.
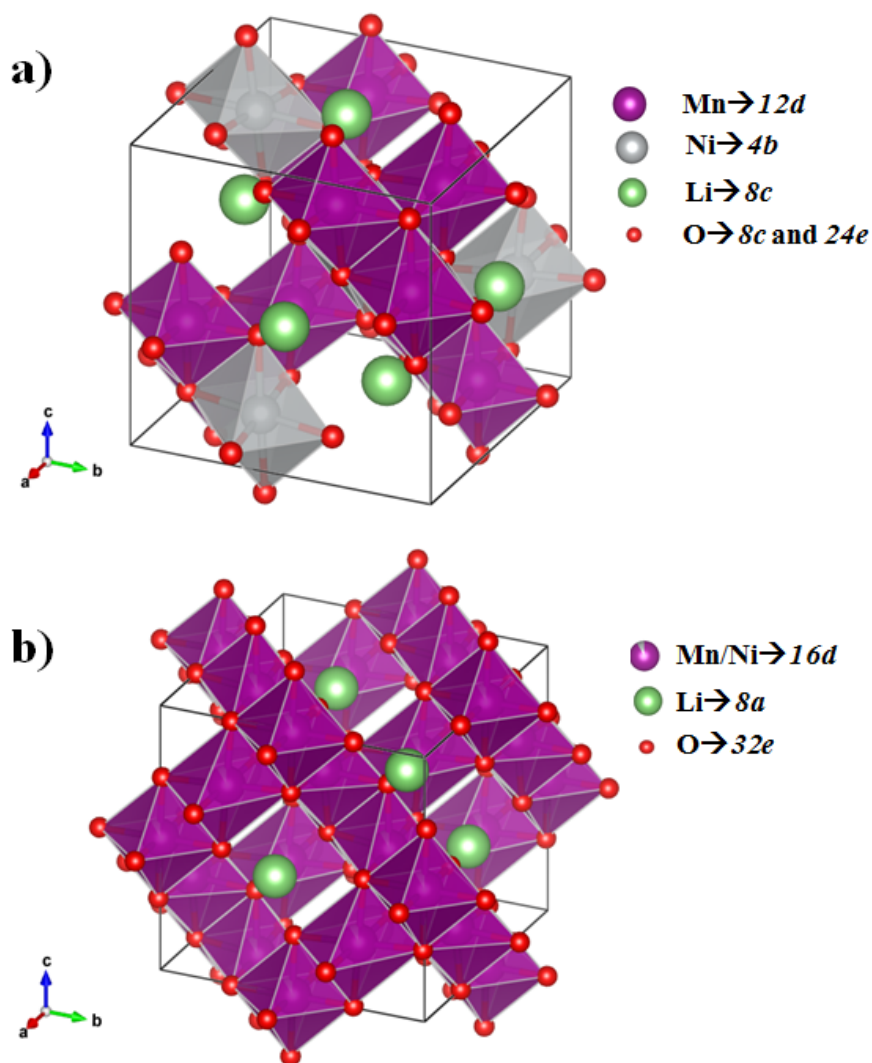
Figure 3.1: a) Cation-ordered structure ($P4_332$ space group) of $LiNi_{0.5}Mn_{1.5}O_4$ b) Cation-disordered structure ($Fd\bar{3}m$ space group) of $LiNi_{0.5}Mn_{1.5}O_4$.

From previous works on $LiNi_{0.5}Mn_{1.5}O_4$ and its derivatives it is known that the cation-disordered structure has better electrochemical performances than the cation-ordered one [20, 21].

3.2 The effects of transition metal ion doping on $LiNi_{0.5}Mn_{1.5}O_4$ spinel

In the ideal $LiNi_{0.5}Mn_{1.5}O_4$ spinel, the oxidation states of Ni and Mn are +2 and +4, respectively, and no Mn ion exists in the trivalent state, which is well-known as Jahn-Teller ion causing structural instability [9–12]. However, the high temperature synthesis of LNMO usually results in the formation of a rock-salt $Li_zNi_{1-z}O$ impurity phase due to oxygen loss [5]. This impurity reduces the amount of Ni in the cubic spinel phase and, thereby, together with some oxygen loss, increases the amount of Mn^{3+}, which strongly influences the electrochemical properties [5].

Different methods were adapted in the past to improve the electrochemical performances of LNMO such as coating and doping [5]. It should be noted that the term of "doping" is generally used in the literature which actually means cation and/or anion substitution on the structure. Among those a partial cation substitution of Ni, Mn or both in LNMO is found to be beneficial for the cycling stability. Fe [4, 22–25], Co [4, 16, 22], Cu [26, 27], Cr [4, 16, 22–24, 28–30], Ru [2, 15], Ga [4, 24], Mg [31, 32], Ti [23], Al [16, 26, 30], Zr [30], Rh [6, 33], Zn [23, 27] are the substituting elements that have been used and investigated so far.

It has already been reported that cation doping on LNMO spinel enhances the reachable capacity, cycling stability and cycling performance especially at high C-rates [6, 13, 14, 16, 34]. Furthermore, the doping of spinels by 3d or 4d cations can also improve the electrical conductivity and the structural stability [15, 35–37]. In 2010, Le *et al*. studied the influence of tetravalent cation substitution on LNMO [38]. They synthesized $LiNi_{0.5}Mn_{1.5-x}M_xO_4$, M = Ti (0<x<1.3) and Ru (0<x<1) samples with solid-state reactions. They have reported that Ti doping decreases the high-voltage electrochemical activity. In contrast, the capacity was maintained and the kinetics were improved by Ru doping. However, no high-rate investigations are reported in this work. Wang

et al. reported that the doping of Ru improves the rate capability and also the high-rate cycling stability of LNMO [14, 15]. They have synthesized the $LiNi_{0.5-2x}Ru_xMn_{1.5}O_4$ (x = 0, 0.01, 0.03, and 0.05) samples with solid-state and polymer-assisted methods. Among all the Ru-doped samples, $LiNi_{0.4}Ru_{0.05}Mn_{1.5}O_4$ showed superior cycling performance (at 10 C charge-discharge rate) and rate capability between 3.0-5.0 V. The substitution of a part of divalent Ni ions with tetravalent Ru ions induced some octahedral vacancies [15]. Since the lithium diffusion occurs between tetrahedral sites via vacant octahedral sites, the additional octahedral vacancies formed enhance the feasibility of this process. They reported that $LiNi_{0.4}Ru_{0.05}Mn_{1.5}O_4$ shows 100 % discharge capacity of its initial discharge capacity when charged with a rate of 0.2 C and discharged from 0.2 C to 2 C. For the high discharge rate of 10 C, it can still retain 89 % of its initial discharge capacity. At the highest rate of 10 C they reported discharge capacities of 117 mAh g^{-1} and 121 mAh g^{-1} for solid-state and polymer-assisted synthesized $LiNi_{0.4}Ru_{0.05}Mn_{1.5}O_4$, respectively. In the present study, $LiNi_{0.4}Ru_{0.05}Mn_{1.5}O_4$ is one of the transition metal doped LNMO which has been studied.

Partial substitution with Fe could also improve the thermal stability of the system as the spinel cathode materials containing Fe were found to have an increased onset temperature for thermal degradation [39]. In addition, Fe substitution could increase the structural stability of the system during cycling and thereby improve the long-term electrochemical performance. According to the work done by Liu & Manthiram, the partial substitution of Mn, Ni or both metals in $LiMn_{1.5}Ni_{0.5}O_4$ with Fe improves the cycling performance and rate capability [25]. They attributed these improvements to several factors like increased structural stabilization due to cation-disorder on the *16d* octahedral site of the spinel lattice, suppression of a thick surface film formation due to the Fe-enrichment and Ni-deficiency on the surface, formation of Mn^{3+} and the resultant increase in electronic conductivity and highly reduced polarization loss due to fast lithium ion diffusion and fast charge transfer kinetics in the bulk. Another work done by Zhong *et al.*, reported trivalent transition-metal substitution on LNMO, giv-

14

ing rise to a composition $LiNi_{0.45}M_{0.10}Mn_{1.45}O_4$ (M = Fe, Cr, Co) [22]. They observed an improvement in the rate capability which was attributed to the increased electronic conductivity resulting from the trivalent 3d cation substitution. In 2012, Shin $et\ al.$ reported cation ordering and surface segregation in $LiMn_{1.5}Ni_{0.5-x}M_xO_4$ (M = Cr, Fe, and Ga) cathodes [24]. According to their work, the right amount of cation substitution in LNMO improves the rate capability by suppressing cation ordering and thereby increasing the electronic and ionic conductivity in the material. Moreover, the dopant cations segregate to the electrode surface and suppress parasitic reactions with the electrolyte, which in turn improves the electrochemical performance at room temperature as well as at elevated temperatures. In 2013, Lee & Manthiram have studied the effect of different dopant ions on the degree of cation ordering in $LiMn_{1.5}Ni_{0.5-x}M_xO_4$ (M = Cr, Fe, Co, and Ga) spinels [4]. They observed that the differences in the degree of cation ordering on the $16d$ site of the spinel lattice originate from the size differences between the Mn^{4+} and M^{3+} (M = Cr, Fe, Co, and Ga) ions, which in turn induce a difference in the lattice strain during Li intercalation/de-intercalation. They also claimed that the dopant cation influences the electrochemical activity below 3 V. The other doping element which has been used in this study is Fe. The nominal composition of Fe-doped samples is $LiNi_{0.5-x}Fe_{2x}Mn_{1.5-x}O_4$ where x= 0.1, 0.15 and 0.2.

It has been reported that rare earth elements such as La, Nd, Er, Y, Ga, Sm, Ce etc. doped $LiMn_2O_4$ show improved electrochemical performances, as well. Recently Mo $et\ al.$ also reported the effect of Sm doping on $LiNi_{0.5}Sm_xMn_{1.5-x}O_4$ spinel [40]. They claimed that Sm replacement by Mn causes the decrease of lattice parameter and enhancement of cation disordering. Due to a more stable lattice structure, less amount of Mn^{3+} and enhanced ionic and electronic conductivity, the cycling performances and rate capabilities are greatly improved. The rare earth elements doped (La, Nd and Sm) LNMO samples have also been investigated in this study. Rare earth elements (La, Nd and Sm) have bigger ionic radii than Ni and Mn. Incorporated into the spinel structure bigger size compared to 3d metal dopants would widen the spinel lattice and thereby

improve the transport behavior. For the rare earth element doping on Ni or both Ni and Mn, two nominal compositions have been used; M is either La, Nd or Sm;

$LiNi_{0.5-x}^{2+}M_{2x}^{3+}Mn_{1.5-x}^{4+}O_4$ (x=0.005) and $LiNi_{0.5-3x}^{2+}M_{2x}^{3+}Mn_{1.5}^{4+}O_4$ (x= 0.025).

The doping effect on $LiNi_{0.5}Mn_{1.5}O_4$ investigated in the literature so far deals with only disordered $Fd\bar{3}m$ structure.

Chapter 4

Experimental

4.1 Synthesis of the Materials

The materials were synthesized by a citric acid-assisted sol-gel method in this work. The sol-gel process is a colloidal route to synthesize an oxide network through polycondensation reaction of molecular precursors in a liquid with an intermediate stage including a sol and/or a gel state [41]. The whole process is illustrated in Figure 4.1.

The metal acetates $LiCH_3COO \cdot 2H_2O$, $Mn(CH_3COO)_2 \cdot 4H_2O$, $Ni(CH_3COO)_2 \cdot 4H_2O$, $Ru(CH_3COO)_2$, $Fe(CH_3COO)_2$, $La(CH_3COO)_3 \cdot xH_2O$, $Nd(CH_3COO)_3 \cdot xH_2O$, $Sm(CH_3COO)_3 \cdot xH_2O$ were used as precursors depending on the stoichiometry of the materials to be synthesized. The corresponding metal acetates of target powder materials were dissolved in a mixture of citric acid and ethylene glycol (1:4 mol/mol) by heating at 90 °C in a glass beaker on the heating plate.

17
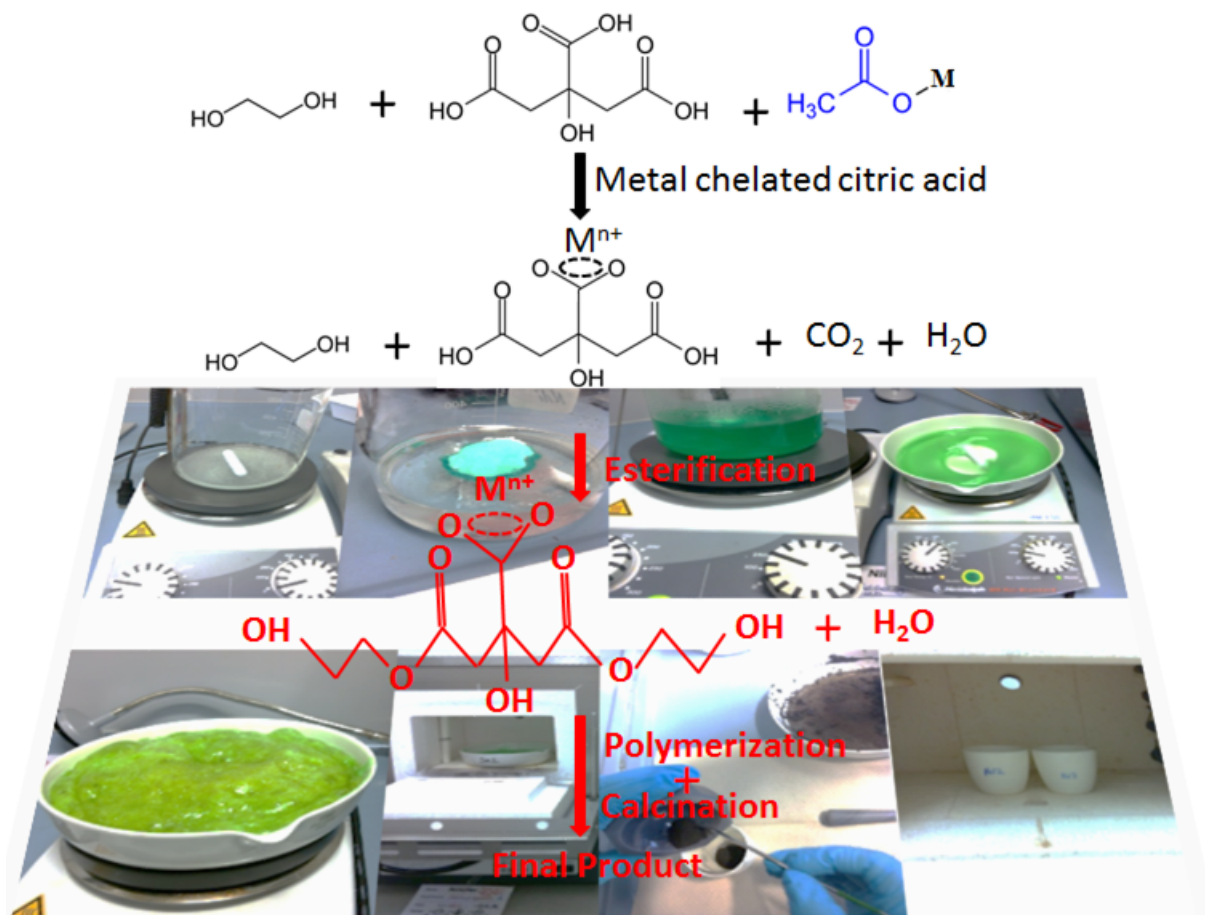
Figure 4.1: Citric acid-assisted sol-gel synthesis routes.

Later, the solution was heated at 180 °C to evaporate the excess ethylene glycol from the mixture and to get a transparent gel. When the mixture started to become gel form, it was transferred into a porcelain bowl. The obtained gel was pre-calcined at 400 °C for 5 h in the furnace to remove the carbon. When the furnace cooled down to room temperature, the mixture was ground in a mortar, transferred into alumina crucibles and then pre-annealed at 600 °C for 24 h in air with intermittent grinding. Until this step, the heating rate was 300 °C/h. After this step, the $LiNi_{0.5}Mn_{1.5}O_4$ and $LiNi_{0.4}Ru_{0.05}Mn_{1.5}O_4$ materials were separated into two parts for post annealing. One part of both material compositions was annealed at 800 °C and the other part at 1000 °C with a heating rate of 600 °C/h and holding time < 1 min and cooled down to RT in the furnace to obtain the final products. For all the other samples except these two materials, the post annealing was limited to one temperature (1000 °C).

4.2   Chemical Analysis

4.2.1   Inductively Coupled Plasma-Optical Emission Spectroscopy (ICP-OES)

The Inductively Coupled Plasma Optical Emission Spectroscopy (ICP-OES) technique is commonly used in laboratories for determination of elemental composition in a sample, which is introduced in liquid form. The principle of this method is that the analyte solution is nebulised and then vaporized within the argon plasma. At temperatures between 4725-6725 °C which are high enough to atomize and/or ionize the elements, the atoms and ions are electronically excited so that they emit light with characteristic wavelength which can be measured.

The determination of elemental concentration was done by ICP OES (iCAP 6500 Duo View (Thermo Fisher Scientific GmbH) in this study. Three parallel measurements were performed with similar weights per sample ($\sim$ 30 mg) to confirm the reproducibility. Therefore, the resulting values are the average of these three values for each sample. The samples were digested with 5 mL HCl (p.a., 37 %, Fa. Merck) at 180 °C. The digestion solution was then diluted with de-ionized water. The acid concentration in the sample solutions was 2 vol.% HCl (37 %). The calibration has been done with six standard solutions of different concentrations with an acid concentration of 2 vol.% HCl (37 %).

4.3 Structural Characterization Methods

4.3.1 X-Ray Diffraction

X-ray diffraction is a method used to determine the structure of a crystal, in which the crystalline material diffracts the X-ray beam in specific directions. The condition for diffraction is described by the Bragg Law (Equation 4.3.1).

$$2dsin(\theta) = n\lambda \qquad (4.3.1)$$

where d is the spacing between the scattering planes in the lattice, θ is the angle between incoming beam and scattering plane of the crystal and λ is the wavelength of the incoming beam.

By measuring intensities which are related to the structure factor, structural information can be extracted. Accordingly also structural changes as phase fraction, lattice expansion, change in atomic positions, occupation numbers, lattice strain and crystallite size can be determined. The structure analysis based on diffraction patterns was performed with the Rietveld method using the Fullprof software package [42]. The Rietveld method is based on minimizing the difference between experimental and calculated pattern. The model used for refinement is based on structural parameters as well as parameters determined by the experimental setup.

Crystallite size (D) and micro-strain (Δd/d) effects can be followed by investigating the angular dependence of the reflection broadening. Micro-strain broadening was investigated during Li insertion/deinsertion into/from the structure; conversely no size broadening was detected.

Additionally, to estimate site occupancies of the individual species the relevant occupation factors were constrained to be 100 % for each site.

Usually two different sources of X-rays are used; X-ray tubes and synchrotrons. X-ray tubes are laboratory or conventional X-ray sources where electrons are accelerated from a heated filament towards a metal anode target (cobalt, copper, molybdenum, silver etc.). After the electrons strike the target, they lose some of the energy eiher as Bremsstahlung or as characteristic radiaion. In synchrotron sources, relativistic electrons are stored in a storage ring which are accelerated towards the center of the ring by moving in a circular orbit and finally emit electromagnetic radiation [43] in a narrow cone in forward direction.

In this study, some of the *in situ* diffraction experiments during electrochemical cycling and *ex situ* experiments were performed at the high resolution powder diffraction beamline (P02.1) at PETRA-III, DESY, using synchrotron radiation with an energy of 60 keV (λ = 0.20726 Å) and exposure time between 5 seconds and 2 minutes per pattern. The initial powders were filled in glass capillaries with a diameter of 0.5 mm for *ex situ* investigations. The diffraction patterns were acquired using a 2D flat panel detector (Perkin Elmer Amorphous-Silicon detector). A photograph of the beamline is shown in Figure 4.2.
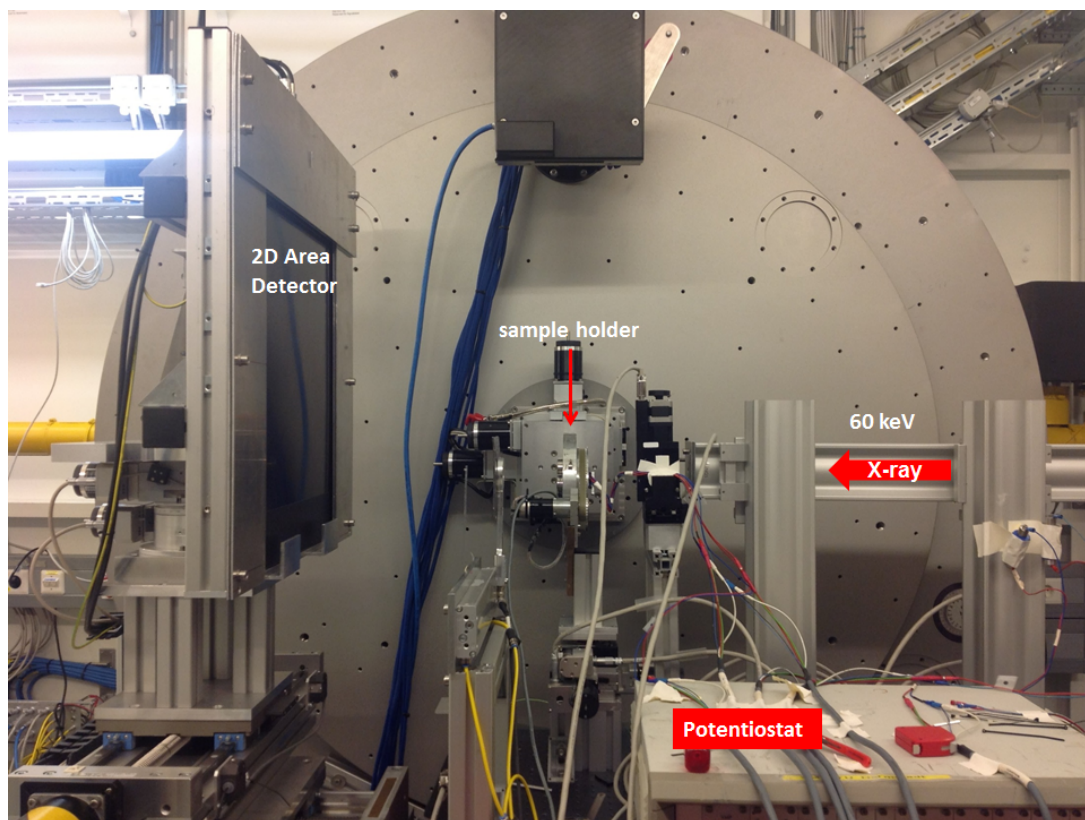
Figure 4.2: Overview of the beamline P02.1 at PETRA III, DESY, Hamburg.

The obtained 2D images were integrated to 1D diffraction patterns using the X-ray image processing program Fit2D [44].

The other *ex situ* and *in situ* experiments were performed at the Powder Diffraction beamline (MSPD) at ALBA (see Figure 4.3), using synchrotron radiation with an energy of 30 keV (λ=0.42477 Å) and exposure between 20 seconds and 2 minutes. The initial powders were again filled in glass capillaries with a diameter of 0.5 mm for *ex situ* investigations. The diffraction patterns at the MSPD beamline at ALBA are obtained using a MYTHEN 1D Position Sensitive Detector [45].
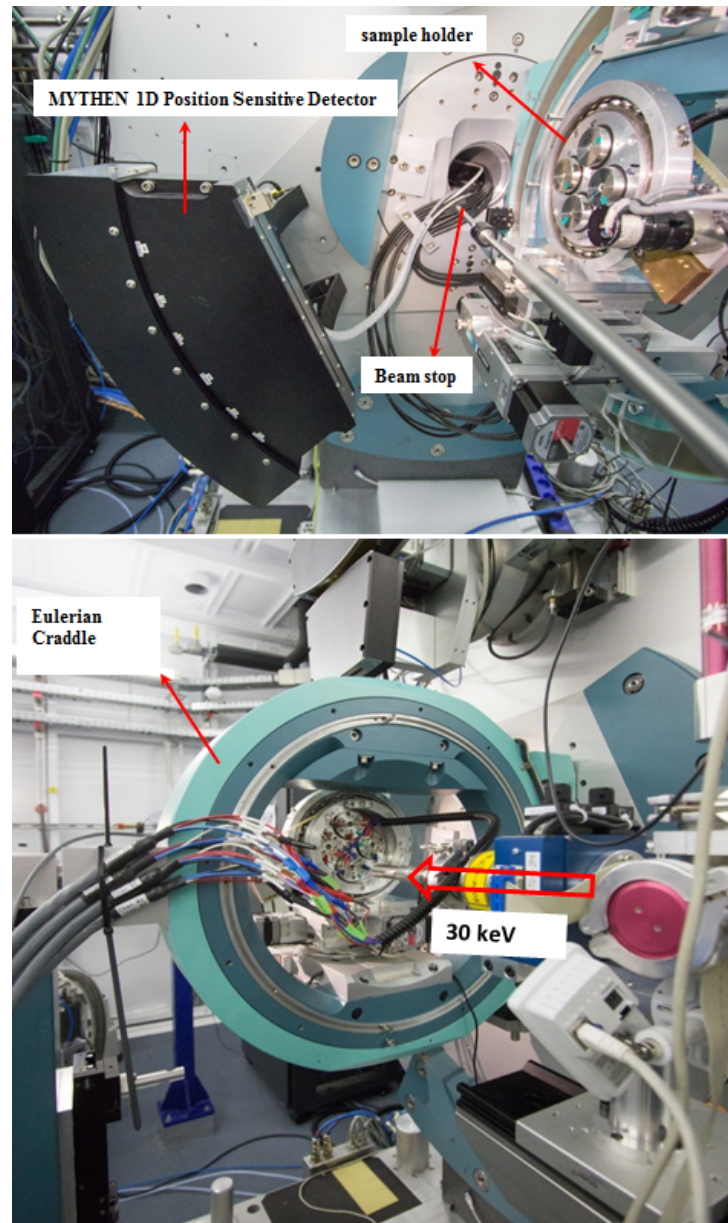
Figure 4.3: Overview of the beamline MSPD at ALBA, Barcelona.

4.3.2 Neutron Diffraction

Neutrons are particles without charge and interact only with the nucleus and not with the electron cloud around the atom as, for instance, X-rays. Since the neutron scattering length shows a very different behavior compared to the atomic form factor for X-ray scatterig, especially light atoms (eg. H, C, N, O, Li etc.) can be much better detected with neutron diffraction compared to X-ray diffraction [46]. Furthermore,

in some cases a much stronger contrast exists between scattering species in neutron diffraction than compared to XRD. Moreover, due to the spin interaction between neutrons and magnetic moments in the structure information about the magnetic ordering can be obtained which is not possible with X-rays.

The neutron datasets in this study were collected at the beamline Spodi, FRM II using a 2D multidetector and a Ge(551) monochromator [47]. The wavelength was estimated to 1.54831(2) Å (using Si NIST 640b standard) and zero-shift is 0.083(3)°2θ. The materials were filled in a vanadium container, the data were collected at room temperature and the time for one measurement was 8 hours per sample.

4.4 Morphology Studies

4.4.1 Scanning Electron Microscopy (SEM)

A tungsten filament or a field emission gun is used to generate an electron beam which is accelerated, then it scans the surface of the sample passing through some system apertures and electromagnetic lenses. The electrons of the electron beam, hitting the sample surface, penetrate into the sample and are scattered by the electrons and nuclei of the sample atoms. The scattering can be inelastic or elastic. As a result of the interaction of the sample with the incident beam, electrons and X-rays are ejected from the sample which are collected by a suitable detector and then monitored by the microscope operator.

The morphology of the particles was analyzed with a Zeiss Supra 55 SEM with primary energy of 15 keV and an in-lens detector. Before acquiring SEM images, a layer of 8 nm Au/Pd (Au = 80 % and Pd = 20 %) was sputtered on the surface of the samples using a DC sputtering device (SCD-050, Baltec) to reduce charging effects. Backscattered electron images were also collected for chosen samples. The backscattered elec-

trons are atomic mass of the nuclei sensitive which has an advantage to distinguish lighter elements from the heavier ones. Since the elements with higher atomic number backscatter electrons more efficiently than the one with lower atomic number, heavier elements will be brighter than the lighter one on the backscattered electron images.

4.5 Brunauer-Emmett-Teller (BET) Surface Analysis Technique

Brunauer-Emmett-Teller (BET) is the most common technique for determination of the surface area. In this technique, the analyte sample is exposed to a gas or vapour which is adsorped on the surface of the sample. The weak forces (van der Waals forces) occur between the adsorbate gas molecules and the adsorbent surface area of the sample due to physical adsorption. The amount of adsorbate gas on the surface is then calculated.

For BET surface area measurements of the samples, the nitrogen physisorption measurements were conducted using a Micromeritics ASAP 2020 system at 77 °K. These samples were degassed at 150 °C for 12 h prior to the measurements. The weights of these samples before and after degass were measured and the experimental densities were used to calculate the BET surface area. The specific surface areas of these samples were determined according to the BET theory.

4.6 X-Ray Absorbtion Spectroscopy (XAS)

XAS is an element specific spectroscopic characterization method. It is based on the absorbtion which can be used for studying oxidation states as well as local coordination of an absorbing atom. Depending on the absorption energy the technique can be classified either hard or soft XAS. The hard X-rays typically above 2500 eV, predom-

inantly give bulk information about the sample [48].

The XAS measurements were conducted to Ru-doped and undoped LNMO samples in this work. XAS measurements on Mn and Ni K-edges were carried out at the XAS beamline, ANKA, Karlsruhe and for the Ru K-edge at BM 23 beamline at the ESRF, Grenoble. XAS spectra on electrodes were recorded in transmission geometry for both Mn and Ni K-edges. However, due to the low amount of Ru in the sample, fluorescence geometry was preferred for the Ru K-edge measurements. The spectra were processed using the Demeter software package based on IFEFFIT and FEFF [49]. The X-ray absorption near edge (XANES) spectra of both Ru-doped and undoped samples at the Mn, Ni and Ru edges were compared with reference materials to obtain the oxidation states. Since XANES is a fingerprint technique, the position of the X-ray absorption edge can be correlated to the oxidation state of the absorbing atom. Extended X-ray absorption fine structure analysis (EXAFS) was done using a structural model for $LiNi_{0.5}Mn_{1.5}O_4$ with $Fd\overline{3}m$ space group.

4.7 Mössbauer Spectroscopy

Mössbauer spectroscopy is an element-specific spectroscopic technique that makes use of the recoil-less resonant emission and absorption of γ rays by specific nuclei (mostly Fe; sometimes Sn, Sb, Eu) in solids. A radioactive source is used to probe transitions between an excited state and the ground state of this nucleus. Different interactions of the nucleus with its electronic environment (Coulomb interaction with electron density, quadrupolar interaction with electric field gradients, Hyperfine interactions with local magnetic fields) give information about the charge state of the central ions, the coordination number, the type of ligands, bond properties, site symmetries, electronic spin states, and magnetic couplings [50].

Fe Mössbauer spectroscopic measurements were performed in transmission mode

at room temperature using a constant acceleration spectrometer with a ^{57}Co(Rh) source in this work. Isomer shifts are given relative to that of α-Fe at room temperature.

4.8 Nuclear Magnetic Resonance Spectroscopy (NMR)

Solid state MAS NMR spectroscopy is an element-specific spectroscopic method that can be used on a large number of elements in order to investigate local structures around these elements as well as dynamics of ions in condensed matter [51–53]. The sample is located in a magnetic field of typically several T and radiofrequency fields in the MHz regime are used to excite transitions between the Zeeman levels of the nuclear ground state. Different interactions of the nucleus with its electronic environment, including the shielding of the external field by binding electrons and quadrupolar interaction with electric field gradients, influence the spectra and thus give information about local environments around the nuclei. For powder materials, fast spinning of the sample (Magic Angle Spinning (MAS)) is necessary to obtain high resolution in the spectra.

NMR is both sensitive to the coordination environment of the nuclear probe, e.g. ^{7}Li, and to the electronic configuration in the proximity of the nucleus [54, 55]. Paramagnetic ions in the surrounding of the lithium ions have strong effects on the NMR spectra due to the Fermi-contact mechanism, *i.e.* the transfer of spin density from the unpaired electrons of the paramagnetic ions to the lithium nucleus.

In the present study, the ^{7}Li magic-angle spinning (MAS) nuclear magnetic resonance (NMR) spectroscopy was performed on a Bruker Avance 200 MHz spectrometer with a magnetic field of B_0 = 4.7 T, which is equivalent to a ^{7}Li Larmor frequency of 77.8 MHz. An aqueous 1M LiCl solution was used as the reference for the chemical shift of ^{7}Li (0 ppm). ^{7}Li MAS NMR experiments were performed using 1.3 mm zirconia rotors at a spinning speed of 60 kHz.

4.9 Thermogravimetry (TG) and Differential Scanning Calorimetry (DSC) Analyses

To understand the thermal behavior of the electrode material, simultaneous Thermogravimetry (TG) and Differential Scanning Calorimetry (DSC) Analyses were carried out using a Model STA 449 C (Netzsch, Germany) analyzer. TG is the technique that measures the difference of the mass obtained during heat treatment. The more the mass loss of samples indicates the more the degradation occurs. On the other hand, DSC is the technique to determine some thermal points like melting point, glass transition of materials, phase changes, crystallization, heat capacity etc.

The thermal responses were detected over the broad temperature range by scanning at a fixed heating rate. In this work, the temperature range was varied for the initial and the charged electrodes but heating rate was kept constant at 5 °C/min. The analyte powders were filled in an alumina crucible. The alumina crucible has been also used as reference for the calibration measurements. Additionally, thermal treatments have been applied under argon flow.

In order to perform thermal stability experiments of electrode samples, a powder mixture consisting of 80 % (w/w) active material, 10 % (w/w) super C 65 carbon (TIMCAL) and 10 % (w/w) polyvinylidenefluoride (Solef PVdF 6020 binder, Solvay) was grinded in a mortar. Later, the initial powder mixture of these three components were pressed with ∼ 3 tons to obtain a pellet with 8 mm diameter. The pellets were then charged up to 5 V with a charging rate of C/15. The charged samples were washed with DMC in argon atmosphere in order to remove the electrolyte residues. Finally, simultaneous TG-DSC was performed to obtain the thermal behavior for initial electrode

samples and fully charged samples under heat treatments.

4.10 Electrochemical Characterization

4.10.1 The Components in the Electrochemical Test Cells

4.10.1.1 Electrodes

- **The Working Electrode:** In this work, all of the working electrodes were pre-
  pared by mixing 80 % (w/w) of active material, 10 % (w/w) super C 65 carbon
  (TIMCAL) which is used as conductive agent and 10 % (w/w) polyvinylidene-
  fluoride (Solef PVdF 6020 binder, Solvay) binder which is used to keep the active
  material and the conductive agent together, in N-methyl-2-pyrrolidone (NMP,
  Sigma-Aldrich) to get a slurry. The obtained slurry was coated on a special alu-
  minium foil (which is almost pure and used in battery applications) with wet
  thicknesses of 120 μm and 300 μm. They were dried at 100 °C, punched out with
  a diameter of 1.2 cm and finally pressed with 7 tons/cm^2. Before assembling the
  test cells, the electrodes were re-dried in vacuum oven in the Ar filled glovebox.
  The mass loading and the final electrode thickness for 120 μm wet thickness coat-
  ings are ~2 mg and 12 μm and for 300 μm wet thickness coatings ~4.5 mg and 25
  μm.

- **The Counter Electrode:** A lithium metal foil (Alfa Aesar) which has high purity
  (99.9 %) with 0,75 mm thickness and 10 mm diameter was used as the counter
  electrode in the Swagelok®-type test cells and *in situ* cells. In the coin cells,
  lithium metal foil (Good Fellow) with high purity (99.9 %), 0.12 mm thickness
  and 12 mm diameter was used as the counter electrode.

4.10.1.2 Electrolyte

In this work, the LP30 Selectipur® electrolyte supplied from Merck which is 1M $LiPF_6$ in ethylene carbonate (EC): dimethyl carbonate (DMC) = 1:1 was used.

The common lithium ion battery electrolytes are solutions of $LiPF_6$ salt in a solvent blend of ethylene carbonate and various linear carbonates such as dimethyl carbonate, diethyl carbonate and ethylmethyl carbonate. Among these components , ethylene carbonate is essential for good solid-electrolyte interface (SEI) and $LiPF_6$ has low cost, high conductivity, good SEI formation properties, ability to effectively passivative an Al foil current collector and is the most appropriate salt for high voltage materials .

$LiPF_6$ salt has limited chemical stability but is thermally stable up to 107 °C in a dry inert atmosphere ($<$ 10 ppm H_2O)[56]. The other disadvantage is unavoidable detrimental HF contamination of its solutions. However, due to properties like good anodic stability, high solubility in polar aprotic solvents and thus yielding highly conductive solutions, the non-explosive and relatively non-poisonous behavior, it is the preferred electrolyte salt used in practical lithium ion batteries. Moreover, its decomposition path is a simple dissociation which is shown in Equation 4.10.1. $LiPF_6$ can be a source of powerful Lewis acid PF_5 under appropriate conditions [57].

$$LiPF_6 \rightarrow LiF + PF_5 \qquad (4.10.1)$$

Because P-F bonds are highly susceptible to hydrolysis, in the presence of even trace amounts of water ($\sim$300 ppm) in the electrochemical cell, POF_3 and HF will be formed (Equation 4.10.2) [56].

$$PF_5 + H_2O \rightarrow POF_3 + 2HF \qquad (4.10.2)$$

A rise in temperature will, of course, accelerate the formation of these species and their

further reaction with the solvents. Total reaction is then shown in equation 4.10.3:

$$LiPF_6 + H_2O \rightarrow LiF + POF_3 + 2HF \tag{4.10.3}$$
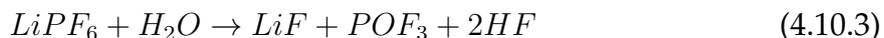
HF attack is especially dangerous for Mn-based spinel materials which causes Mn dissolution into electrolyte that results poor electrochemical performance. Therefore, it is important to keep the humidity low which is <15 ppm H_2O in standard battery electrolytes.

4.10.1.3 Separator

As a medium of ionic transportation in the test cell and also for the separation of the anode and the cathode material to prevent the short-circuit inside the cell, a glass microfiber filter supplied from Whatmann® (GF/D 70mm Ø) with 12 mm diameter was used. For the coin cells, the Celgard® trilayer PP/PE/PP battery separator with 16 mm diameter was used.

4.10.2 Layout of the Test Cells

4.10.2.1 *Ex situ* electrochemical experiments

Ex situ electrochemical experiments have been carried out by using two electrode Swagelok®-type test cells (see Figure 4.4) which were assembled in an argon-filled glove box with lithium foil (Alfa Aesar) as anode, LP30 (1 M $LiPF_6$ in ethylenecarbonate (EC):dimethylcarbonate (DMC) = 1:1) as electrolyte and glass microfiber filters (Whatmann®GF/D 70mm Ø) as separator. 200 μL electrolyte and two pieces of separators with 12 mm diameter have been used for each test cell.

1.   Steel Plunger
2.   Perforated Nut
3.   Aluminium Plunger
4.   Tube Fitting
5.   Spring
6.   Nickel Disk
7.   Lithium Foil
8.   Electrolyte
9.   Separator
10. Working Electrode
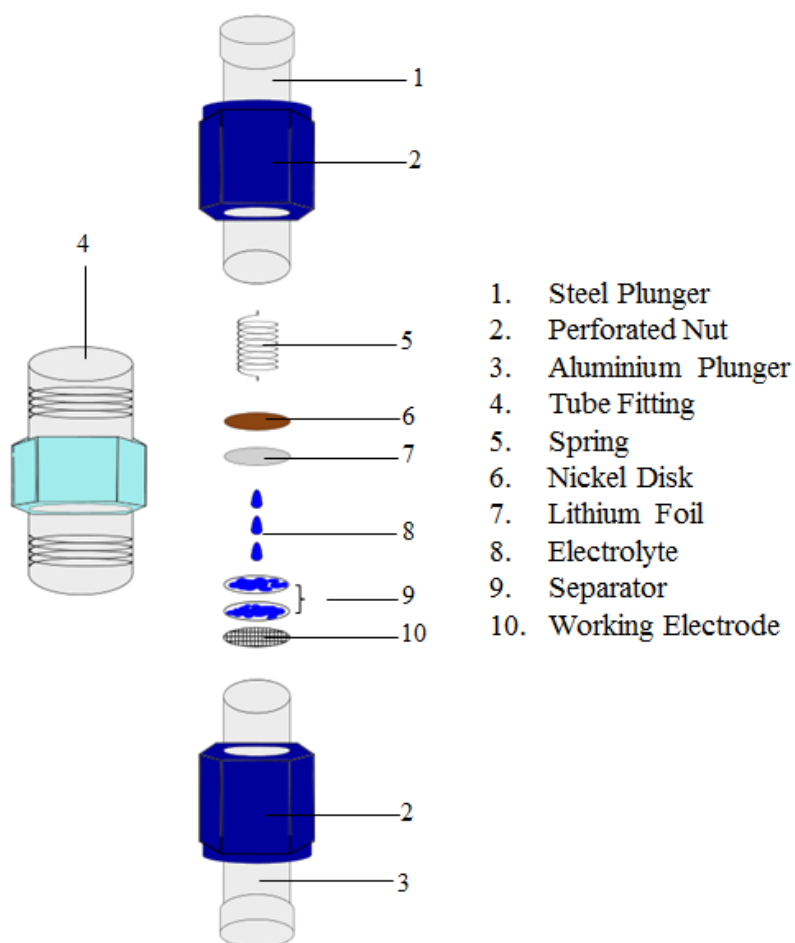
Figure 4.4: Shematic drawing of two electrode Swagelok®-type test cell.

4.10.2.2 *In situ* electrochemical experiments

For the *in situ* investigations of selected samples at the synchrotron facilities, an *in situ* cell design as shown in Figure 4.5 was used [58]. The cell housing is made of stainless steel. The windows of the cell for the beam are sealed with thin glass discs (∼100 μm), fixed with a high-density polyethylene foil by heating up to 180 °C. The procedure of assembling these *in situ* cells is the same as for Swagelok®-type cells.

1: 100 μm glass window
2: contact spring
3: sealing ring
4: insulating PTFE ring
5: current collector

6: 100 μm glass window
7: current collector foil
8: working electrode
9: separator
10: counter electrode
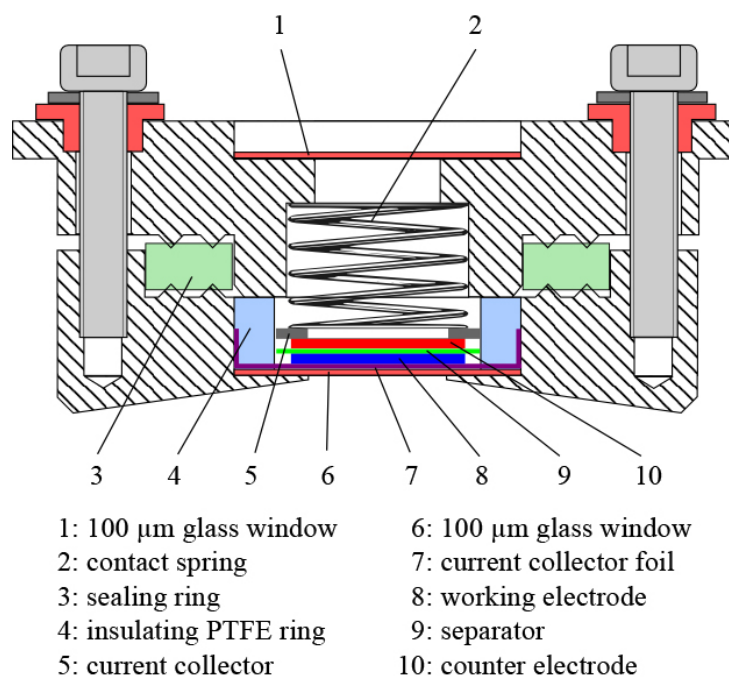
Figure 4.5: Shematic drawing of the test cell for *in situ* investigations (reproduced with permission from Herklotz *et.al*, 2013).

The sample holder can hold four *in situ* cells (See Figure 4.7, left) that can be automatically interchanged by a motor allowing *in situ* measurements of 4 cells cycling in parallel.

Another cell design for the *in situ* investigations is a coin cell design (CR2025, CR2032, CR2016 etc.). There are holes in the housing of the coin cells, which allow the beam passing through the sample. These holes were then sealed either with Kapton foil or aluminated Kapton foil, using the acid modified polyethylene (PE) foil as glue, by heating them up to 180 °C (see Figure 4.6). For the *in situ* coin cell setup, the same electrolyte was used. However, in this case, one piece of Celgard® trilayer PP/PE/PP separator (soaked in the electrolyte minimum 8 hours) and thin lithium foil (0.12 mm thickness) were utilised.

1.	Aluminated Kapton foil
2.	Kapton Foil
3.	Acid modified polyethylene(PE) foil
4.	Housing of coin cell with hole
5.	Housing (top) of coin cell sealed with Kapton foil
6.	Spring
7.	Spacer with hole
8.	Housing of coincell sealed with aluminated Kapton foil
9.	Sealing ring
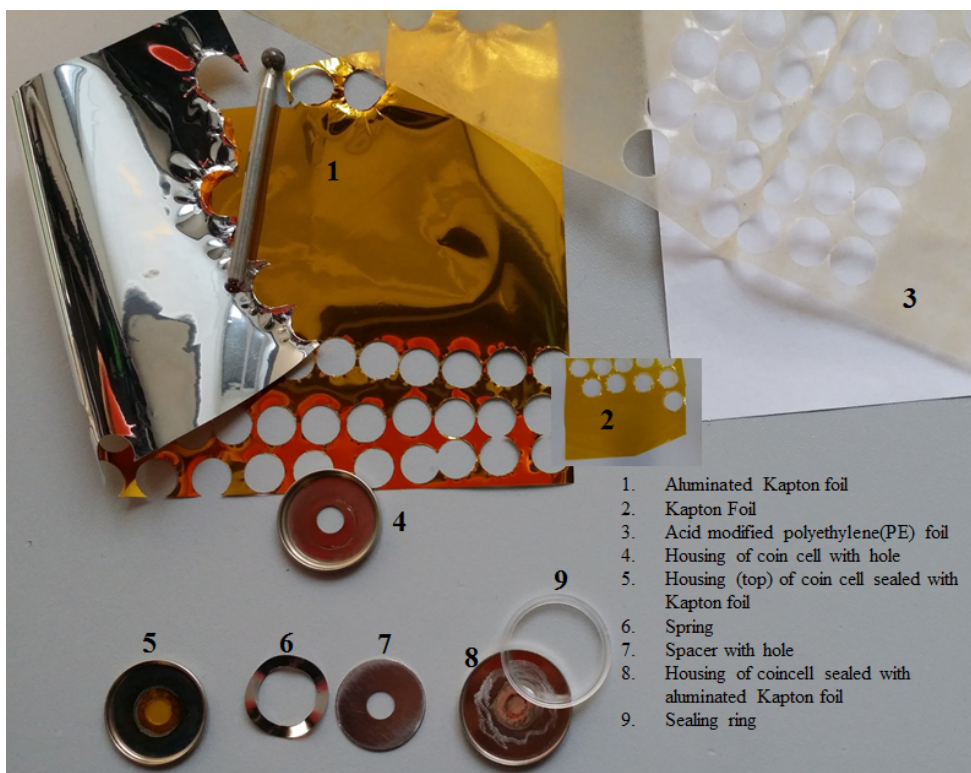
Figure 4.6: Sealing the *in situ* coin cells.

The sample holder can hold eight *in situ* coin cells (See Figure 4.7, right) that can be automatically interchanged allowing cycling of eight cells in parallel again controlled by rotation motor.
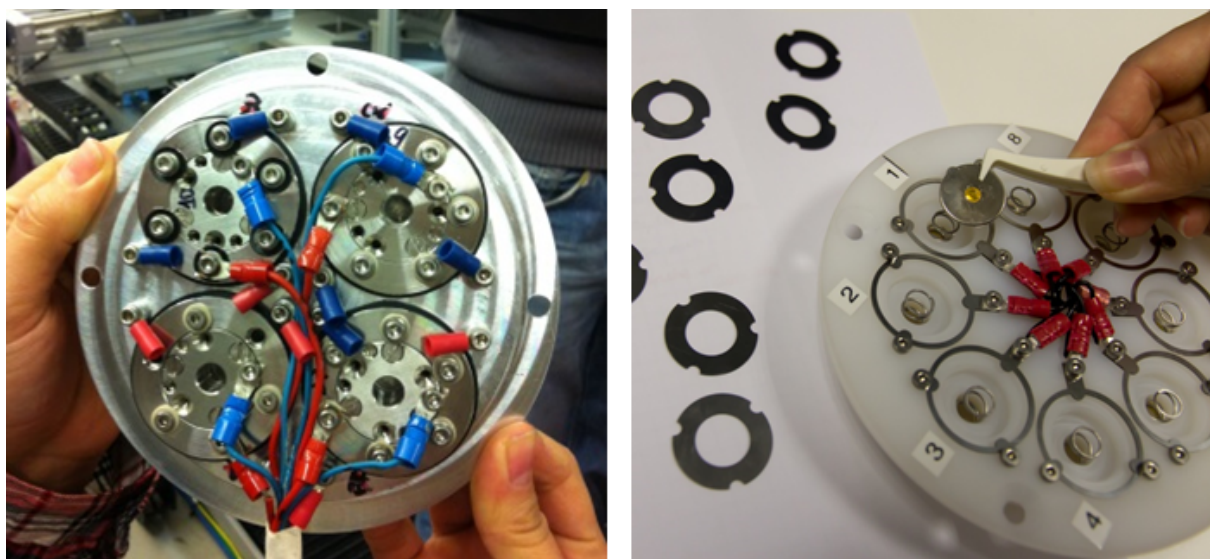
Figure 4.7: *In situ* cell (left) and *in situ* coin cell (right) holders.

4.10.3 Electrochemical Cycling Experiments

4.10.3.1 Instrument

A VMP (Perkin Elmer Instruments, USA) multichannel potentiostat controlled by computer with the program EC-Lab was used to perform electrochemical experiments. The channels were placed in a temperature controlled climate chamber which allows to perform electrochemical experiments at different temperatures.

4.10.3.2 Techniques

There are several techniques, which can be applied to test the electrochemical performance of the cells. In this research, two of these were mainly used such as;

✓ Cyclic Voltammetry (CV)

✓ Galvanostatic Cycling with Potential Limitation (GCPL)

Cyclic Voltammetry (CV):

The CV technique enables to measure the current resulting from oxidation/reduction reactions during scanning of the potential between two given values at a fixed rate. The CV technique is usually used for determining the electrochemical activity regions in the working electrodes. Additionally, it provides information on the properties of redox reactions. Figure 4.8 shows an example for cyclic voltammetry of a LiNi$_{0.5}$Mn$_{1.5}$O$_4$ spinel cathode. A reversible electrochemical activity can be observed at around 4 V which is attributed to the Mn^{3+}/Mn^{4+} redox couple [59, 60]. The two peaks in the region of 4.5-4.9 V during oxidation and reduction processes can be attributed to the $Ni^{2+} \rightleftharpoons Ni^{4+} + 2e^-$ reactions [1, 2, 5, 7, 59–61].

In this work, the scan rate used for the CV experiment was always 0.1 mV s^{-1}. However, the voltage range was varied depending on the active material investigated.
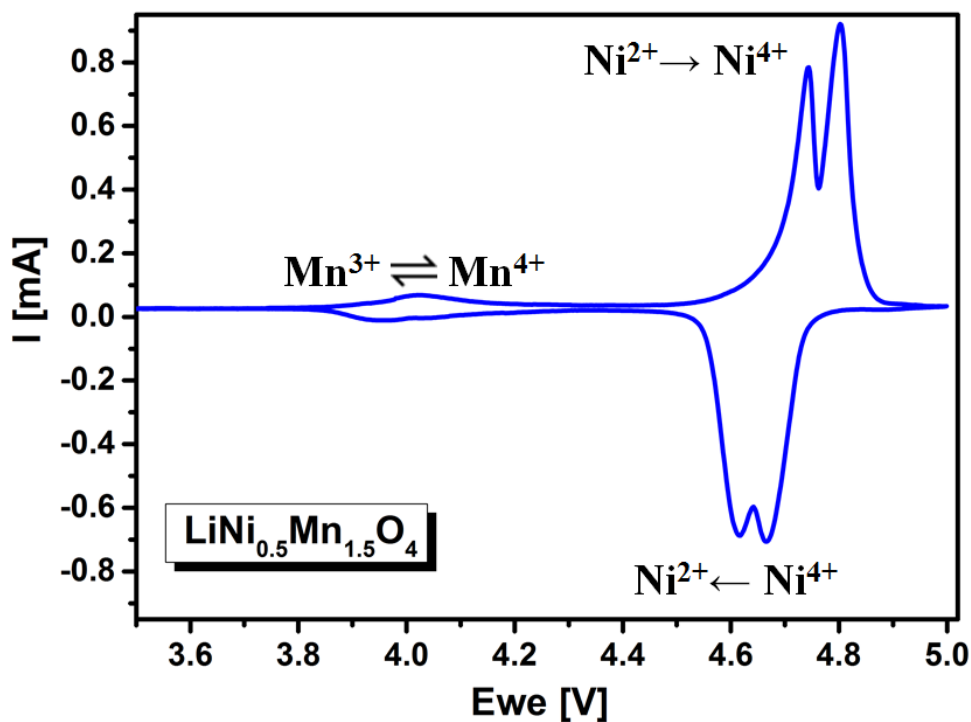
Figure 4.8: Cyclic Voltammogram of $LiNi_{0.5}Mn_{1.5}O_4$ spinel cathode material.

Galvanostatic Cycling (GCPL):

In this technique, a constant current (which is related to the C-rate) is set with potential limitations of working and counter electrodes. The changes of potential between the given range with time are recorded. The results of Galvanostatic cycling are usually presented as E (voltage) vs. t (time) or E vs. specific capacity (mAh g^{-1}). An example of galvanostatic cycling is shown in Figure 4.9.

36
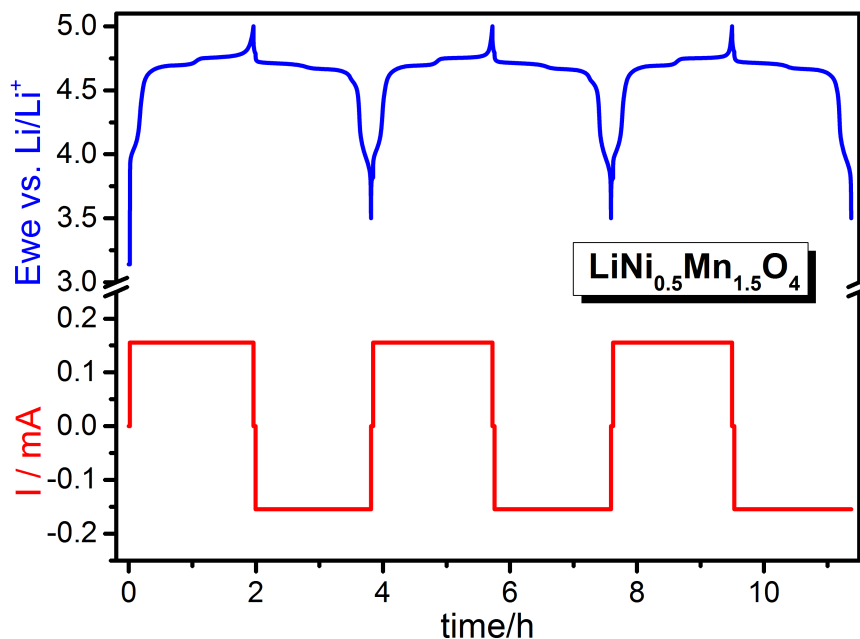
Figure 4.9: Galvanostatic cycling of LiNi$_{0.5}$Mn$_{1.5}$O$_4$ spinel cathode material.

In this work, GCPL technique is applied in order to perform cycling stability and rate capability performances. Cycling stability performance of a battery which is related to its cycle life as well as having a good performance at different current rate are very important for its applications. The current rate was kept constant (C/2) during charging and discharging processes for cycling stability performances. The rate capability experiments were carried out by keeping the charging current rate constant (C/2) and applying different discharging current rates such as 1 C, 5 C, 10 C and 20 C.

Chapter 5

Results and Discussions

5.1 LiNi$_{0.5}$Mn$_{1.5}$O$_4$ Spinel as High-Volt Cathode Material

5.1.1 Structural Analyses

LiNi$_{0.5}$Mn$_{1.5}$O$_4$(LNMO) powders synthesized at 800 °C and 1000 °C have cubic spinel structure and the patterns are indexed with the *Fd$\overline{3}$m* space group (see Figure 5.1). An impurity phase Li$_z$Ni$_{1-z}$O (*Fm$\overline{3}$m*) with rock-salt structure is obtained for LNMO-800 °C and LNMO-1000 °C powders with phase fractions of 1 % and 3 %, respectively. This Li$_z$Ni$_{1-z}$O phase is a quite well known impurity phase which occurs as a result of increased oxygen loss from the crystal lattice due to the high synthesis temperature [1] which in turn increases the amount of Mn^{3+} in the LNMO sample. The structural parameters obtained from Rietveld refinement based on the synchrotron data are listed in Table 5.1. In all the diffraction patterns presented in this study, the observed data are shown as points in red, the calculated profiles are shown as black line, the corresponding difference between observed and calculated are date shown as line in blue and the calculated Bragg positions of reflections are shown as the vertical lines in green colours.
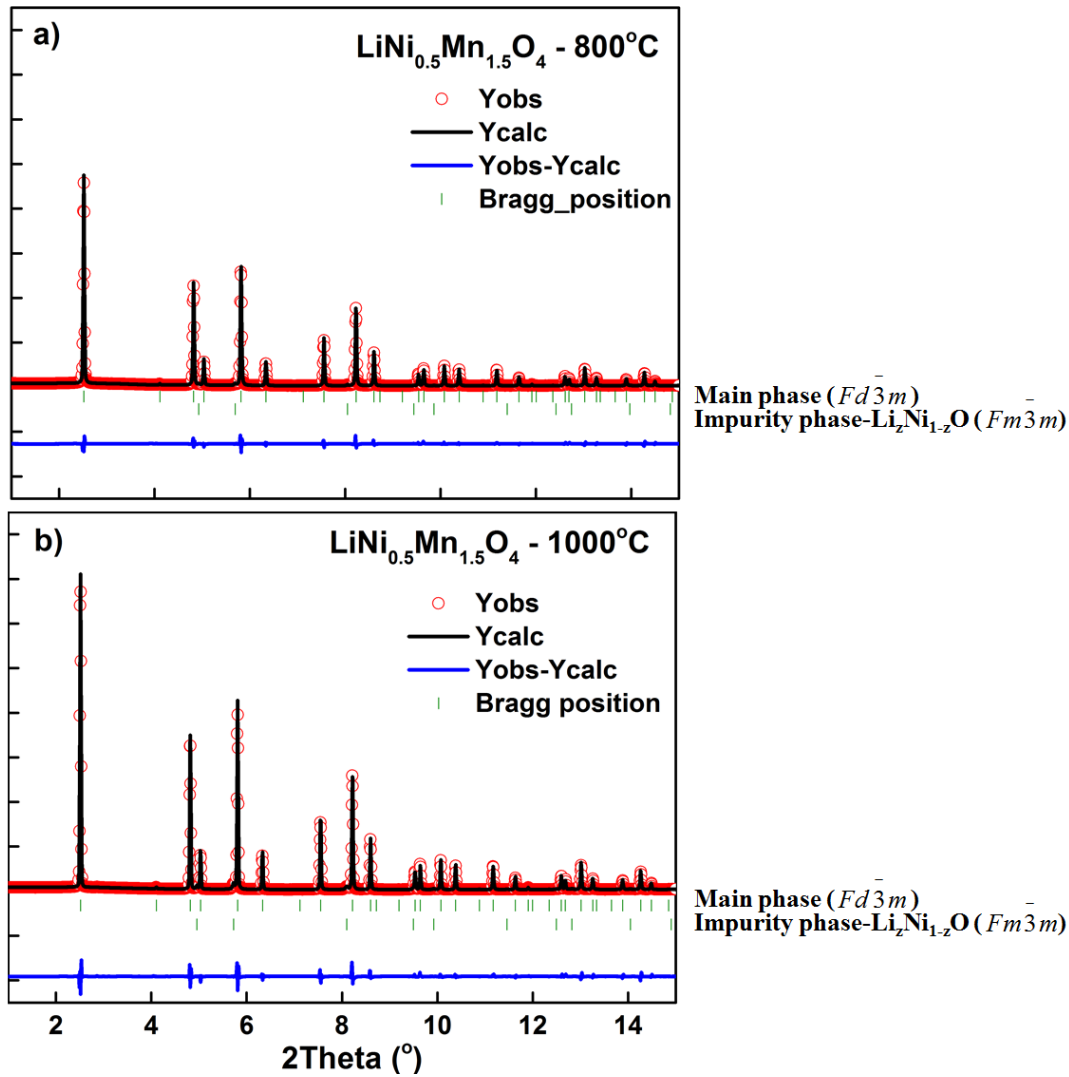
Figure 5.1: Rietveld refinement results based on synchrotron diffraction patterns of as prepared a) LNMO-800 °C b) LNMO-1000 °C materials measured in 0.5 mm capillaries.

The increase of lattice parameters with increasing synthesis temperature can be attributed to oxygen loss from the crystal lattice which in turn increases the Mn^{3+} content in the sample [1]. Since Mn^{3+} has higher ionic radius ($\sim$ 0.645 Å) than Mn^{4+} ($\sim$ 0.53 Å) [62], the unit cell would expand.

Samples	Atomic Site	x=y=z	a(Å)	Volume (Å^3)	Fraction of impurity phase %	Overall Temperature Factor (B$_{ov}$)	R$_{wp}$(%)
LNMO-800°C	Li$_{8a}$ Ni$_{16d}$ Mn$_{16d}$ O$_{32e}$	0.125 0.500 0.500 0.2630(3)	8.1722(1)	546(1)	1	0.38	6.25
LNMO-1000°C	Li$_{8a}$ Ni$_{16d}$ Mn$_{16d}$ O$_{32e}$	0.125 0.500 0.500 0.2630(4)	8.1779(1)	547(1)	3	0.39	8.68

Table 5.1: Rietveld refinement results of LNMO samples based on synchrotron diffraction data (space group $Fd\bar{3}m$).

As already mentioned the impurity phase in LNMO spinel sample is usually treated as Li$_z$Ni$_{1-z}$O. However, the careful analysis of recently obtained neutron diffraction data for the sample reveals that the impurity phase can be better fitted with the Ni$_6$MnO$_8$ ($Fm\bar{3}m$ space group) phase. The neutron diffraction pattern of LNMO-1000 °C is shown in Figure 5.2. The inset figure of Figure 5.2 indicates the zoomed area of whole pattern where additional two Bragg positions exist (shown with arrows) which belong to Ni$_6$MnO$_8$ rock-salt structure but not to Li$_z$Ni$_{1-z}$O. The phase fraction of Ni$_6$MnO$_8$ is ∼3 %. This information is not clearly observable in XRD patterns. The calculated stoichiometry from the refined site occupation factors based on the Rietveld refinements of neutron data is Li$_{1.02(5)}$Ni$_{0.45(1)}$Mn$_{1.55(1)}$O$_4$.
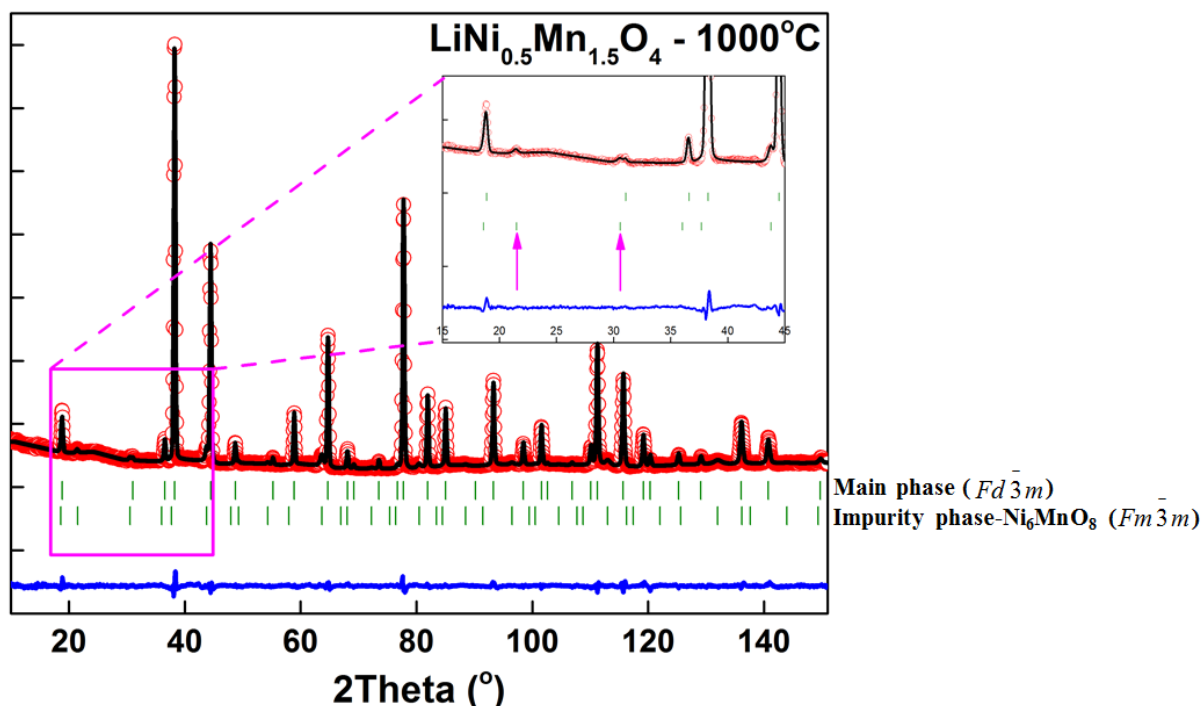
Figure 5.2: Rietveld refinement result based on the observed neutron diffraction pattern of as prepared $LiNi_{0.5}Mn_{1.5}O_4$-1000 °C powder.

5.1.2 Elemental Analysis (ICP-OES)

Table 5.2 displays the Li/transition metal ratios of the LNMO samples synthesized at 800 °C and 1000 °C as determined by ICP-OES. The observed values were calculated assuming that Li has complete stoichiometry and the results show that no significant difference is detectable between the samples synthesized at 800 °C and 1000 °C.

It should be noted that the Ni:Mn ratio obtained from ICP-OES (0.5004 : 1.5172) is different from that calculated from neuton diffraction results for the spinel phase (0.45 : 1.55). This can be explained on the fact that the ICP-OES provides only the total ratio of elements in the sample but the stoichiometry calculated from neutron diffraction corresponds to the specific phase (here the $Fd\bar{3}m$ phase). The impurity phase is a Ni-rich phase which is contributing also in ICP-OES.

Sample	Ratio of Li: Transition Metals (expected)	Ratio of Li: Transition Metals (observed)	Ratio of Transition Metals Ni:Mn (observed)
LNMO-800 °C	0.5	0.4951	0.5025 : 1.5172
LNMO-1000 °C	0.5	0.4956	0.5004 : 1.5172

Table 5.2: The results of ICP-OES analyses of LNMO-800 °C and LNMO-1000 °C.

5.1.3 Morphology Studies of initial $LiNi_{0.5}Mn_{1.5}O_4$ powder

SEM images of LNMO-800 °C and LNMO-1000 °C are presented in Figure 5.3a and b, respectively. The LNMO particles obtained after annealing at 800 °C lack well defined edges and the particle sizes are in the range of 50-200 nm. In contrast, the particles of the materials synthesized at 1000 °C exhibit pseudo-octahedral shape with smoother surfaces with the size range 1-2 μm for LNMO-1000 °C .
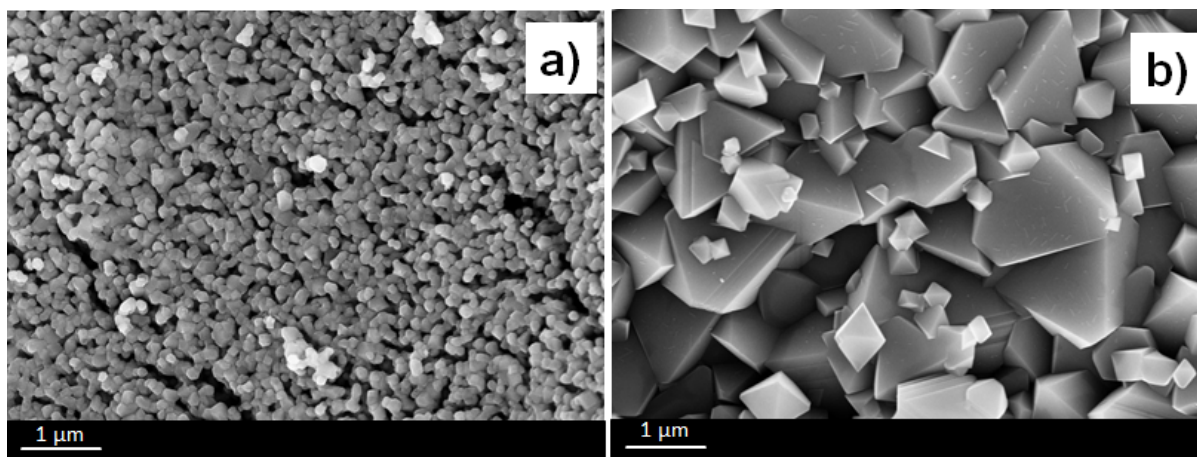
Figure 5.3: SEM images of as prepared a) LNMO-800 °C, b) LNMO-1000 °C powders.

5.1.4 Electrochemical Performances of LiNi$_{0.5}$Mn$_{1.5}$O$_4$ Cathode Materials at Room Temperature (RT)

5.1.4.1 Cyclic Voltammetry (CV)

In order to determine the electrochemical activity regions contributing to the electrochemical performance of the electrode materials, cyclic voltammetry has been conducted. The electrochemical test cell of LNMO-1000 °C cathode material was cycled between the voltage range of 3.5-5.0 V with the scan rate of 0.1 mV s^{-1}. According to the 1st and the 10th CV curves of LNMO-1000 °C spinel samples shown in Figure 5.4, there is a reversible electrochemical activity at around 4 V which is attributed to the Mn^{3+}/Mn^{4+} redox couple [59, 60] which is still present after 10 cycles.
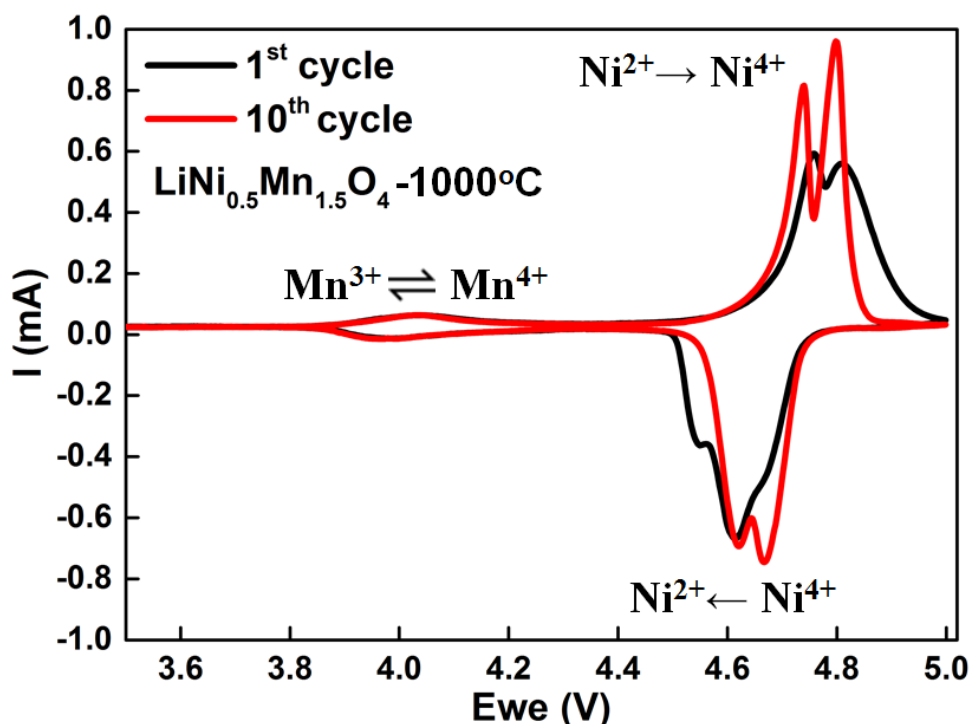
Figure 5.4: Cyclic voltammograms of 1st cycle and 10th cycle of LNMO-1000 °C cathode material with the scan rate of 0.1 mV s^{-1} in a voltage range 3.5-5.0 V.

The two peaks in the region of 4.5-4.9 V during oxidation and reduction processes

are related to the Ni^{2+}/Ni^{4+} redox couple [1, 2, 5, 7, 59–61].

5.1.4.2 Cycling Stability

Since a lithium ion battery provides energy storage and conversion repeatedly, the sustainability with good efficiency of these properties play an essential role for suitability of its applications in real life. Therefore, the better cycle life means the more demand.

To study cycling stability, all electrochemical experiments were repeated at least two times for each sample in order to check reproducibility. The cycling stability results of the first 300 cycles of LNMO synthesized at 800 °C and 1000 °C with a C/2 charge-discharge rate in the voltage window 3.5-5.0 V which have been repeated 4 times for each sample are shown in Figure 5.5. For the material synthesized at 800 °C, the capacity fading is much higher than the material synthesized at 1000 °C. In addition, LNMO-800 °C shows different character compared to LNMO-1000 °C until ∼100 cycles where the most ponounced degradation can be seen. In contrast, LNMO-1000 °C shows very reproducible results in this region. The particles of the LNMO-800 °C sample are nano-sized and not really well shaped (see Figure 5.3). They have a high surface area which in contact with the electrolyte may cause undesirable side reactions resulting in poor cycling performance [63]. The reason for the different character for the first 100 cycles of LNMO-800 °C sample might be that due to high surface area which in contact with the electrolyte may cause the decomposition of the electrolyte which results in development of solid electrolyte interface (SEI). In contrast, the capacity retention is higher for the material synthesized at 1000 °C which could be attributed to the bigger particle size with pseudo-octahedral shape, smooth surface and reduced surface area available for parasitic reactions [1]. The avarage capacity retentions after 300 cycles for LNMO-800 °C and LNMO-1000 °C are 42 % and 79.5 %, respectively [2].
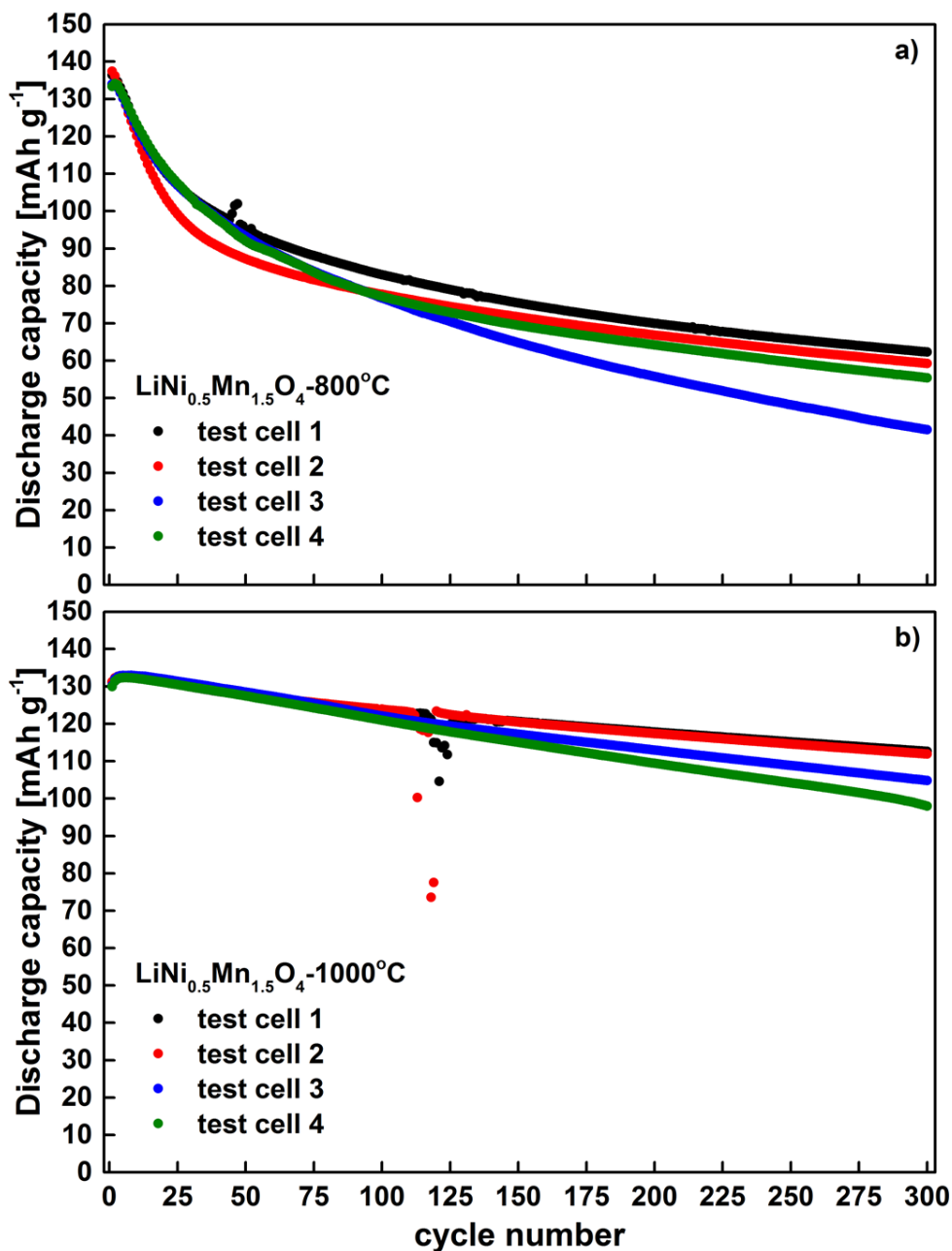
Figure 5.5: Discharge capacity vs. cycle number plots of LNMO-800 °C and LNMO-1000 °C cathode materials cycled at C/2 charge-discharge rate in a voltage range 3.5-5.0 V at RT .

5.1.4.3 Rate Capability

Besides cycle life, the battery should also show good performance at different current rates applied. In another words, the delivered capacity obtained at different C-rates should not differ too much. In this work, the charging rate was hold constant at

C/2 and the discharge rates were varied for 5 cycles for each rate to investigate the rate capability of the cathode materials. The high-rate performances of LNMO-800 °C and LNMO-1000 °C cathode materials prepared with the wet thickness of 120 μm (mass loading is $\sim$2 mg and final electrode thickness is 12 μm without the thickness of Al foil) and with the wet thickness of 300 μm (mass loading is $\sim$4.5 mg and final electrode thickness is 25 μm without the thickness of Al foil), respectively, are displayed in Figure 5.6. After applying high discharge rates, as a last step, the initial discharge current rate (C/2) was applied again to see if the system regains its initial capacity. The discharge capacities as percentages of the capacity delivered at C/2 for the two mass loadings of LNMO samples are also listed in Table 5.3. The samples synthesized at 1000 °C have superior high rate-performance compared to the samples synthesized at 800 °C. This could also be due to the strong capacity fading of the 800 °C sample during each cycling. Additionally, when the initial discharge rate (C/2) was applied as a last step to check the reversibility of the performance of LNMO-800 °C sample, it was observed that the both thin and thick electrodes cannot deliver the same capacity as they delivered at the beginning for the first 5 cycles. This observation implies that the electrochemical test cells with LNMO-800 °C electrodes have already deteriorated after applying high discharge current rates. In contrast, the delivered capacities observed for the first 5 cycles and for the last 5 cycles of LNMO-1000 °C electrodes shown in Figure 5.6 are almost the same for the thin and thick electrodes. That shows that there are no irreversible impairments which affect the electrochemical test cells seriously.
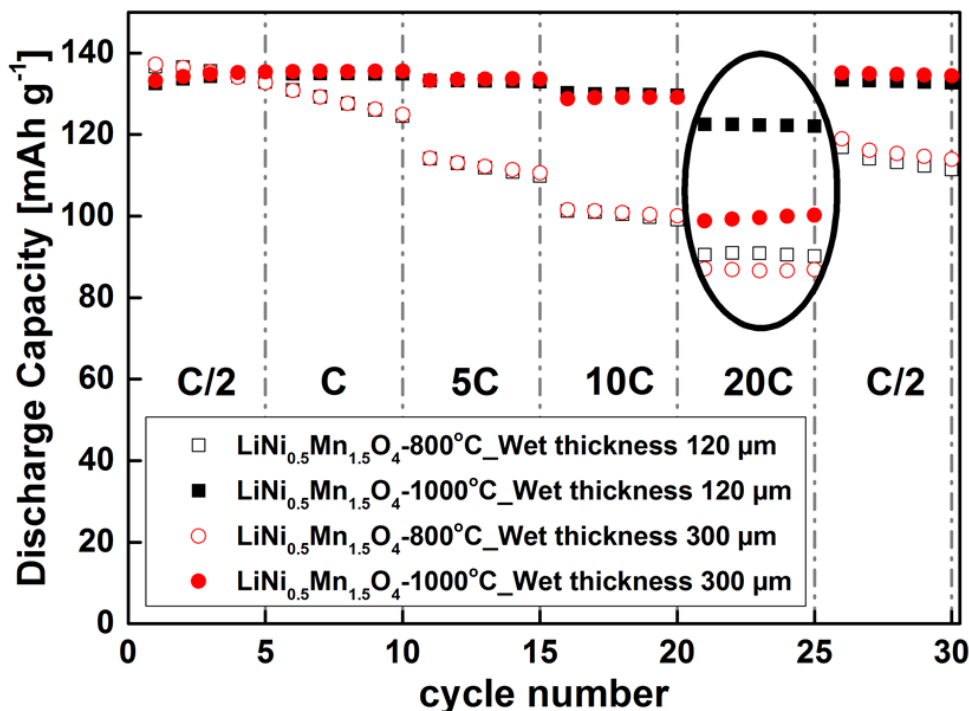
Figure 5.6: Discharge capacity vs. cycle number plots of 800 °C and 1000 °C synthesized LNMO at C/2 charge rate and varied discharge rates for electrodes with a wet thickness of 120 μm and electrodes with a wet thickness of 300 μm.

Sample	Discharge Capacity (mAh g^{-1}) at C/2		The discharge capacities as percentage of the capacity delivered at C/2 for two mass loadings							
			1C		5C		10C		20C	
	120μm	300μm	120μm	300μm	120μm	300μm	120μm	300μm	120μm	300μm
LNMO-800°C	136	136	95%	95%	83%	83%	74%	74%	67%	64%
LNMO-1000°C	134	134	100%	100%	99%	99%	97%	96%	91%	74%

Table 5.3: The discharge capacities obtained at different C-rates for LNMO cathode materials for two different mass loadings.

Hence, up to 10 C the applied electrode thicknesses and mass loadings do not play a critical role in the capacities delivered. However, at 20 C the capacities delivered are much more dependent on the mass loadings. Since the thickness of the electrodes (mass loading) plays an important roles on rate performances especially at high C-rates, for the other element doped samples, only the electrodes with the wet thickness of 120 μm have been used [2].

48

5.1.5 Electrochemical Performance of LiNi$_{0.5}$Mn$_{1.5}$O$_4$-1000 °C Cathode Material at Elevated Temperature (55 °C)

5.1.5.1 Cycling Stability

Cycling a battery at elevated temperatures may decrease the internal resistance thereby speeding up the electrochemical reactions in it which could result in higher performance at the beginning of the cycling. However, this condition may effect the cycle life negatively, as it can promote some degradation phenomena which would occur on each components of the battery mostly at the electrode-electrolyte interface. The cathode materials have been cycled at 55 °C which is the temperature mostly used in literature [1, 6, 24, 64].

The amount of electrolyte that has been used for the electrochemical experiments at room temperature was 200 μL. However, the test cells with the same amount of electrolyte showed very fast capacity fading after couple of cycles when the experiments were carried out at 55 °C. This experiments was repeated three times for LNMO-1000 °C which is shown in Figure 5.7. The sudden decrease in the discharge capacity seems not to be related with the sample performance but maybe with the stability of the test cells at elevated temperature. The results of the repeated experiments also show that the cycling behavior at 55 °C is not really reproducible after certain number cycles which was obtained for all samples investigated in this work. Long term measurements at 55 °C cause more reproducibility issues. Therefore, it should be noted that the cycling stability data obtained at 55 °C for the rest of the samples will present where the reproducible behavior can be seen.
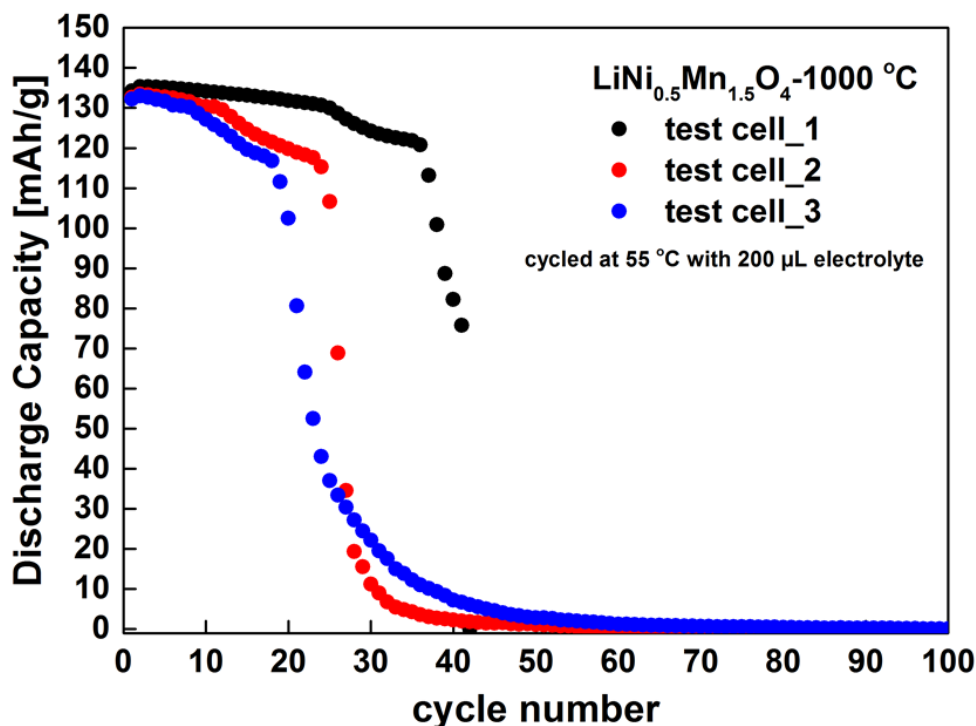
Figure 5.7: Discharge capacity vs. cycle number plots of LNMO-1000 °C cathode material cycled at C/2 charge-discharge rate in a voltage range 3.5-5.0 V at 55 °C with 200 μL electrolyte.

To check if the capacity fading is related to the electrolyte consumption or drying during cycling, sequential cycling stability tests of LNMO-1000 °C cathode material at 55 °C with different amount of electrolyte has been carried out. The best result obtained was with 325 μL electrolyte per test cell (see Figure 5.8). The cells were cycled between the voltage range of 3.5-5.0 V. All cells have been checked after cycling and there were no drying out problem of the electrolyte. Another problem might be electrolyte decomposition at high temperature and at high voltages. Because of this reason, all cycling stability experiments at 55 °C have been carried out by using 325 μL electrolyte for all other samples investigated in this work.
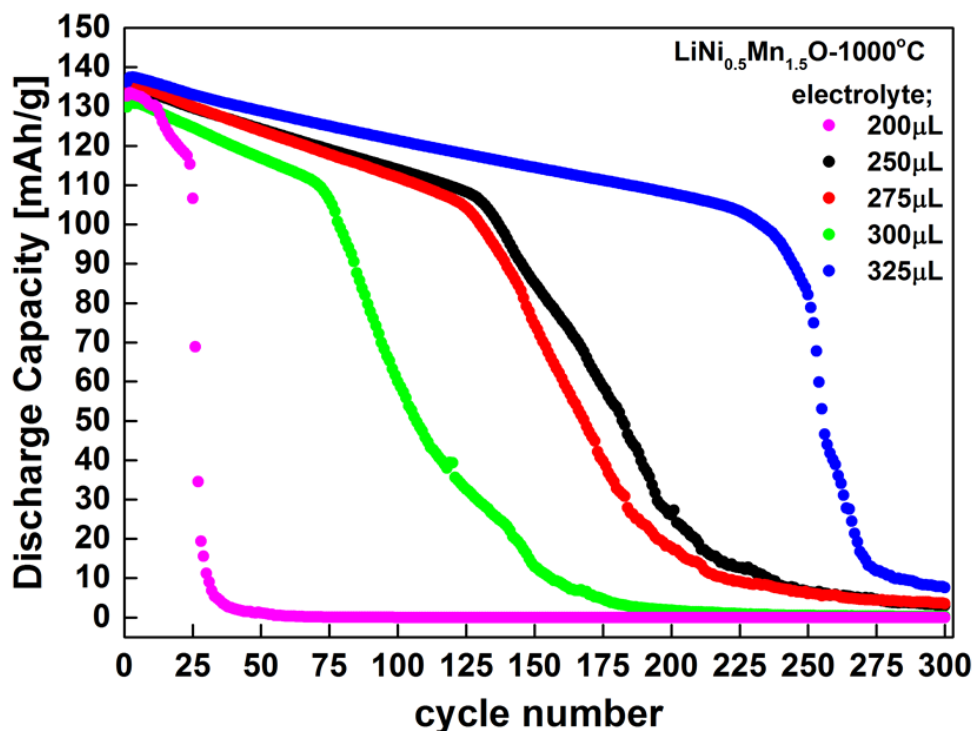
Figure 5.8: Discharge capacity vs. cycle number plots of LNMO-1000 °C cathode material cycled at C/2 charge-discharge rate in a voltage range 3.5-5.0 V at 55 °C with different amounts of electrolyte.

The LNMO-1000 °C cathode material showed good capacity retention when it was cycled with C/2 and with 325 μl electrolyte at 55 °C. It has an initial capacity of $\sim$ 136 mAh g^{-1} and a capacity retention of 75 % after 225 cycles. The capacity fading is then $\sim$ 0.11 % per cycle which is less than in some literatures [24, 34, 65]. The pronounced capacity fading was obtained after 225 cycles.

Even a small amount of Mn^{3+} remains in LNMO structure, it has mainly Mn with tetravalent state which prevents the Mn dissolution in the electrolyte that contains acidic species. It has been reported that Mn dissolves in the electrolyte containing acidic species [66, 67] when it has its trivalent state due to a disproportionation reaction;

$$2Mn^{3+}_{(solid)} \longrightarrow Mn^{4+}_{(solid)} + Mn^{2+}_{(solution)} [5]$$
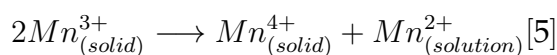
The reason for the good capacity retention after 225 cycles at 55 °C might be the reduced amount of Mn dissolution into the electrolyte. Additionally, LNMO-1000 °C has micron range sized and good crystalline particles (see Figure 5.3b) with low surface area. Therefore, side reactions in high voltage region at elevated temperature can be reduced. The negative effect of these conditions was obtained after relatively high number of cycles (after 225 cycles).

5.1.6 Investigations on Structural Evolutions of $LiNi_{0.5}Mn_{1.5}O_4$-1000 °C Cathode Material during Electrochemical Cycling using Synchrotron Diffraction

Understanding the mechanisms influencing the lifetime of a cell is of greatest importance and within that the structural aspects play a key role. The structural changes such as phase transitions (if present), lattice parameters, phase ratios, microstructure parameters (crystallite size, strain) etc. inside the electrode materials during charging and discharging can be understood with *in situ* diffraction studies. The study of structural changes occurring during lithiation / de-lithiation is critical for understanding of degradation phenomena. In this work , only thick electrodes (wet thickness 300 μm) with $\sim$4.5 mg active material and 25 μm final thickness were used for all samples for *in situ* diffraction studies during cycling in order to obtain enough intensity in diffraction patterns.

5.1.6.1 Analysis of Synchrotron Diffraction Patterns Obtained During 1st Charging and Discharging at C/2 Current Rate

Figure 5.9 displays the 1st charging and subsequent discharging voltage profiles of the LNMO-1000 °C cathode material taken during *in situ* synchrotron diffraction patterns.
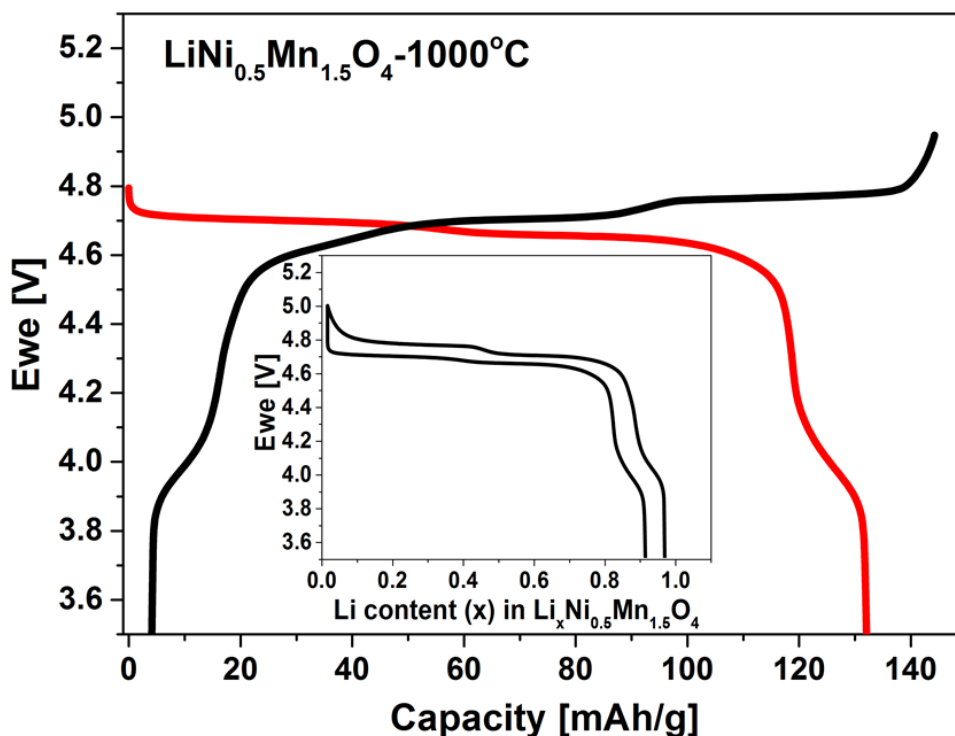
Figure 5.9: The first charge (black) - discharge (red) voltage profiles corresponding to the *in situ* synchrotron diffraction patterns for LNMO-1000 °C cathode material between 3.5-5.0 V cycled at C/2 charge-discharge rate.

The LNMO-1000 °C cathode material was cycled with a charge/discharge rate of C/2 in the voltage range 3.5-5.0 V. Fast experiments with short exposure times at synchrotron sources are essential to monitor structural changes under exactly the same conditions as during battery operation. This behavior is different from the results of slow experiments with a laboratory X-ray diffractometer, which can reveal changes closer to equilibrium, but essentially different from the conditions in an operating energy storage device. It should be noted that the electrochemical performance obtained with *in situ* cell is similar to that obtained with the standard Swagelok®-type cell. The voltage profiles show a re-intercalation of ∼0.90 moles of lithium into LNMO-1000 °C with *in situ* cell which was ∼ 0.95 moles of lithium in the case of Swagelok®-type cell.
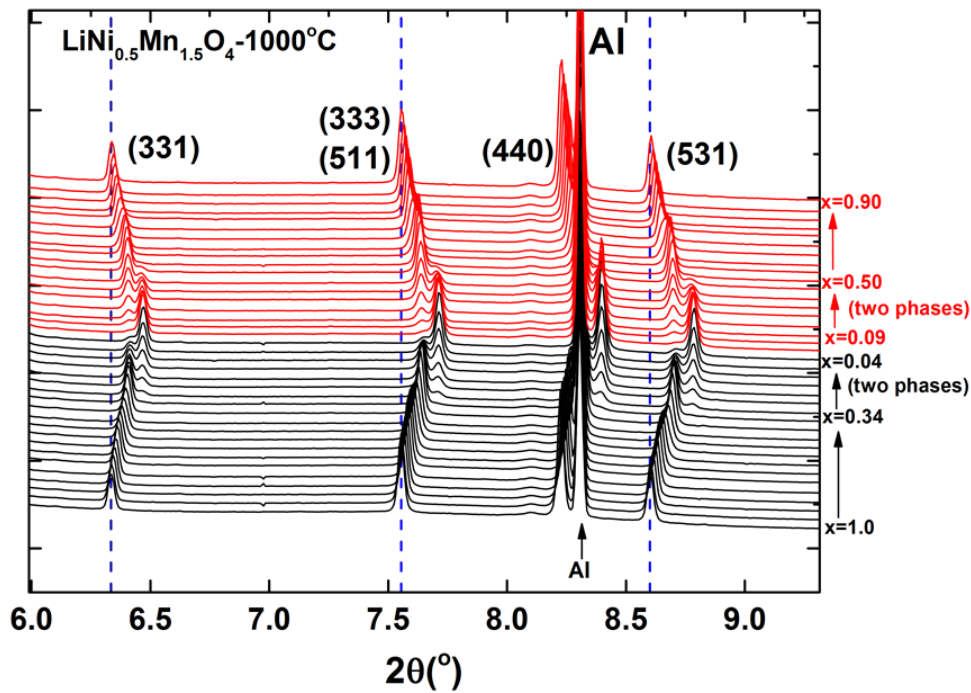
Figure 5.10: Selected 2θ regions of *in situ* synchrotron diffraction patterns of LNMO-1000 °C measured at beamline P02.1 during the 1st cycle.

The structural evolution during charge and discharge processes for LNMO-1000 °C are displayed in Figure 5.10 for selected 2θ regions, where black and red lines correspond to the charge and discharge regions, respectively. For initial state of charge (up to x = 0.34), the delithiation occurs via solid solution mechanism. The reflections shift to higher 2θ values, in accordance with a shrinkage of the unit cell upon lithium extraction. At higher degree of delithiation, an additional cubic spinel phase appears with the same space group ($Fd\overline{3}m$) as the initial phase, but with a different lattice parameter, which can clearly be seen in Figure 5.11.
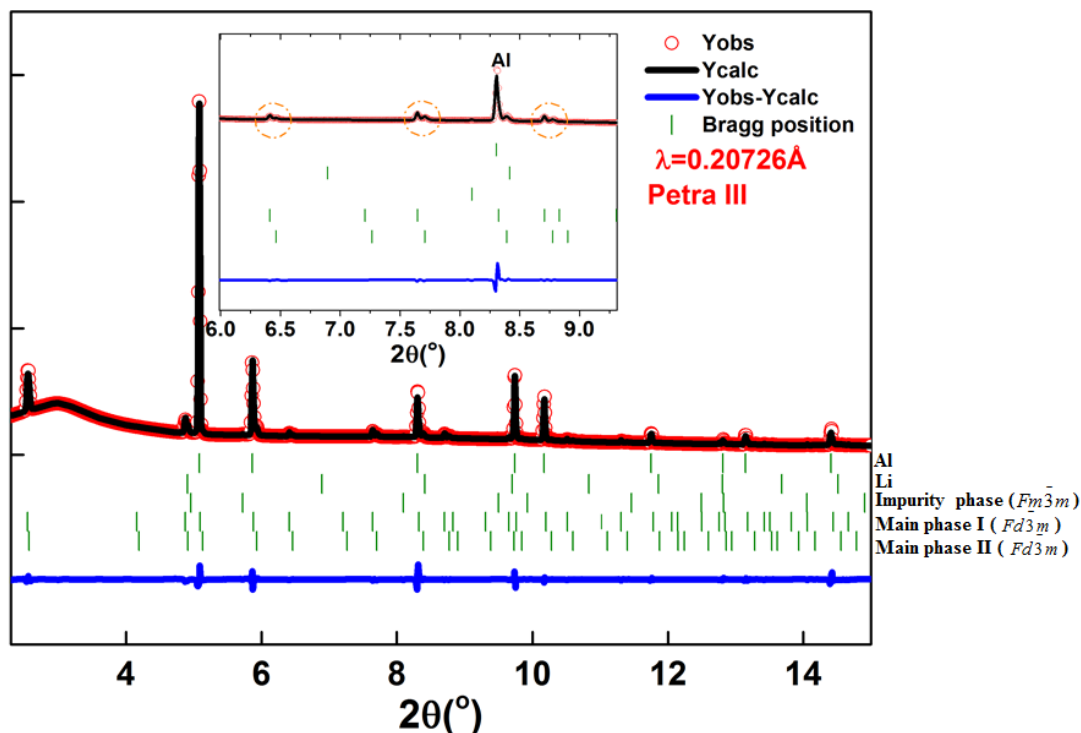
Figure 5.11: Synchrotron diffraction pattern of $Li_{0.24}Ni_{0.5}Mn_{1.5}O_4$-1000 °C observed during the charging process at ~4.77 V corresponding to 0.24 moles of remaining Li in the structure.

The second phase in LNMO-1000 °C cathode material was observed until the end of charge (existence of two phases between x = 0.34-0.04 during charging) and reversibly continues until approximately half of the Li ions are re-intercalated during discharge (existence of two phases between x = 0.34-0.04 during discharging). "x" is defined as the nominal number of moles of Li that remains in the structure, calculated from the number of electrons flowing through the circuit. Figure 5.12 displays the evolution of the lattice parameter as a function of the Li content for the LNMO-1000 °C sample. The unit cell parameter of the second cubic spinel phase undergoes a constant decrease and increase during charging and discharging, respectively, similar to the main cubic spinel phase, which proves that the new phase formed is also electrochemically active.
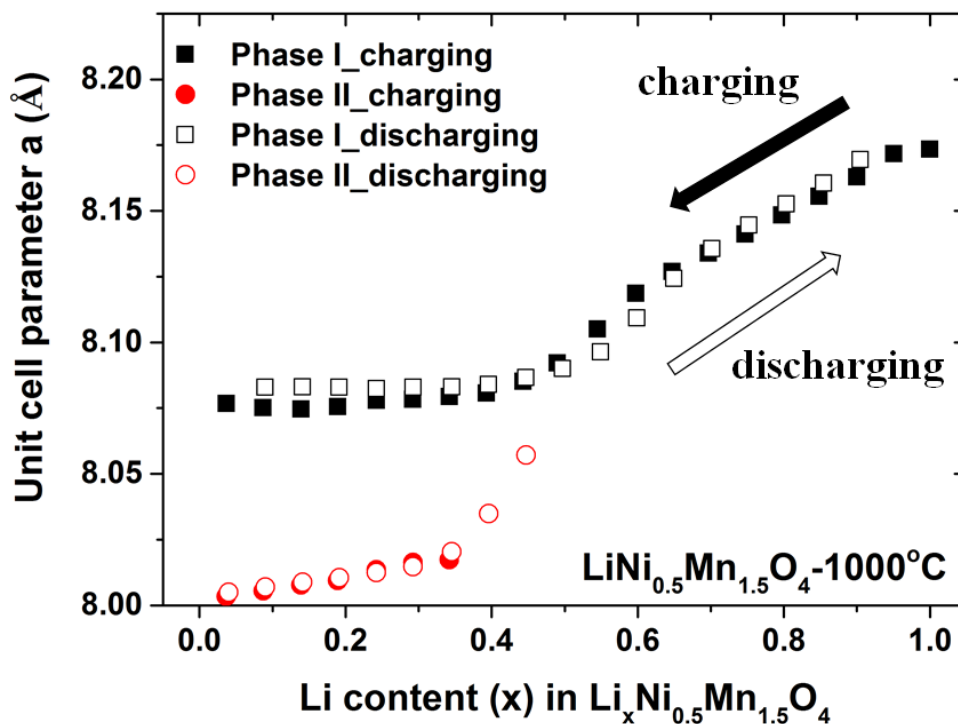
Figure 5.12: Change in the unit cell parameter as a function of number of moles of Li (x) remaining in the structure for $Li_xNi_{0.5}Mn_{1.5}O_4$-1000 °C. The red circles represent the unit cell parameter changes of the additional spinel phase.
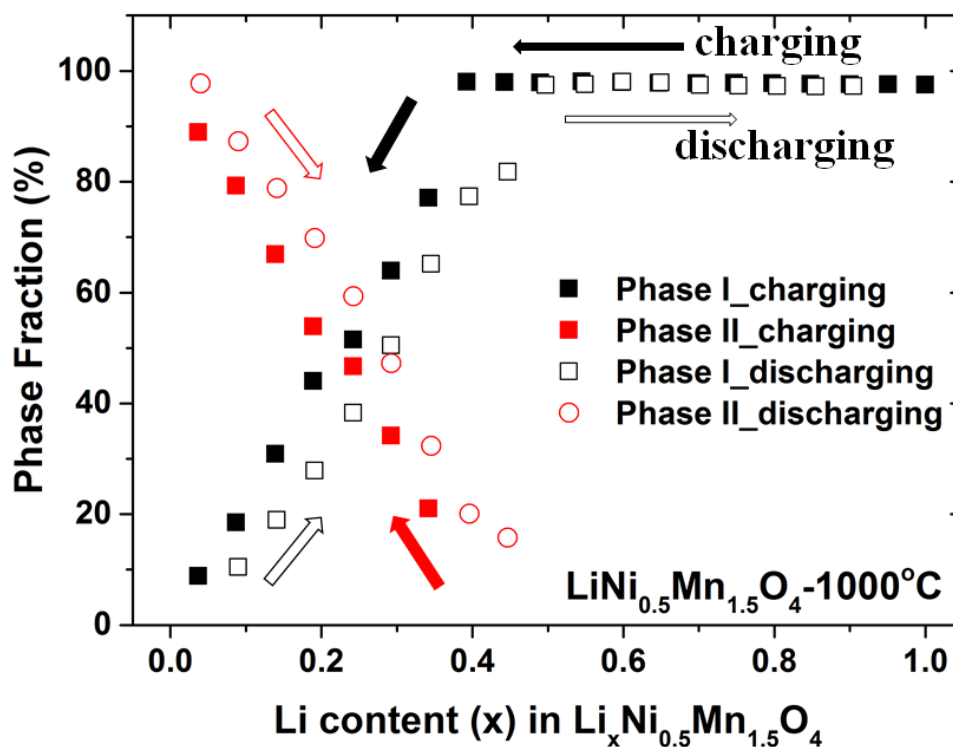
Figure 5.13: The phase ratios vs. Li content during cycling for $Li_xNi_{0.5}Mn_{1.5}O_4$-1000 °C.

Apparently, the phase transition obtained until end of the charge is reversible be-cause it disappears upon discharging process. The phase fraction analysis shown in Figure 5.13 supports this assumption.

The shrinkage of the unit cell at the end of the first charge obtained from Rietveld refinement are 1.18 % and 2.08 % for LNMO-1000 °C for both spinel phases at the end of the 1st charge (see table 5.4). The shrinkage differences are small. The lattice ex-pansions during discharging are 1.13 % and 2.03 % for both phases of LNMO-1000 °C. They are calculated from the lattice parameter differences between the end of the 1st charge and the end of the 1st discharge. This indicates the re-insertion of remarkable amounts of Li ions back into the structure.

	LNMO		
	Lithium content	$a(\mathring{A})$	Shrinkage/ Expansion(%)
Initial	1	8.1733(1)	
End of 1st charge	0.0370	8.077(2) 8.0034(4)	1.18 2.08
End of 1st discharge	0.9047	8.1694(2)	1.13 2.03

Table 5.4: Rietveld refinement results based on *in situ* synchrotron diffraction of LNMO-1000 °C. (The percentage of the shrinkage is the difference between the initial state and end of 1st charge and the percentage of the expansion is the dif-ference between the end of 1st charge and end of 1st discharge)

The micro-strain analysis obtained by Rietveld refinement of the LNMO-1000 °C sample is shown in Figure 5.14. An increase in the lattice strain was observed at the voltage points where the Ni^{2+}/Ni^{4+} redox couple is active. The lattice strain on the structure especially when two phases exist deviate considerably. That would cause much stress on the structure during Li insertion/deinsertion which can negatively in-fluence the kinetic or cycling stability.
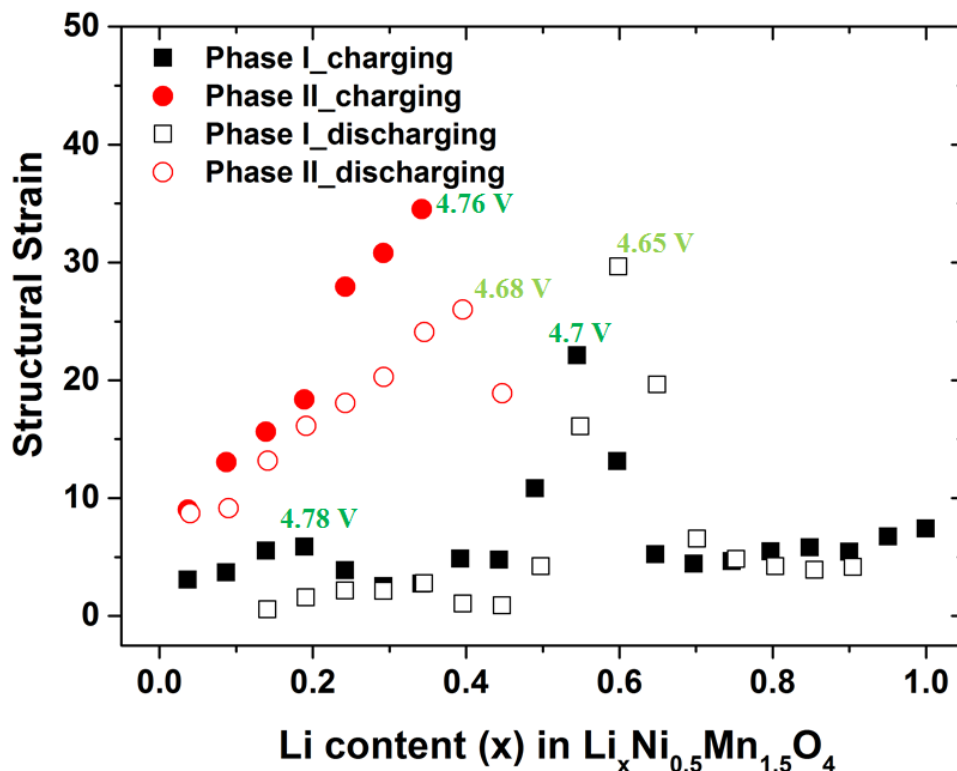
Figure 5.14: The micro-strain analysis of $LiNi_{0.5}Mn_{1.5}O_4$-1000 °C cathode material. The maximum strain is given in the Fullprof microstructural output file as $\frac{\Delta d}{d} \times 10^{-4}$.

5.1.6.2 Analysis of Synchrotron Diffraction Patterns Obtained During Discharging at 5 C and 10 C Current Rates

In order to monitor the structural changes during faster discharging, the same *in situ* cell already cycled at a C/2 rate was used. The cell was charged a second time at C/2 and discharged at 5 C and as a last step it was charged a third time at C/2 and discharged at 10 C. In this section, the structural evolution obtained during discharging at 5 C and 10 C will be taken into account. The exposure time for one XRD pattern during fast discharging was 5 seconds and the patterns were obtained from each cell individually for this experiment in order to get enough XRD patterns to be able to track structural changes in each voltage range.

Figure 5.15 displays the voltage profiles of the LNMO-1000 °C cathode material charged at C/2 and discharged at 5 C and 10 C, respectively, corresponding to the re-

spective *in situ* synchrotron diffraction patterns.
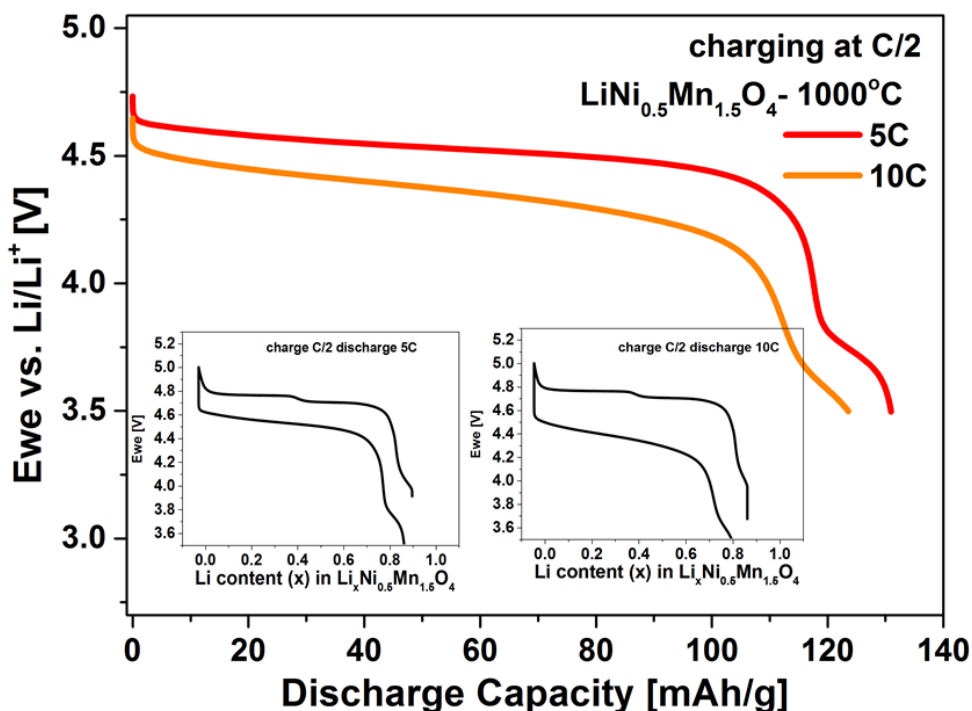
Figure 5.15: The voltage profiles corresponding to the *in situ* synchrotron diffraction patterns for LNMO-1000 °C cathode material between 3.5-5.0 V charged at C/2 and discharged at 5 C and 10 C, respectively.

The capacity loss can clearly be seen when the discharge rate is increased from 5 C to 10 C. The 4 V plateau becomes less visible and in addition, the high-voltage plateau ∼4.7 V diminishes for both discharging rates. The delivered discharge capacities at 5 C (131 mAh g^{-1}) and 10 C (123 mAh g^{-1}) are slightly less than those observed with Swagelok cells (see Figure 5.6). The reason for this difference could be attributed to the bulky construction of the *in situ* cells which have glass windows sealing those are not as hermetic as the Swagelok cells against air contact. In addition, thick electrode with 4.5 mg active material was used which is not optimized for high C-rates.

The structural evolution during the discharge process at 5 C and 10 C for LNMO-1000 °C is displayed in Figure 5.16a and b with selected 2θ regions. The kinetic effects on structure during cycling processes have not been investigated so far. This new ob-

servation shows that a faster discharging leads to the existence of a third spinel phase ($Fd\bar{3}m$) which disappeared at the end of the discharging process for both 5 C and 10 C discharge rates.
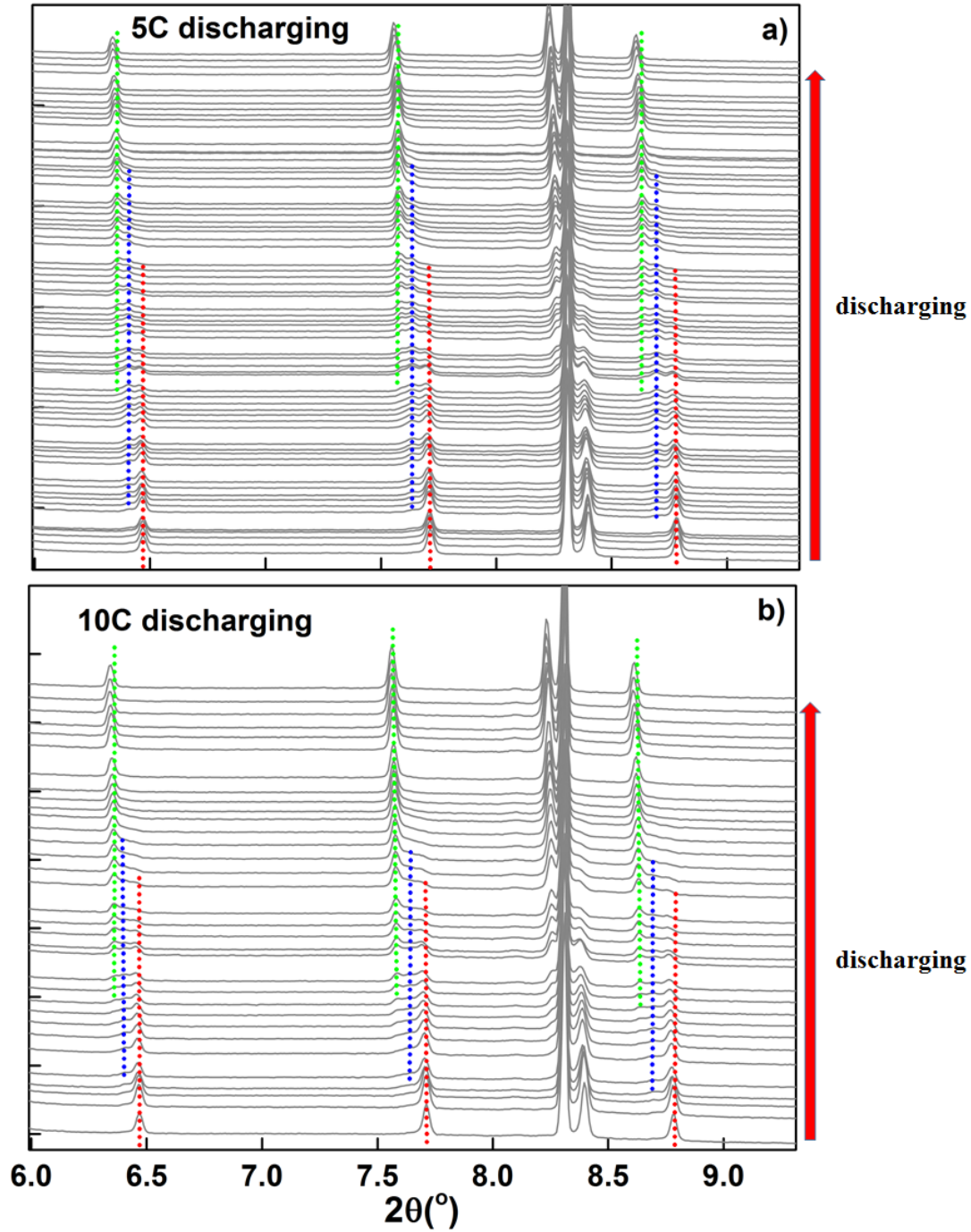
Figure 5.16: Selected 2θ regions of the *in situ* synchrotron diffraction patterns of LNMO-1000 °C measured at P02.1 during discharging at a) 5 C and b) 10 C.

The results of the Rietveld refinements of the diffraction patterns at 5 C discharge rate are displayed in Figure 5.17a, b and c showing a change in lattice parameter, phase fractions and the micro-strain parameters, respectively. Similarly, Figures 5.17d, e and f show the change in lattice parameter, phase fractions and micro-strain at 10 C discharge rate. According to the evaluation of the diffraction patterns, the third spinel ($Fd\bar{3}m$) phase evolves in the structure during both 5 C and 10 C discharging process which is absent when cycled at C/2 rate.

At the beginning as well as at the end of the discharging processes, there is only one spinel phase. This observation indicates that the formation of the second and third spinel phase is completely reversible and due to the constant changes in the lattice parameter for all three phases, it can be said that they are involved in the electrochemical reactions, like in the process at C/2 rate. Moreover, the lattice strain observed during 5 C and 10 C discharge rate is higher than that at C/2.
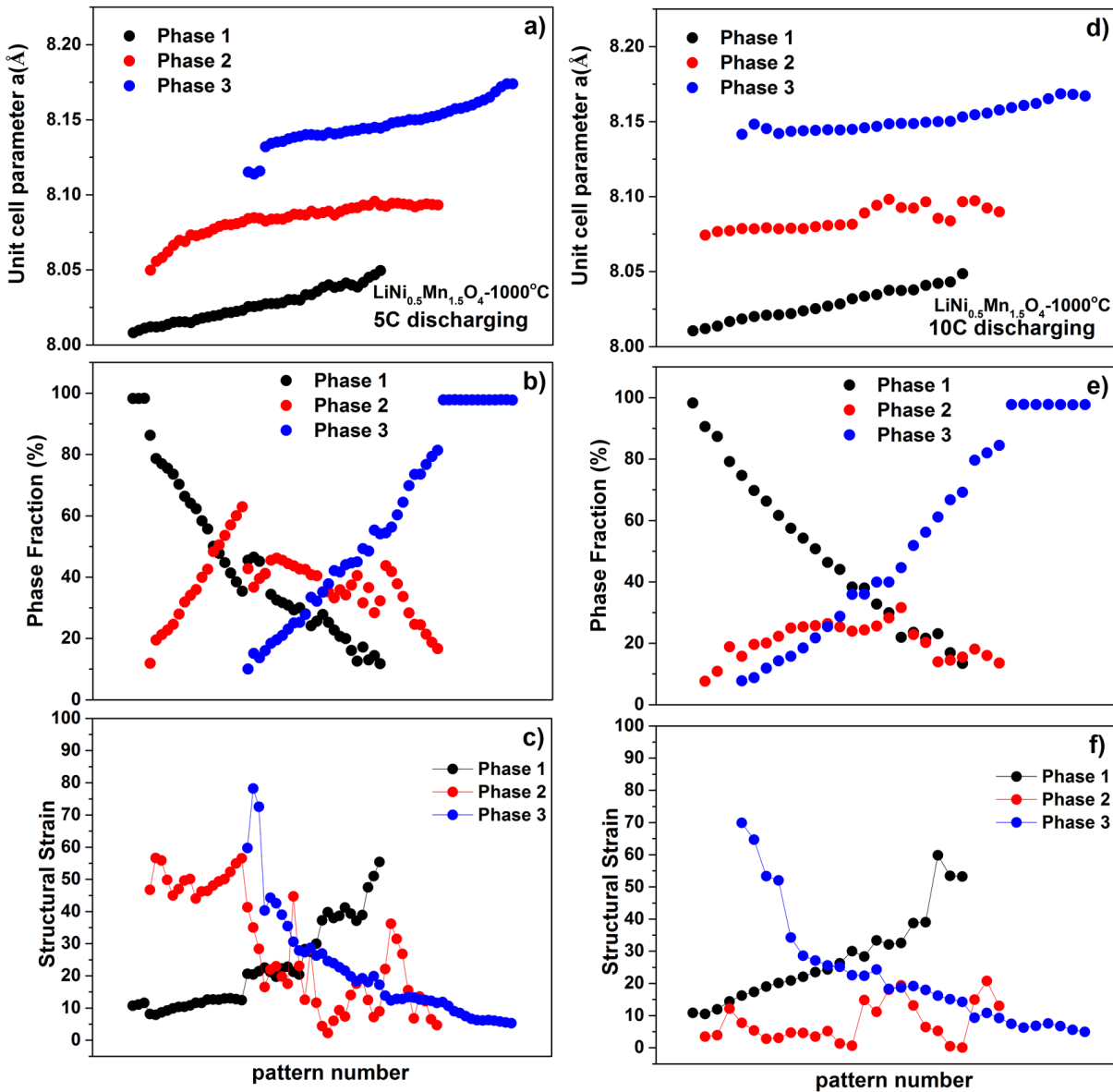
Figure 5.17: Structural parameters from synchrotron diffraction patterns of LNMO-1000 °C measured at beamline P02.1 during discharging at 5 C and 10 C. a) Change in the lattice parameter during 5 C discharging rate b) Change in the phase ratios during 5 C discharging rate c) Micro-strain analysis during 5 C discharging rate d) Change in the lattice parameter during 10 C discharging rate e) Change in the phase ratios during 10 C discharging rate f) Micro-strain analysis during 10 C discharging rate.

It can be concluded that the Li de-/intercalation in LNMO takes place via both solid solution mechanism and phase transition depending on the state of charge. Additionally, our *in situ* experiments with different C-rates show that the character of the structural changes depends on the current density applied. The structure undergoes

extra phase transition when the current rate was increased which causes higher strain on the lattice that effects the electrochemical performance.

5.2 Ru-doped $LiNi_{0.5-2x}Ru_xMn_{1.5}O_4$ (x=0.05) Spinel as High-Volt Cathode Material

This section focuses on the influence of Ru-doping on LNMO concerning structure, morphology and electrochemical performances. The idea of synthesizing $LiNi_{0.5-2x}Ru_xMn_{1.5}O_4$ material is based on producing octahedral vacancies in the spinel structure [15]. When Ni is partially replaced with the transition metal Ru, the oxidation state distribution changes from $Li^+Ni_{0.5}^{2+}Mn_{1.5}^{3+/4+}O_{4-\delta}$ to $Li^+Ni_{0.4}^{2+}Ru_{0.05}^{4+}Mn_{1.5}^{3+/4+}O_{4-\delta}$. As a result, in the ideal case, there will not be 2 moles of transition metals in the spinel structure but less.

The details on the structure, morphology, cycling stability, rate capability and electrochemical mechanism will be discussed in the following text in comparison with the parent compound LNMO synthesized at both 800 °C and 1000 °C. For the comparison of electrochemical performances like CV, cycling stability and rate capacibility, electrodes with very similar mass loadings were used.

5.2.1 Structural Analyses

Figure 5.18 shows the synchrotron diffraction patterns of $LiNi_{0.4}Ru_{0.05}Mn_{1.5}O_4$ (LNRMO) samples synthesized at 800 °C and 1000 °C, respectively.
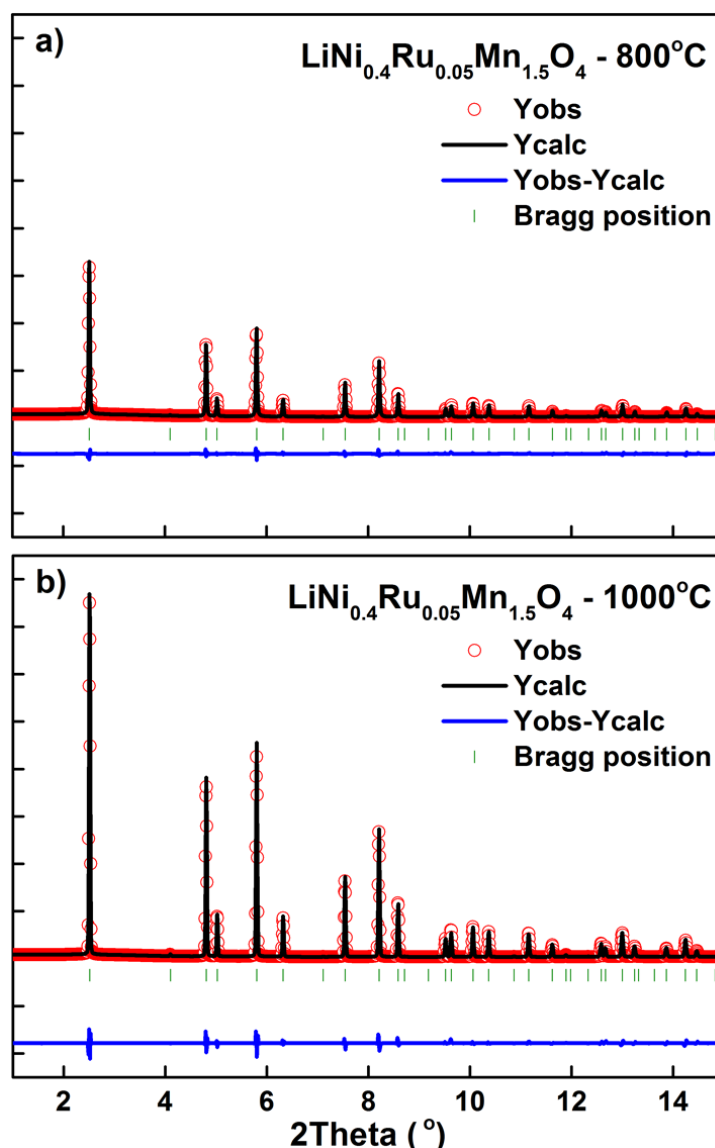
Figure 5.18: Rietveld refinement results based on synchrotron diffraction patterns of as prepared a) LNRMO-800 °C b) LNRM-1000 °C materials measured in 0.5 mm capillaries.

The materials have cubic spinel structure with $Fd\overline{3}m$ space group as in the case of the undoped LNMO samples. However, these materials are phase pure, no additional impurity phases are detectable with synchrotron diffraction. This observation implies that Ru doping suppresses the formation of an additional phase. In other words, Ru doping makes the structure more stable against formation of second phase. Moreover, the obtained lattice parameters listed in Table 5.5 are larger for the Ru-doped samples than the undoped ones. The ionic radii of Ni^{2+} and Ru^{4+} are 0.69 Å and 0.62 Å, respec-

tively. Because of this difference, it is expected that the Ru-doped samples should have smaller lattice parameters than the parent LNMO samples. The reason for a larger lattice parameter might be due to a higher amount of oxygen deficiency for the Ru-doped samples, hence, resulting in a higher amount of Mn^{3+} which has larger lattice parameter (0.645 Å) than Mn^{4+} (0.53 Å).

Samples	Atom Site	x=y=z	a(Å)	Volume (Å^3)	Fraction of impurity phase %	Overall Temperature Factor (B$_o$v)	R$_{wp}$(%)
LNRMO-800°C	Li$_{8a}$ Ni$_{16d}$ Mn$_{16d}$ Ru$_{16d}$ O$_{32e}$	0.125 0.500 0.500 0.500 0.2631(3)	8.1830(1)	548(1)	-	0.36	5.12
LNRMO-1000°C	Li$_{8a}$ Ni$_{16d}$ Mn$_{16d}$ Ru$_{16d}$ O$_{32e}$	0.125 0.500 0.500 0.500 0.2633(3)	8.1889(1)	549(1)	-	0.44	6.8

Table 5.5: Rietveld refinement results of LNRMO samples based on synchrotron diffraction data (space group $Fd\bar{3}m$).

The neutron diffraction data of initial LNRMO-1000 °C powder also shows that the material is phase pure and again confirms that Ru is inside the spinel structure on the *16d* site (see Figure 5.19). Since the scattering lengths are different for Ni, Mn and Ru (10.3 fm, -3.73 fm and 7.03 fm, respectively), it is possible to obtain their stoichiometries by refining the site occupancies independently for all three cations. The calculated stoichiometry from refined site occupation factors (which were refined independently) based on the Rietveld refinements of neutron data is $Li_{1.0512}Ni_{0.4044}Ru_{0.04224}Mn_{1.5552}O_4$. This shows a slight Mn excess.
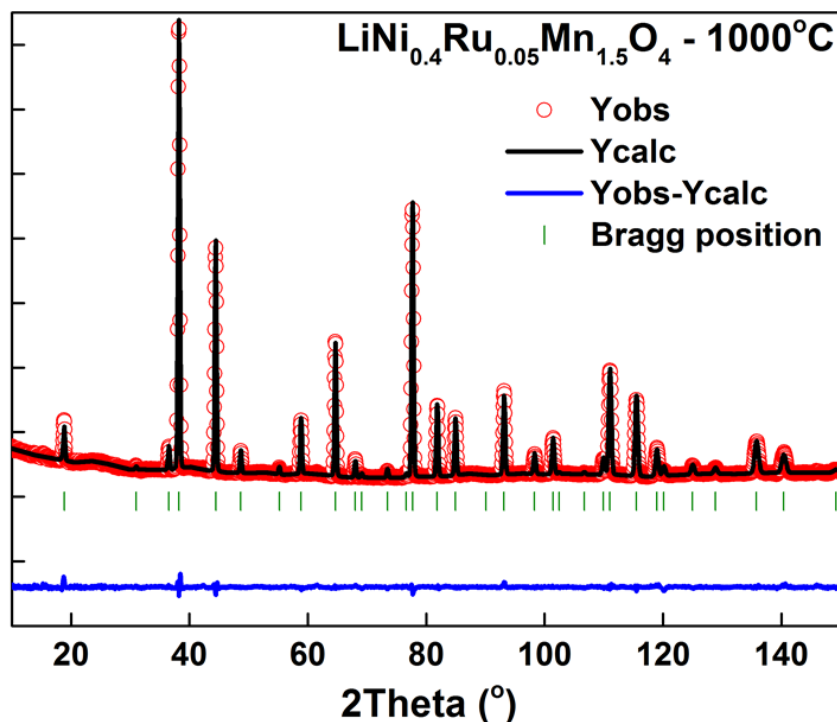
Figure 5.19: Rietveld refinement results based on neutron diffraction pattern of as pre-pared LNRMO-1000 °C powder.

5.2.2 Chemical Analysis (ICP-OES)

Table 5.6 gives the Li/transition metals ratios of the LNRMO samples synthesized at 800 °C and 1000 °C as determined from ICP-OES analysis. The observed values were calculated assuming that Li has complete stoichiometry and the results show that no significant difference is detectable between the samples synthesized at 800 °C and 1000 °C.

Sample	Ratio of Li: Transition Metals (expected)	Ratio of Li: Transition Metals (observed)	Ratio of Transition Metals Ni:Mn:Ru (observed)
LNRMO-800 °C	0.5128	0.5071	0.4048 : 1.4853 : 0.0421
LNRMO-1000 °C	0.5128	0.5071	0.3931 : 1.4853 : 0.0439

Table 5.6: The results of ICP-OES analyses of LNRMO-800 °C and LNRMO-1000 °C.

5.2.3 Morphology Studies of initial LiNi$_{0.4}$Ru$_{0.05}$Mn$_{1.5}$O$_4$ powder

SEM images of LNRMO-800 °C and LNRMO-1000 °C are presented in Figure 5.20a-b, respectively. The LNRMO particles obtained after the annealing at 800 °C have similar properties as the parent LNMO samples. They also lack well defined edges and the particle sizes are in the range of 50-200 nm. In contrast to the LNRMO-800 °C, the particles of the materials synthesized at 1000 °C exhibit pseudo-octahedral shape with smoother surfaces and a size range of 0.5-1 μm for LNRMO-1000 °C.
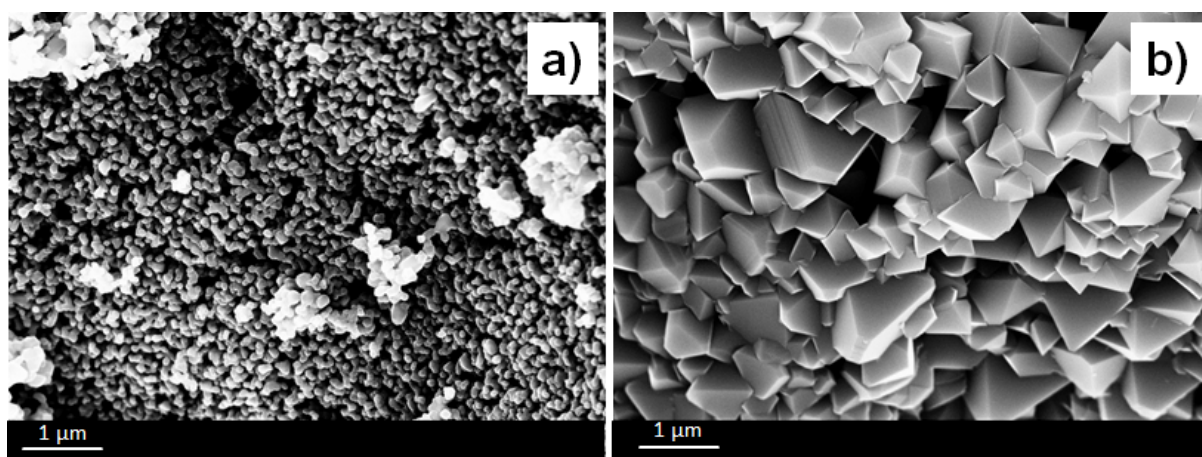
Figure 5.20: SEM images of as prepared a) LNRMO-800 °C, b) LNRMO-1000 °C powders.

5.2.4 X-Ray Absorption Spectroscopy (XAS) Analysis of LNRMO-1000 °C in Comparison with LNMO-1000 °C

To study the influence of Ru doping on the oxidation state of Mn and Ni, X-ray absorption near edge (XANES) spectra were analyzed for LNMO-1000 °C and LNRMO-1000 °C samples. By comparing the XANES region of the Mn K-edge of both LNMO-1000 °C and LNRMO-1000 °C with the standard MnO$_2$, it may be concluded that the Mn in both systems predominantly exist as Mn^{4+} (see Figure 5.21).
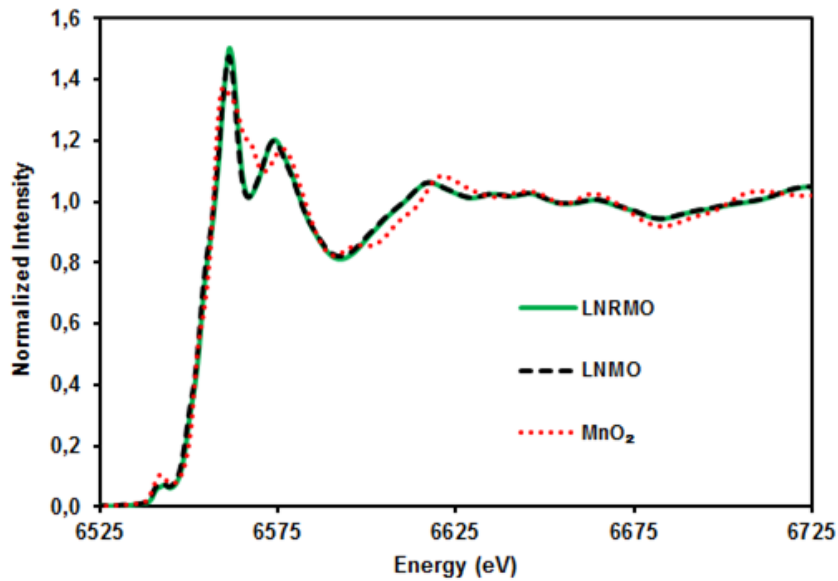
Figure 5.21: XANES of the Mn K-edge, for LNMO-1000 °C and LNRMO-1000 °C samples, as well as for the reference material MnO_2.

Direct evidence of the presence of Mn^{3+} may not be obtained from XANES, as the concentration of Mn^{3+} is too low to be detected. Recently, Rana *et al.* has correlated the Mn-O bond distance obtained from the extended X-ray absorption fine structure spectra (EXAFS) fitting to the average oxidation state of the Mn [68]. The present EXAFS fitting for both LNMO and LNRMO provides a Mn-O bond distance of 1.90 Å (see Table 5.7) which may be assigned to an average Mn-O bond distance lying between $Mn^{3.5+}$- O and Mn^{4+}- O. The EXAFS fit for both LNMO and LNRMO at the Mn edge is shown in Figure 5.22.
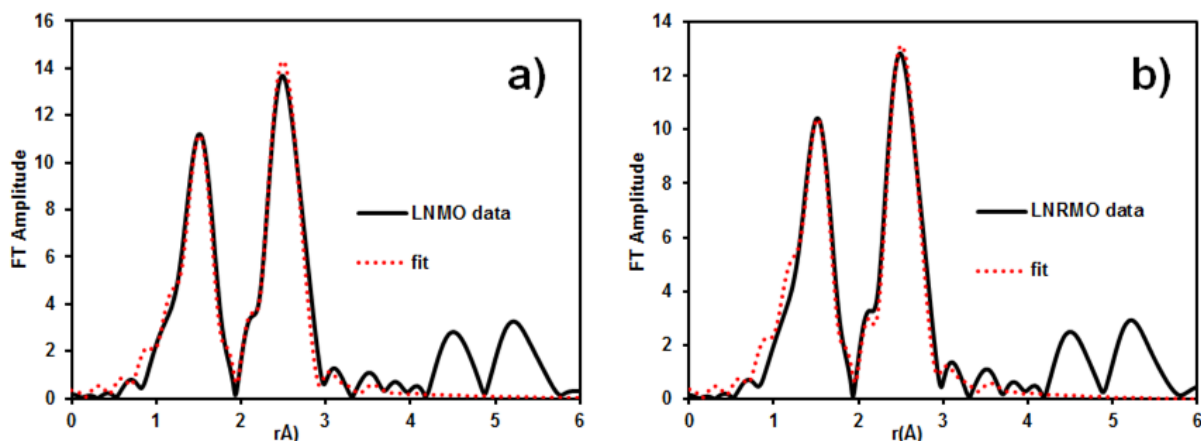
Figure 5.22: Fourier transform Mn K-edge fit of a) LNMO-1000 °C and b) LNRMO-1000 °C.

It should be emphasized that any quantification of Mn^{3+} is limited by the available data range ($\approx 2\Delta k \Delta R / \pi$) where Δk is the range of Fourier transform and ΔR is the range in direct space R over which the fit is evaluated. By comparing the measured Ni-edges with a $NiSO_4$ reference spectrum, it can be seen that Ni exists as Ni^{2+} in both the Ru-doped and undoped system (see Figure 5.23).
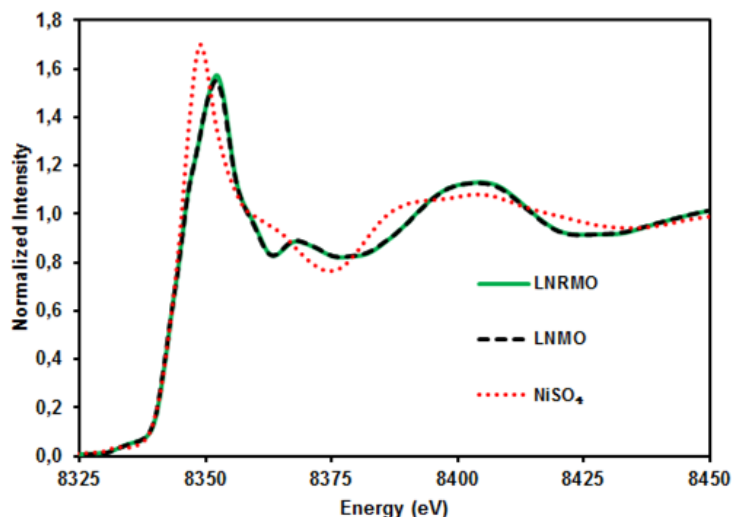
Figure 5.23: XANES of the Ni K-edge, for LNMO-1000 °C and LNRMO-1000 °C samples, as well as for the reference material $NiSO_4$.

The EXAFS fitting at Ni K-edge for both doped and undoped systems provides a

bond distance for Ni-O of 2.05 Å, which may be assigned to a Ni^{2+}- O bond distance
(see Table 5.7). The EXAFS fitting for both LNMO and LNRMO spectra at the Ni K-
edge is shown in 5.24.
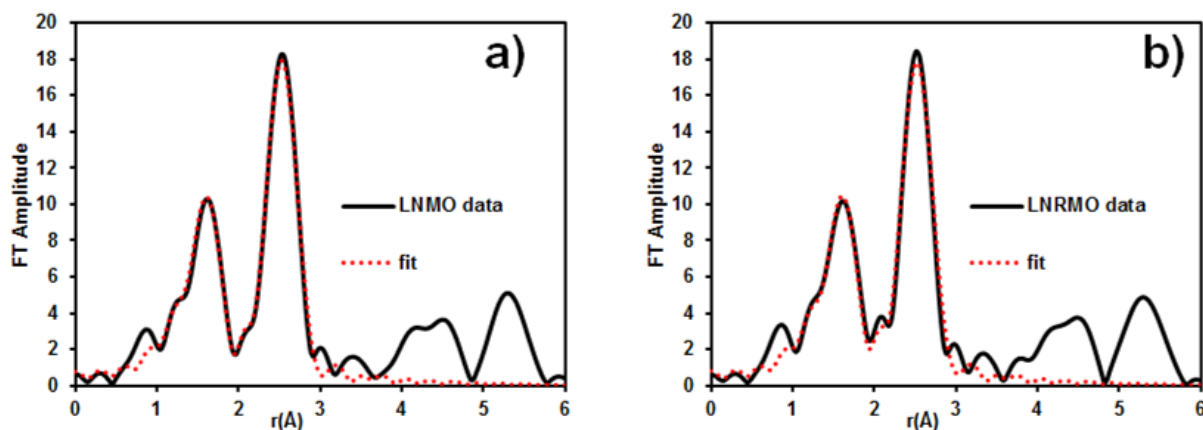
Figure 5.24: Fourier transform Ni K-edge fit of a) LNMO-1000 °C and b) LNRMO-1000
°C.

Although an identical structural model was used to fit both Mn and Ni edges, a
statistically better fit was observed for the Ni edge. This may be further attributed to
the presence of a mixed valance state of Mn which was not taken into account for fit-
ting. To confirm the presence of Ru inside the spinel structure the Ru K-edge spectra
of the Ru-doped samples were analyzed. By comparing the Ru K-edge XANES spectra
of the doped system with the reference spectra of RuO_2 it may be concluded that Ru
exists as Ru^{4+} (see Figure 5.25a).
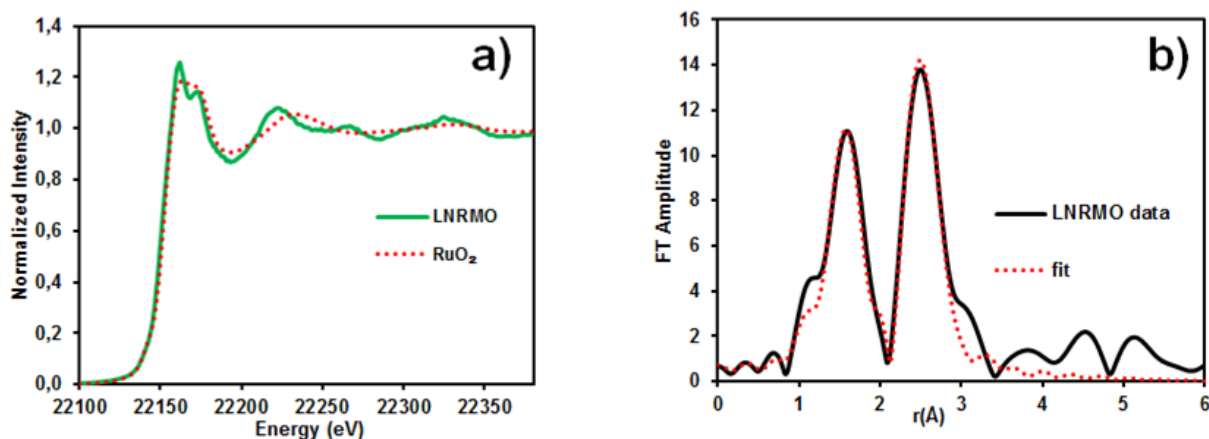
Figure 5.25: a)XANES of the Ru K-edge for LNRMO-1000 °C, as well as for the reference material RuO$_2$ b) Fourier transform Ru K-edge fit of LNRMO-1000 °C.

Furthermore, to understand the local coordination of the Ru, the EXAFS region of the XAS spectra was analyzed. The Fourier transformation (FT) of the EXAFS spectra to the r space revealed two high amplitude peaks, one at low r value (between 1 and 2 Å) and another at high r value (between 2 and 3 Å) (see Figure 5.25b). This is consistent with the FT pattern obtained at the Ni as well as Mn edges. Thus, the Ru is expected to be present inside the spinel structure. Finally the EXAFS fitting at the Ru K-edge provided a Ru-O bond distance of 2.02 Å and 2.94 Å for Ru-Ni/Mn, respectively, which are the expected values for Ru occupying the *16d* Wyckoff position in the spinel structure. The larger Ru-Mn/Ni bond distance correlate very well with the larger lattice parameter observed for the LNRMO sample comparing to LNMO.

	$LiNi_{0.5}Mn_{1.5}O_4$	$LiNi_{0.4}Ru_{0.05}Mn_{1.5}O_4$
rMn-O1($\mathring{A}$)	1.902(5)	1.903(6)
DW-Mn-O1($\mathring{A}^2$)	0.0035(6)	0.0032(6)
rMn-Mn($\mathring{A}$)	2.890(5)	2.890(5)
DW-Mn-O1($\mathring{A}^2$)	0.0036(5)	0.0033(4)
rNi-O($\mathring{A}$)	2.047(4)	2.046(5)
DW-Ni-O($\mathring{A}^2$)	0.0062(5)	0.0056(7)
rNi-Mn($\mathring{A}$)	2.920(3)	2.913(4)
DW-Ni-Mn($\mathring{A}^2$)	0.0053(3)	0.0049(4)
rRu-O($\mathring{A}$)	-	2.017(9)
DW-Ru-O($\mathring{A}^2$)	-	0.002(1)
rRu-Mn($\mathring{A}$)	-	2.940(8)
DW-Ru-Mn($\mathring{A}^2$)	-	0.0030(9)

Table 5.7: EXAFS fit results obtained for Mn, Ni, and Ru K edges.

5.2.5 Electrochemical Performances of $LiNi_{0.4}Ru_{0.05}Mn_{1.5}O_4$ Cathodes at Room Temperature (RT)

5.2.5.1 Voltage Profile Comparison of LNMO-1000 °C and LNRMO-1000 °C Cathode Materials

The voltage vs. discharge capacity plots of LNMO and LNRMO synthesized at 800 °C and 1000 °C cycled with C/2 charge-discharge rate for the 3rd cycle are shown in Figure 5.26. The Ru-doped samples exhibit higher 4 V region electrochemical activity than LNMO as revealed from the larger plateau obtained at 3.8-4.4 V voltage range

(see inset of Figure 5.26).
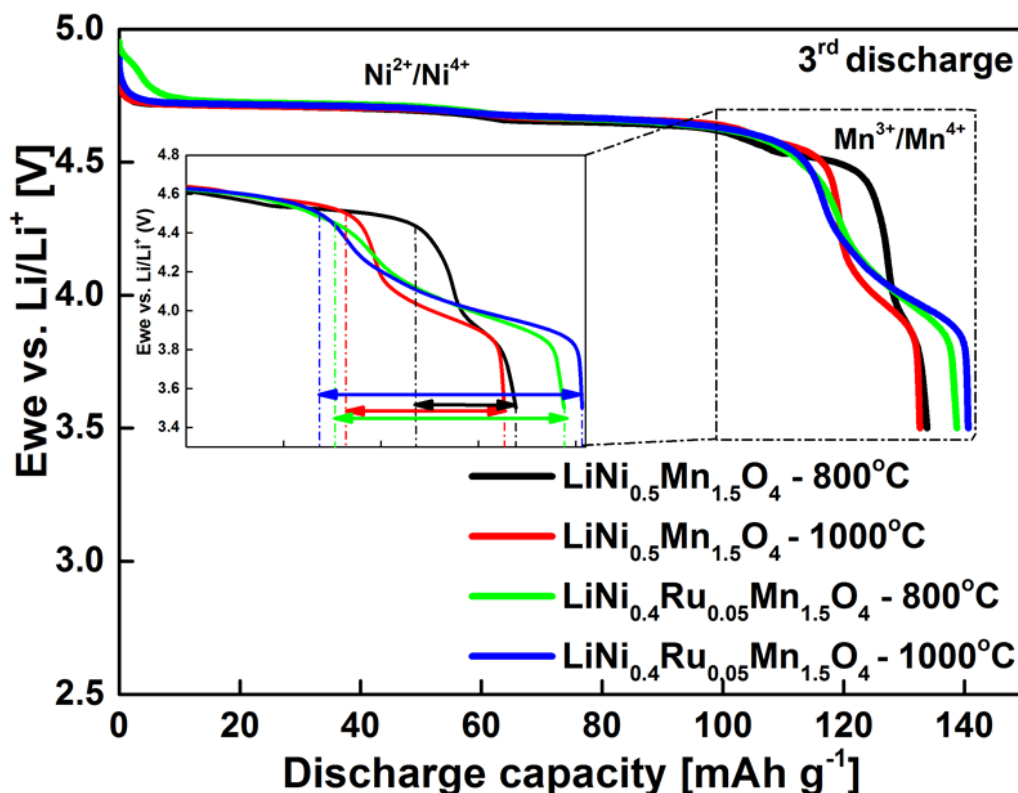
Figure 5.26: Voltage vs. 3rd discharge capacity curves of LNMO-800 °C (black), LNMO-1000 °C (red), LNRMO-800 °C (green) and LNRMO-1000 °C (blue) cathodes cycled at a charge discharge rate of C/2 in a voltage range 3.5-5.0 V.

As the 4 V electrochemical activity directly correlates to the amount of Mn^{3+} in the sample, the above observation points out to a higher Mn^{3+} content in LNRMO (0.173 moles in LNRMO-800 °C and 0.183 moles in LNRMO-1000 °C calculated from the capacity obtained at the 4 V region) in comparison with LNMO (0.1 moles in LNMO-800 °C and 0.109 moles in LNMO-1000 °C calculated from the capacity obtained at the 4 V region). This further indicates that the structure can better tolerate the oxygen non-stoichiometry in the presence of Ru, without undergoing a phase separation. There are no big differences between the electrochemical activities in the 5 V region (4.4-5.0 V) which is attributed to the Ni^{2+}/Ni^{4+} redox couple. Moreover, no additional electrochemically active regions are observed which shows that Ru is not participating in the

electrochemical reactions.

5.2.5.2 Cyclic Voltammetry (CV)

The comparison of the 1st and the 10th CV curves of LNMO-1000 °C and LNRMO-1000 °C spinel samples are shown in Figure 5.27. The electrode mass loadings were ~2 mg. The CV curves of the LNRMO sample show the same behavior as the parent LNMO sample. The improvement of the kinetic is especially pronounced for charge. The larger electrochemical activity during discharging at around 4 V which is attributed to the Mn^{3+}/Mn^{4+} redox couple can clearly be observed from the CV curves.
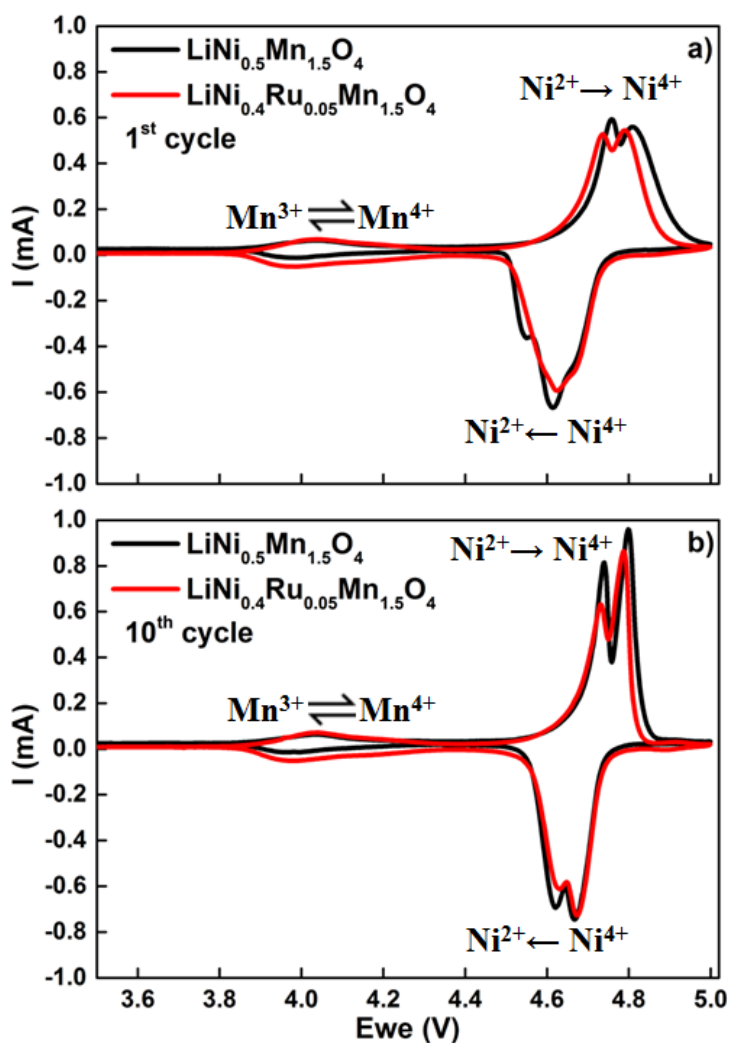
Figure 5.27: Cyclic Voltammograms of a) 1st cycle and b) 10th cycle of LNMO-1000 °C and LNRMO-1000 °C cathodes with the scan rate of 0.1 mV s^{-1} in a voltage range 3.5-5.0 V.

The two peaks in the region of 4.4-5.0 V during oxidation and reduction are related to the Ni^{2+}/Ni^{4+} redox couple [1, 7, 61]. Since the LNRMO-1000 °C sample has less amount of Ni inside the structure, this activity is higher in the LNMO-1000 °C sample (black curve) than in LRMO-1000 °C (red curve), as it was expected. Besides the Mn^{3+}/Mn^{4+} and Ni^{2+}/Ni^{4+} electrochemical activity regions, the CV curves do not have any additional electrochemical activity region which again confirms that Ru^{4+} is not electrochemically active in the studied voltage range.

5.2.5.3 Cycling Stability

The cycling stability results of the first 300 cycles of LNMO and LNRMO synthesized at 800 °C and 1000 °C with a C/2 charge-discharge rate in the voltage window 3.5-5.0 V are shown in Figure 5.28a. For the materials synthesized at 800 °C, the capacity fading is much higher than the materials synthesized at 1000 °C for both samples. The reason might be that the particles of the LNMO-800 °C and LNRMO-800 °C samples are nano-sized and not really well shaped (see Figure 5.3a and 5.20a). Hence, they have a higher surface area which in contact with the electrolyte compared to materials synthesized at 1000 °C. That may cause unwanted side reactions and results in poor cycling performance [63].

Figure 5.28b shows the coulombic efficiencies of all Ru-doped and undoped materials. The LNRMO-1000 °C sample has the highest first cycle coulombic efficiency. Moreover, both Ru-doped materials have higher first cycle coulombic efficiency than the parent LNMO samples. However, the coulombic efficiencies during the following cycles of the materials synthesized at 800 °C are lower than the ones synthesized at 1000 °C. The coulombic efficiencies of both LNMO-1000 °C and LNRMO-1000 °C materials increase and reach $\sim$98-99 % during the following cycles.
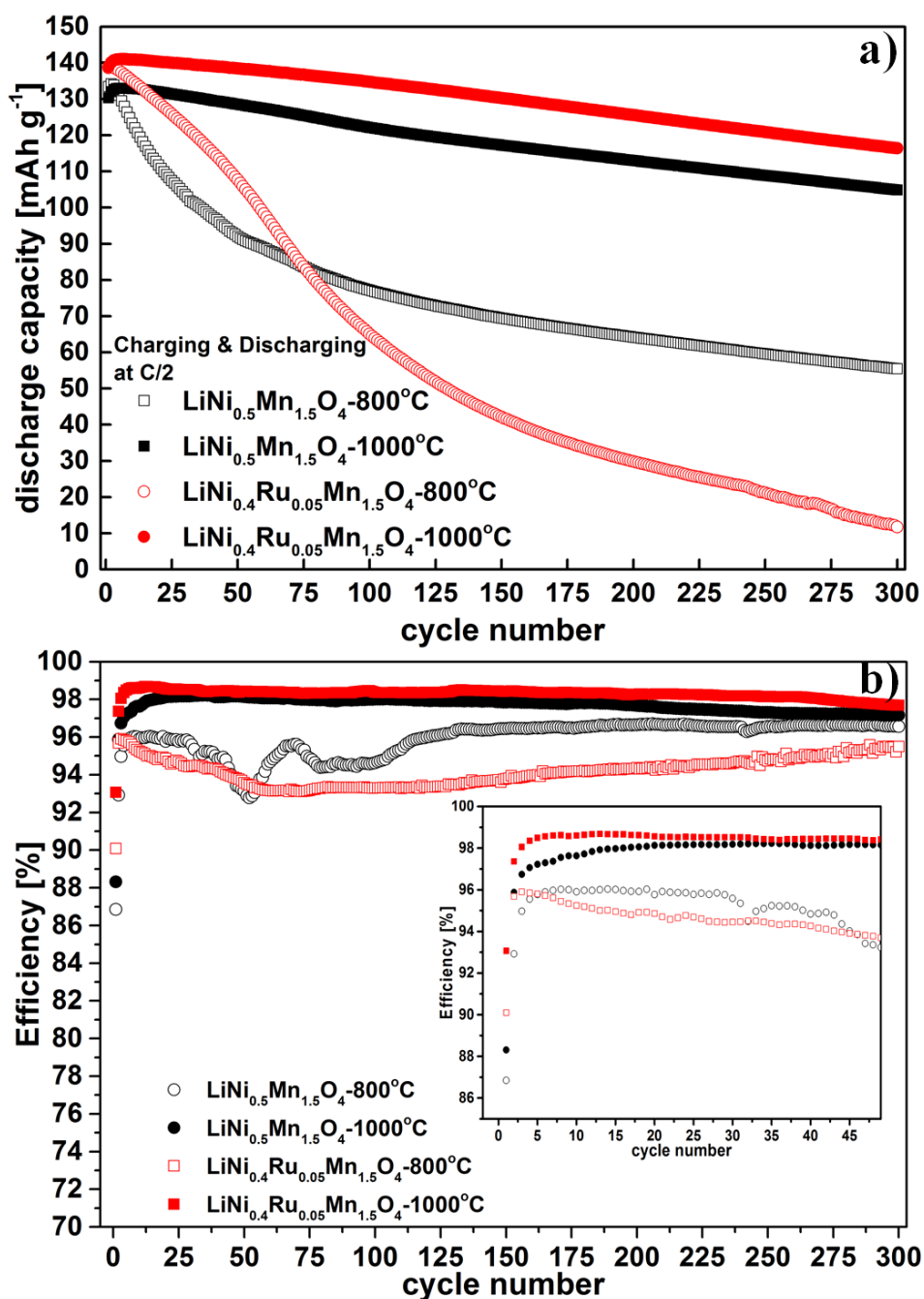
Figure 5.28: a) Discharge capacity vs. cycle number plots of LNMO-800 °C, LNMO-1000 °C, LNRMO-800 °C and LNRMO-1000 °C cathode materials cycled at C/2 rate between 3.5-5.0 V at RT . b) Coulombic efficiencies vs. cycle number plots for the cycling mentioned in a). Inset figure shows the zoom region of coulombic efficiency plots for 50 cycles.
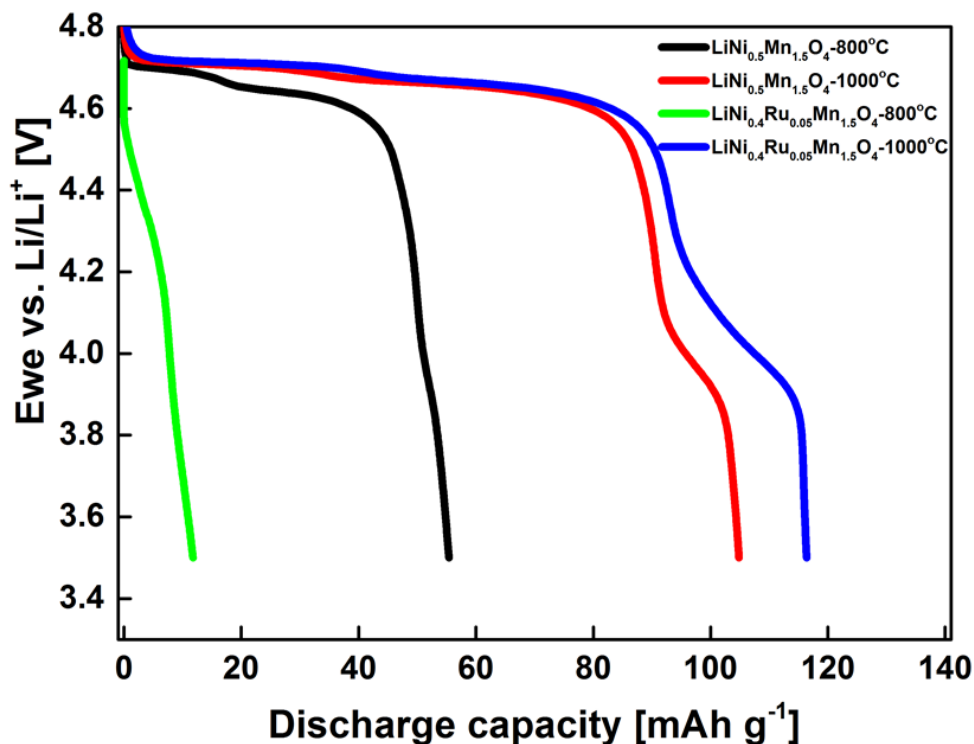
Figure 5.29: Voltage vs. 300th discharge capacity curves of LNMO-800 °C, LNMO-1000 °C, LNRMO-800 °C and LNRMO-1000 °C cathode materials cycled at a charge-discharge rate of C/2 in a voltage range 3.5-5.0 V.

Figure 5.29 shows the 300th discharge curves for all four samples where the high capacity losses of the LNMO-800 °C and LNRMO-800 °C samples are clearly visible and the 4 V plateau almost vanishes for both samples. In addition, the high-voltage plateaus (~4.7 V) diminish for both samples and are almost absent for LNRMO-800 °C. However, it still exists for the materials synthesized at 1000 °C. Even though LNRMO-1000 °C has a larger 4 V electrochemical activity than LNMO-1000 °C, it has a better cycling stability. The capacity retentions after 300 cycles for LNRMO-800 °C and LNRMO-1000 °C are 8.6 % and 84 %, respectively.

5.2.6 Comparison of Morphology Studies of LNMO-1000 °C and LNRMO-1000 °C with SEM after Electrochemical Cycling

In order to get a first insight into the ageing mechanism, LNMO-1000 °C and LNRMO-1000 °C have been investigated with SEM before and after 300 cycles (see Figures 5.30a-d). The 800 °C synthesized samples were omitted as they exhibit poorer electrochemical performance compared to their high-temperature derivative. Figures 5.30a-d show the fresh and the cycled cathodes of LNMO-1000 °C and LNRMO-1000 °C, respectively.
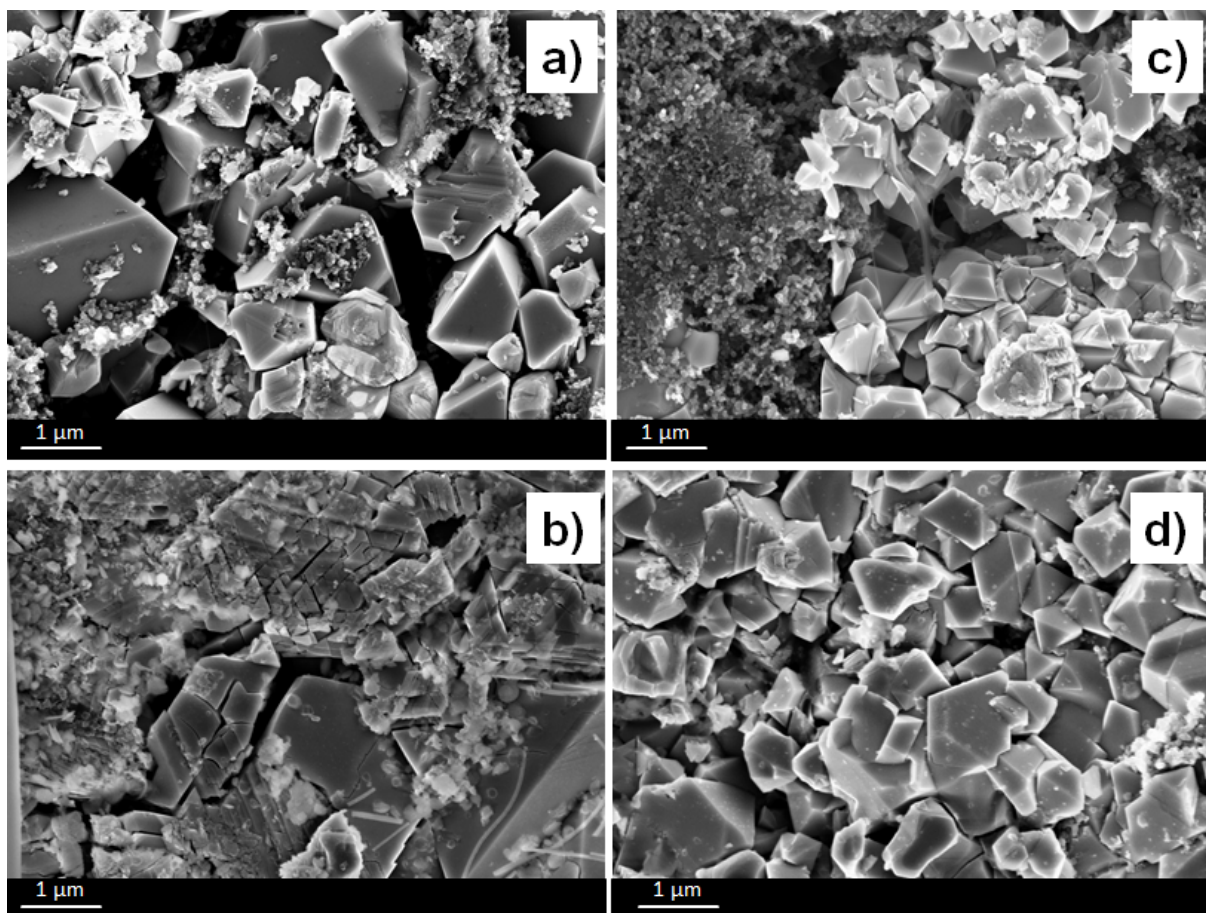
Figure 5.30: SEM images of a) fresh LNMO-1000 °C, b) cycled LNMO-1000 °C, c) fresh LNRMO-1000 °C and d) cycled LNRMO-1000 °C electrodes.

It is interesting to note that the LNMO-1000 °C particles undergo severe crack-

ing after cycling. Comparatively much less particle cracks are observed in the case of LNRMO-1000 °C electrodes. One of the reasons of the observed capacity loss in LNMO-1000 °C might be related to this mechanical degradation which increases the total available surface area and in turn results in side reactions such as electrolyte decomposition. Additionally, this could also lead to contact loss which would result in less material taking part in the electrochemical reaction. This investigation furthermore reveals that ruthenium doping on LNMO also helps to stabilize the electrode morphology to a certain extent.

5.2.6.1 Rate Capability

A comparison of the high-rate performance of LNMO and LNRMO samples synthesized at 800 °C and 1000 °C is displayed in Figure 5.31. The charging rate was hold constant at C/2 and the discharge rates were varied. The samples synthesized at 1000 °C have superior high rate-performance compared to the samples synthesized at 800 °C as it was observed for the parent LNMO sample. However, both Ru-doped samples synthesized at two temperatures have superior high rate performance to their parent materials. The reason for this superior behavior is the improved Li insertion/deinsertion kinetics. It has been confirmed that Ru^{4+} replaces Ni^{2+} in the spinel structure and as a result creates octahedral vacancies [2, 15]. These vacancies may enhance the lithium diffusion, which is taking place from one tetrahedral site to another via the octahedral sites. Among all the materials LNRMO-1000 °C shows the highest absolute capacity even at high C-rates. This material has the largest unit cell volume (see Table 5.5) which might support fast diffusion of lithium ions and results in better kinetics of Li insertion/de-insertion to/from the crystal structure.

The discharge capacities as percentages of the capacity delivered at C/2 of LNMO and LNRMO samples are listed in Table 5.8. The discharge capacity at 5 C of LNRMO-1000 °C is ~100 % of the capacity delivered at C/2. Furthermore, the material delivers

an absolute capacity of $\sim$139 mAh g^{-1} at 10 C which is 100 % of the capacity delivered at C/2. At 20 C an absolute capacity of $\sim$136m Ah g^{-1} (98 %) is obtained.
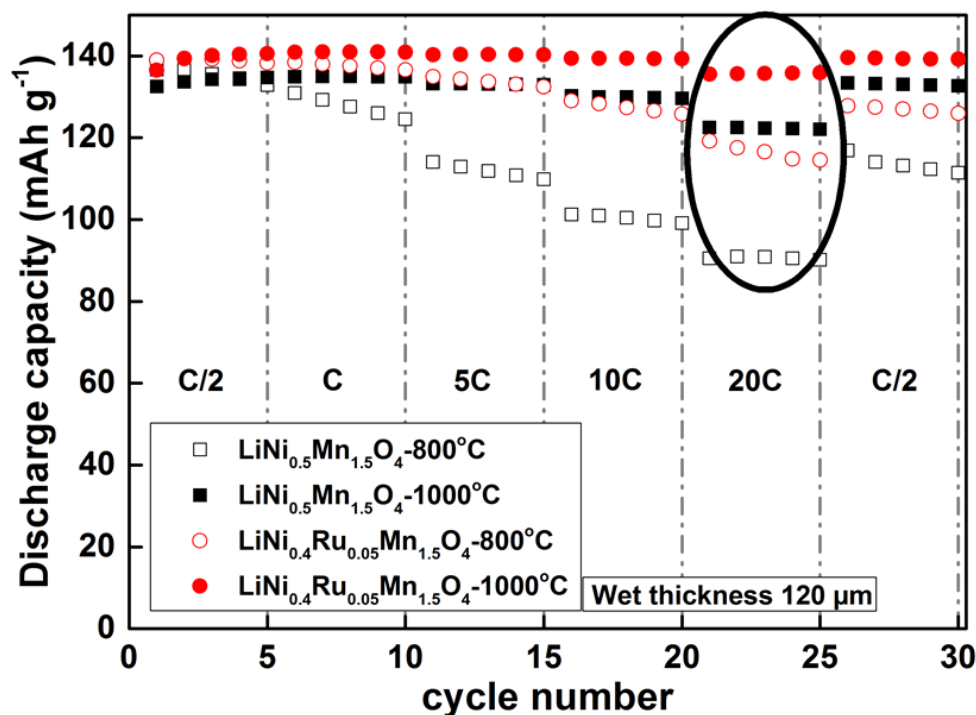
Figure 5.31: Discharge capacity vs. cycle number plots of 800 °C and 1000 °C synthesized LNMO and LNRMO at C/2 charge rate and varied discharge rates for electrodes with a wet thickness of 120 μm.

Sample	Discharge Capacity (mAh g^{-1}) with C/2	The discharge capacity as percentage of the capacity delivered at C/2			
		1C	5C	10C	20C
LNMO-800 °C	136	95%	83%	74%	67%
LNMO-1000 °C	134	100%	99%	97%	91%
LNRMO-800 °C	139	99%	96%	92%	84%
LNRMO-1000 °C	139	100%	100%	100%	98%

Table 5.8: The discharge capacities obtained at different C-rates for LNMO and LNRMO cathode materials.

5.2.7 Electrochemical Performances of $LiNi_{0.4}Ru_{0.05}Mn_{1.5}O_4$-1000 °C in Comparison with $LiNi_{0.5}Mn_{1.5}O_4$-1000 °C Cathode at Elevated Temperature (55 °C)

5.2.7.1 Cycling Stability

The cycling stability at 55 °C for both LNMO-1000 °C and LNRMO-1000 °C samples is shown in Figure 5.32. The LNRMO-1000 °C cathode material showed a higher initial capacity than LNMO-1000 °C similar to the performance obtained at RT. However, they both have similar behavior when they were cycled at 55 °C. The most pronounced degradation in LNRMO-1000 °C starts earlier than LNMO-1000 °C. Considering the cycling conditions like high voltage range, elevated temperature environment and high cycling rate, the reason for the faster degradation in LNRMO-1000 °C might be the performance of the cell which was used for days.
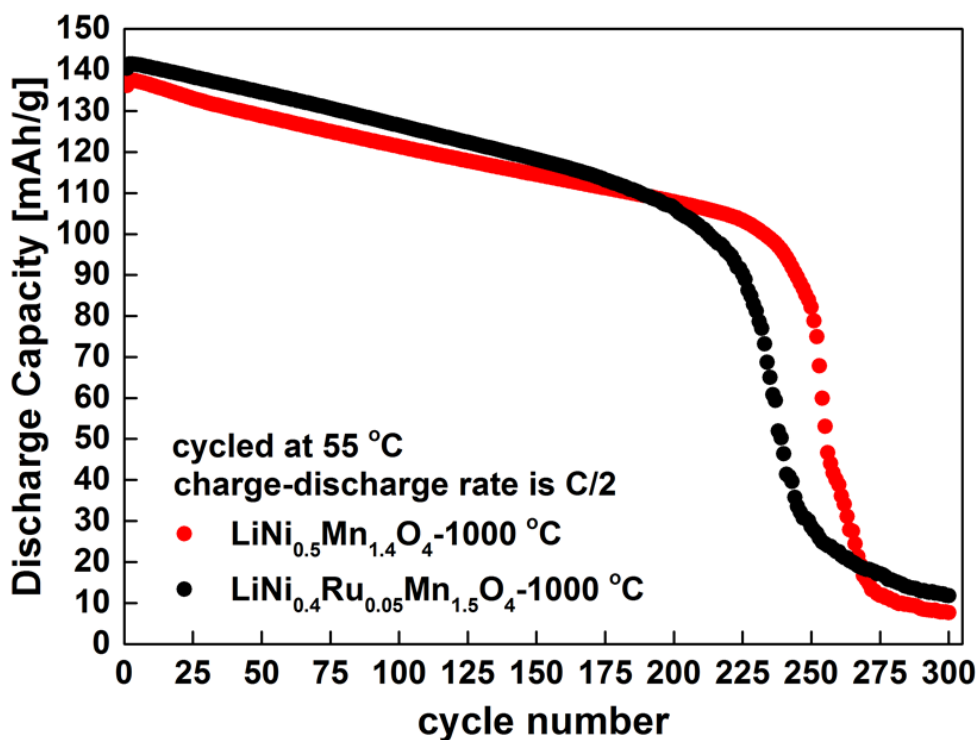
Figure 5.32: Cycle number vs. discharge capacity plots of LNMO-1000 °C and LNRMO-1000 °C cathode materials cycled at C/2 charge-discharge rate in a voltage range 3.5-5.0 V at 55 °C.

In addition, in section 5.2.5.1, where the voltage profiles of LNMO-1000 °C and LNRMO-1000 °C samples were compared, it was observed that the LNRMO-1000 °C sample contains a higher amount of Mn^{3+} (0.183 moles) than LNMO-1000 °C (0.109 moles). Since Mn dissolves in the acidic species containing electrolyte when it has its trivalent state [5, 66, 67], the reason for the faster capacity fading of LNRMO-1000 °C might also be that it has a higher amount of Mn^{3+} inside the structure. Moreover, elevated temperature environment for cycling might accelerate the Mn dissolution process in the electrolyte inside the test cells.

5.2.8 Investigations on Structural Evolutions of $LiNi_{0.4}Ru_{0.05}Mn_{1.5}O_4$-1000 °C Cathode Material during Electrochemical Cycling using Synchrotron Diffraction

5.2.8.1 Analysis of Synchrotron Diffraction Patterns Obtained During 1st Charging and Discharging at C/2 Current Rate

In order to investigate the structural evolution during cycling, synchrotron diffraction patterns were obtained when the LNRMO-1000 °C cathode was cycled with a charge/discharge rate of C/2 in the applied voltage range 3.5-5.0 V. According to the electrochemical performance of *in situ* cell, a re-intercalation of ∼0.95 moles of lithium into LNRMO-1000 °C was obtained which is the same as that observed with Swagelok®-type cell.

The structural evolution during charge and discharge is displayed in Figure 5.33 with selected 2θ regions, where black and red lines correspond to the charge and discharge regions, respectively.
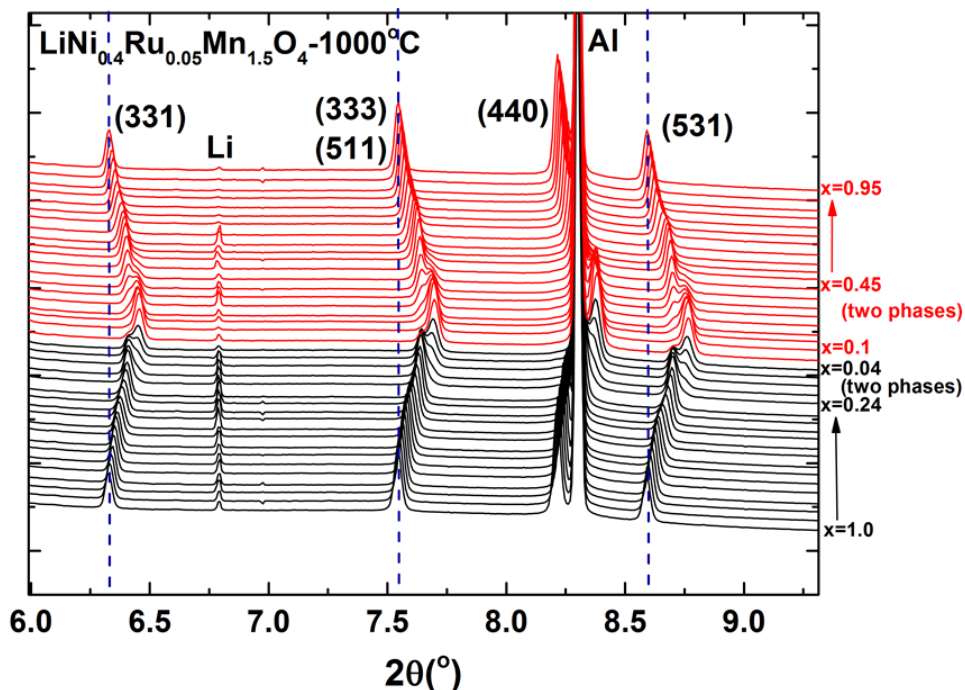
Figure 5.33: Selected 2θ regions of the *in situ* synchrotron diffraction patterns of LNRMO-1000 °C cathode material.

An additional cubic spinel phase appears in LNRMO-1000 °C with the same space group ($Fd\bar{3}m$) as the initial phase and different lattice parameter similar to the case of LNMO-1000 °C. The additional phase starts to appear between x = 0.24 - 0.04 moles during charging and between x = 0.1 - 0.45 moles of lithium in the structure during discharging (where "x" is defined as the nominal number of moles of Li that remains in the structure, calculated from the number of electrons flowing through the circuit). The change in lattice parameters during cycling is shown in Figure 5.34a.
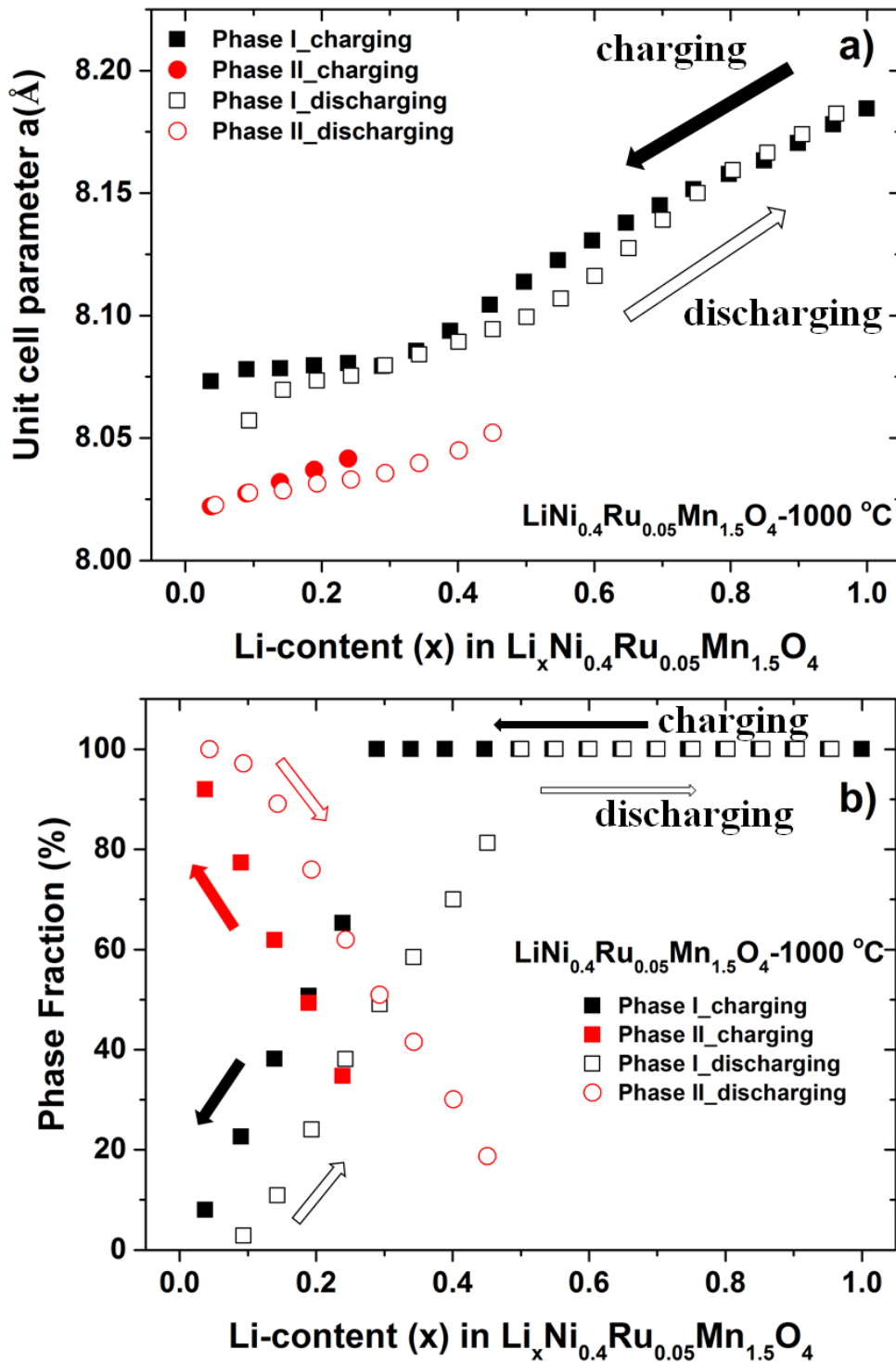
Figure 5.34: a) Change in the unit cell parameter as a function of number of moles of Li (x) remaininig in the structure for $Li_xNi_{0.4}Ru_{0.05}Mn_{1.5}O_4$-1000 °C b) The phase ratios vs. Li content in the sample during cycling.

The obtained lattice parameters for the two cubic spinel phases in LNRMO-1000

°C are closer to each other than in LNMO-1000 °C (see Figure 5.34a). The less change in the lattice parameters during cycling for LNRMO-1000 °C may help to preserve the morphology of the electrode during cycling (see Figure 5.30).

The unit cell parameters of the second cubic spinel phase undergo a constant decrease and increase during charging and discharging, similar to the main cubic spinel phase, which proves that the new phase formed is also electrochemically active, like in the parent LNMO cathode. Additionally, the second phase disappears at the end of discharging process which means that the formation of this second phase is reversible which in turn is supported by the phase fraction analysis shown in Figure 5.34b.

The micro-strain analysis obtained by Rietveld refinement of LNRMO-1000 °C is shown in Figure 5.35.
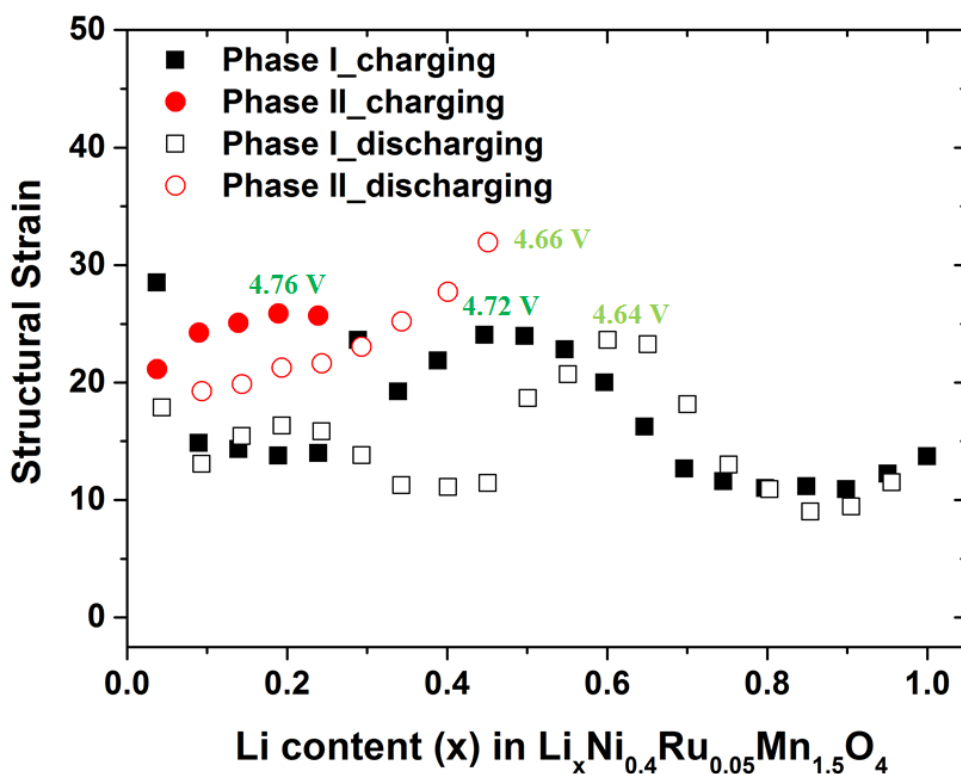
Figure 5.35: The micro-strain analysis of $LiNi_{0.4}Ru_{0.05}Mn_{1.5}O_4$-1000 °C cathode material. The maximum strain is given in the Fullprof microstructural output file as $\frac{\Delta d}{d} \times 10^{-4}$.

Even though some increase in the lattice strain was observed at the voltage points where the Ni^{2+}/Ni^{4+} redox couple is active as it was observed in parent LNMO-1000 °C, lattice strain during lithium insertion/deinsertion is more stable compared to undoped LNMO-1000 °C. In another word, the change in the lattice strain of LNRMO-1000 °C during cycling is less than LNMO-1000 °C (see Figure 5.14). That makes the structure more relaxed which might enhanced the cycling performance of the sample.

5.3   Fe doped $LiNi_{0.5-x}Fe_{2x}Mn_{1.5-x}O_4$-1000 °C (x=0.1; 0.15; 0.2) Spinels as High-Volt Cathode Materials

The influence of Fe-doping on the performance of LNMO will be focused in this section. According to the literature , Fe substitution could improve the thermal stability of the spinel system [39]. In addition, the partial substitution of Mn or Ni metals in $LiNi_{0.5}Mn_{1.5}O_4$ with Fe has been studied mostly and the results shows that Fe substitution improves the cycling performance and rate capability. Only couple of work has been submitted about the effect of Fe substitution with both Ni and Mn [22, 25]. However, especially the effects of Fe substitution on structure (formation of bimixture), thermal stability or electrochemical mechanism was not studied. The new composition $LiNi_{0.5-x}Fe_{2x}Mn_{1.5-x}O_4$-1000 °C with x=0.1; 0.15; 0.2 will be investigated in detail on the structure, morphology, electrochemical performance, cycling mechanism etc.

5.3.1   Structural Analyses

The synchrotron diffraction patterns of $LiNi_{0.4}Fe_{0.2}Mn_{1.4}O_4$ ($LNF_{0.2}MO$), $LiNi_{0.35}Fe_{0.3}Mn_{1.35}O_4$ ($LNF_{0.3}MO$) and $LiNi_{0.3}Fe_{0.4}Mn_{1.3}O_4$ ($LNF_{0.4}MO$) samples synthesized at 1000 °C are presented in Figure 5.36. The Fe-doped samples also have cubic spinel structure with space group $Fd\bar{3}m$ but they do not contain any rock-salt impurity phase as in the parent LNMO. According to the Rietveld refinement based

on the synchrotron diffraction data, only $LNF_{0.2}MO$ powder is phase pure without any other impurity phases. The Rietveld refinement results are listed in Table 5.9. When the amount of Fe increases in $LiNi_{0.5-x}Fe_{2x}Mn_{1.5-x}O_4$, the lattice parameters increase and two additional phases, Fe containing cubic spinel Fe_3O_4 (space group $Fd\bar{3}m$) and a monoclinic Li_2MnO_3 phase with $C2/m$ space group, appear. The phase fractions of the Fe_3O_4 and the Li_2MnO_3 phases are also directly proportional to the amount of Fe inside the whole nominal composition.
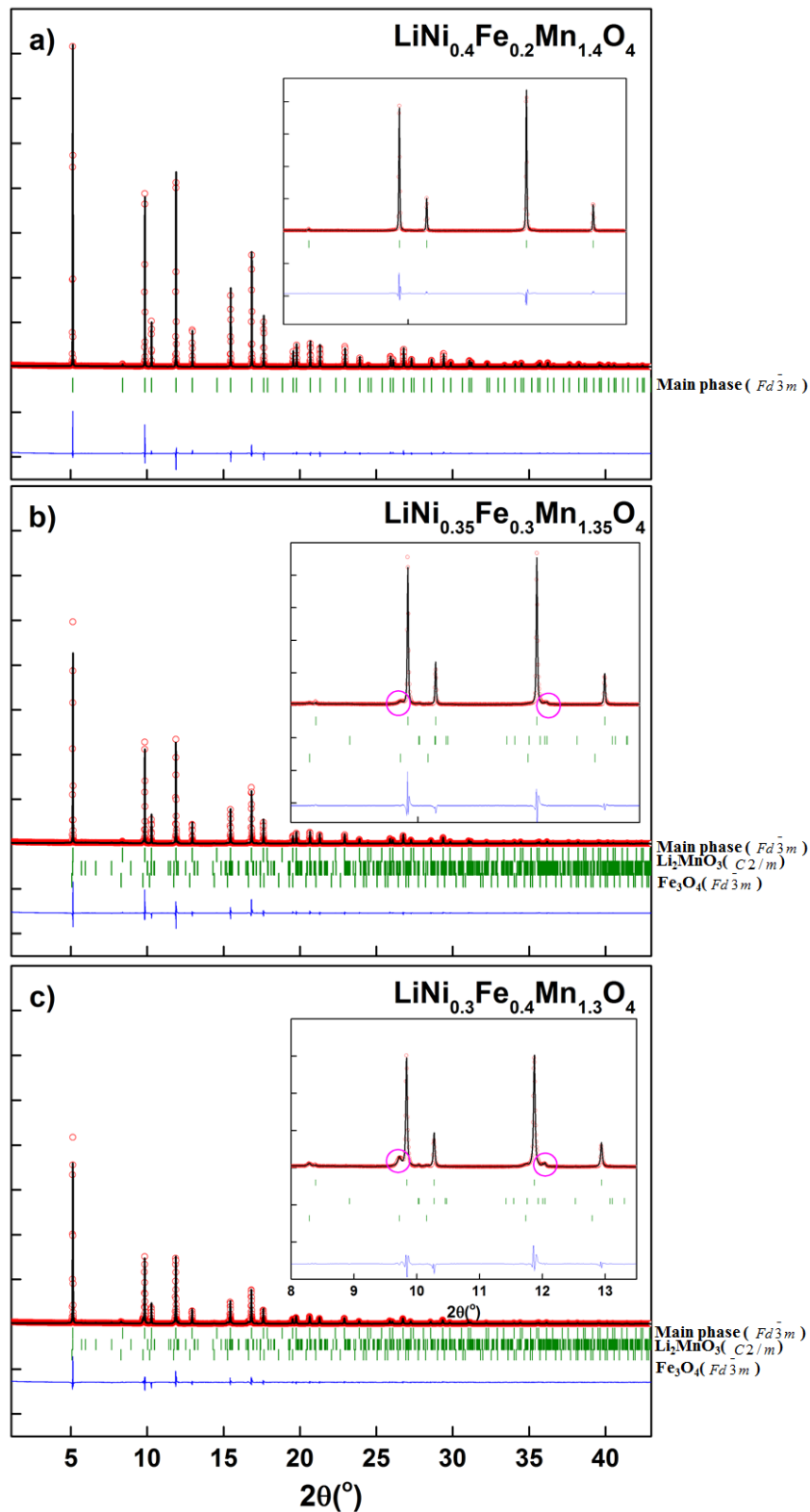
Figure 5.36: Rietveld refinement results based on synchrotron diffraction patterns of as prepared a) $LNF_{0.2}MO$ b) $LNF_{0.3}MO$ and c) $LNF_{0.4}MO$ materials measured in 0.5 mm capillaries. The inset figures indicate zoomed regions where the contributions from the Fe_3O_4 and Li_2MnO_3 phases can be seen (pink circles) in $LNF_{0.3}MO$ and $LNF_{0.4}MO$ samples but not in $LNF_{0.2}MO$.

Samples	Atom Site	x=y=z	a(Å)	Volume (Å^3)	Fraction of impurity phases % (Fe$_3$O$_4$/Li$_2$MnO$_3$)	Overall Temperature Factor (B$_o$v)	R$_{wp}$(%)
LNF$_{0.2}$MO	Li$_{8a}$ Ni$_{16d}$ Mn$_{16d}$ Fe$_{16d}$ O$_{32e}$	0.125 0.500 0.500 0.500 0.2649(3)	8.1949(1)	550.35(1)	-	0.25	11.1
LNF$_{0.3}$MO	Li$_{8a}$ Ni$_{16d}$ Mn$_{16d}$ Fe$_{16d}$ O$_{32e}$	0.125 0.500 0.500 0.500 0.2626(5)	8.2071(1)	552.80(1)	∼3.5/∼3.5	0.22	14.6
LNF$_{0.4}$MO	Li$_{8a}$ Ni$_{16d}$ Mn$_{16d}$ Fe$_{16d}$ O$_{32e}$	0.125 0.500 0.500 0.500 0.2629(5)	8.2129(1)	554.00(2)	∼8.5/∼4	0.25	13.5

Table 5.9: Rietveld refinement results of Fe-doped samples based on synchrotron diffraction data (space group $Fd\bar{3}m$).

Rietveld refinements based on neutron diffraction data of all Fe-doped LNMO samples are shown in Figure 5.37. According to these results, all three Fe-doped samples contain Fe$_3$O$_4$ ($Fd\bar{3}m$) and Li$_2$MnO$_3$ ($C2/m$) phases. The impurity phases were not detectable with synchrotron diffraction experiments for the LNF$_{0.2}$O sample. However, the phase ratios of these impurity phases are very small (0.89 % for spinel Fe$_3$O$_4$ and 1.32 % for Li$_2$MnO$_3$, respectively). Neutron analysis shows that increasing the amount of Fe in the nominal composition LiNi$_{0.5-x}$Fe$_{2x}$Mn$_{1.5-x}$O$_4$ leads to an increased amount of Li$_2$MnO$_3$ and Fe$_3$O$_4$ impurity phases.
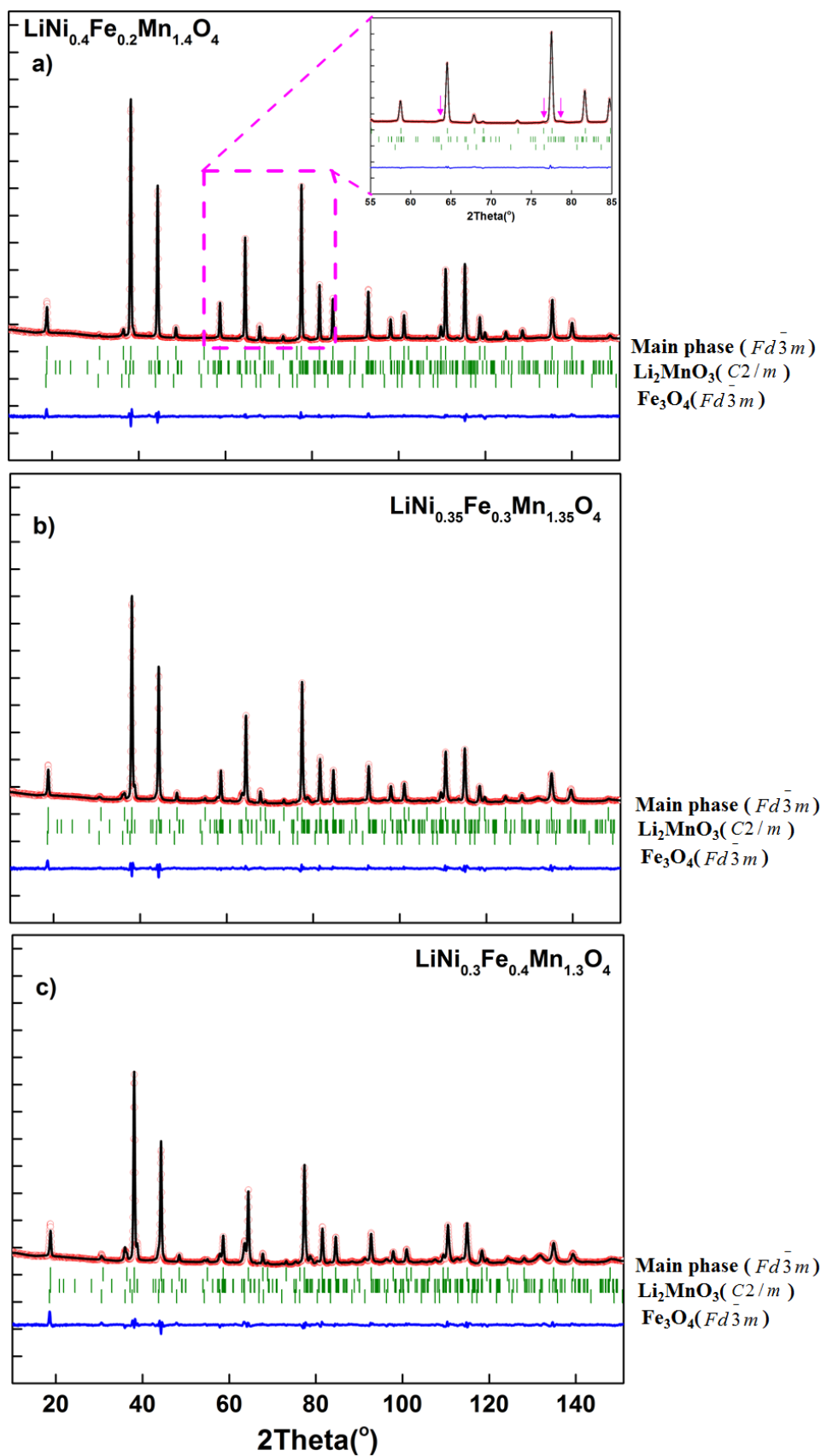
Figure 5.37: Rietveld refinement results based on neutron diffraction patterns of as prepared a) $LNF_{0.2}MO$ b) $LNF_{0.3}MO$ and c) $LNF_{0.4}MO$ powders.

The calculated stoichiometry from the obtained site occupation factors after the Rietveld refinements based on the neutron data are $Li_{0.82176}Ni_{0.38832}Fe_{0.15552}Mn_{1.45632}O_4$, $Li_{0.87888}Ni_{0.36024}Fe_{0.20736}Mn_{1.43088}O_4$ and $Li_{0.93048}Ni_{0.26064}Fe_{0.30816}Mn_{1.43352}O_4$ for $LNF_{0.2}MO$, $LNF_{0.3}MO$ and $LNF_{0.4}MO$, respectively. It can be observed that there is a slight Mn excess in all compositions. This can be correlated with the Fe deficiency in the main spinel phase ($Fd\overline{3}m$), $LNFe_{0.2}MO$, $LNF_{0.3}MO$ and $LNF_{0.4}MO$ which is further confirmed by the presence of the impurity spinel phase Fe_3O_4. Moreover, the neutron scattering lengths of Ni and Fe are very similar (10.3 fm and 9.45 fm, respectively) which could also contribute to the discrepancy of the calculated values with the nominal compositions.

5.3.2 Morphology Studies of initial $LiNi_{0.5-x}Fe_{2x}Mn_{1.5-x}O_4$ (x= 0.1; 0.15; 0.2) powders

The particles of Fe-doped LNMO samples exhibit also pseudo-octahedral shape and $LNFe_{0.2}MO$ possesses smooth surfaces like the parent LNMO material (see Figure 5.38). However, the defined edges and smooth surfaces deteriorate with increasing amount of Fe in the sample. The layered lines on the particles which can clearly be seen in $LNF_{0.3}MO$ and $LNF_{0.4}MO$ samples might be related to the Li_2MnO_3 bimixture grown in the same grain as the main phase [69].

The particle size is slightly larger and the size distribution is narrower for all Fe-doped LNMO samples compared to the undoped one which results in lower surface area available for parasitic reactions. This observation was then confirmed by the Brunauer-Emmett-Teller (BET) experiments. According to the surface area analysis, the LNMO sample has the highest surface area and the surface area found by BET decreases by increasing the amount of Fe inside the structure. The BET surface areas were found to be 13.40 m^2/g, 11.16 m^2/g, 4.87 m^2/g and 4.76 m^2/g for the LNMO, $LNF_{0.2}MO$, $LNF_{0.3}MO$ and $LNF_{0.4}MO$ materials, respectively.
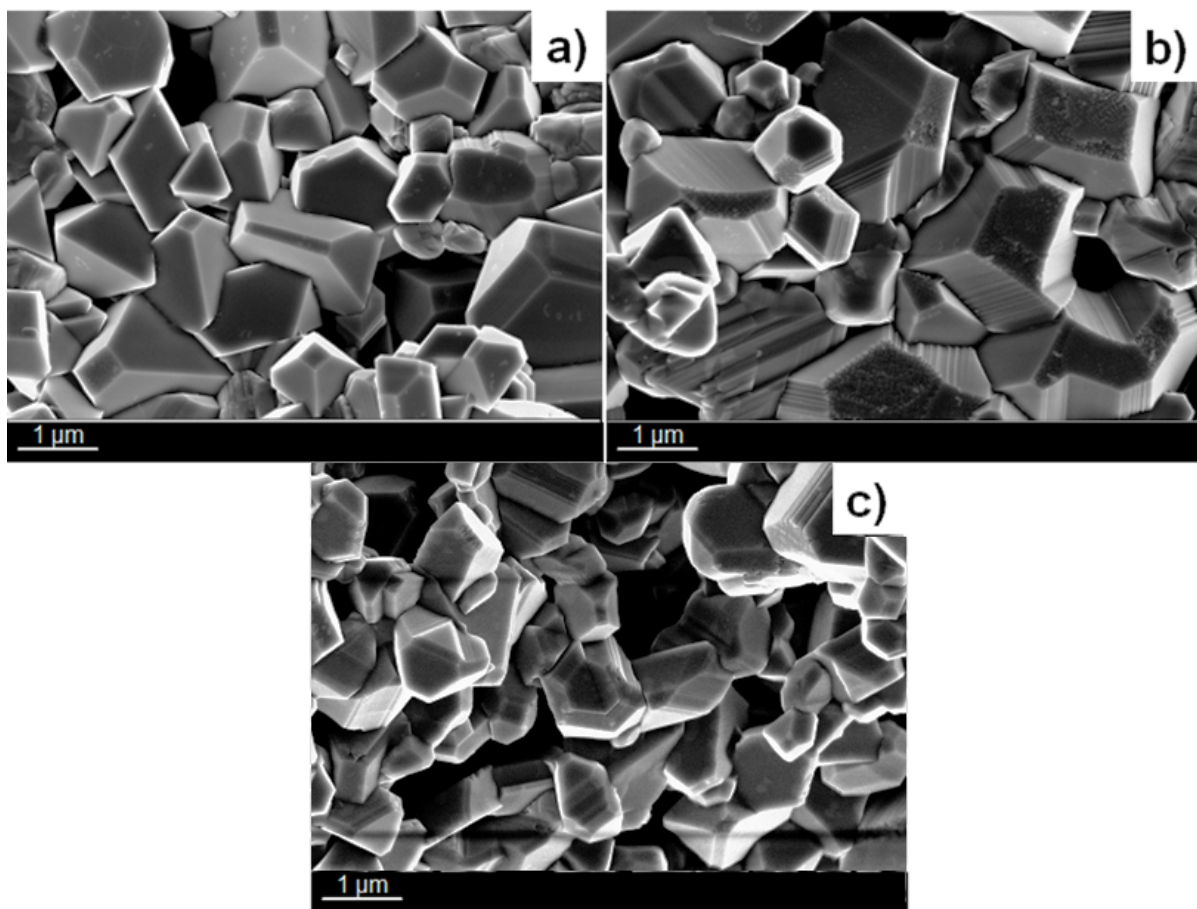
Figure 5.38: SEM images of as prepared a) $LNFe_{0.2}MO$ b) $LNFe_{0.3}MO$ and c) $LNFe_{0.4}MO$ powders.

5.3.3 Mössbauer Spectroscopic Studies

The Fe Mössbauer spectra of $LNF_{0.2}MO$, $LNF_{0.3}MO$ and $LNF_{0.4}MO$ are shown in Figure 5.39.

For the sample with $LNF_{0.2}MO$, the spectrum can be well described with a single doublet with isomer shift IS = 0.34 mm/s and quadrupole splitting QS = 0.78 mm/s (Table 5.10). These parameters confirm that exclusively Fe^{3+} with high-spin configuration in an octahedral coordination is present [50, 70–73]. The spectra of the samples with $LNF_{0.3}MO$ and $LNF_{0.4}MO$ are also dominated by this doublet and IS, QS, and the line width are very similar to those of the sample with $LNF_{0.2}MO$ (Table 5.1). Additionally, a sextet is present with IS = 0.24 mm/s and a hyperfine field B_{hf} of about 48 T.

Its relative area fraction amounts to 28 and 36 % for x = 0.3 and 0.4, respectively. These values are consistent with the presence of Fe_3O_4 phase [74]. This sextet is not visible for $LNF_{0.2}MO$ but might be obscured by the noise level.
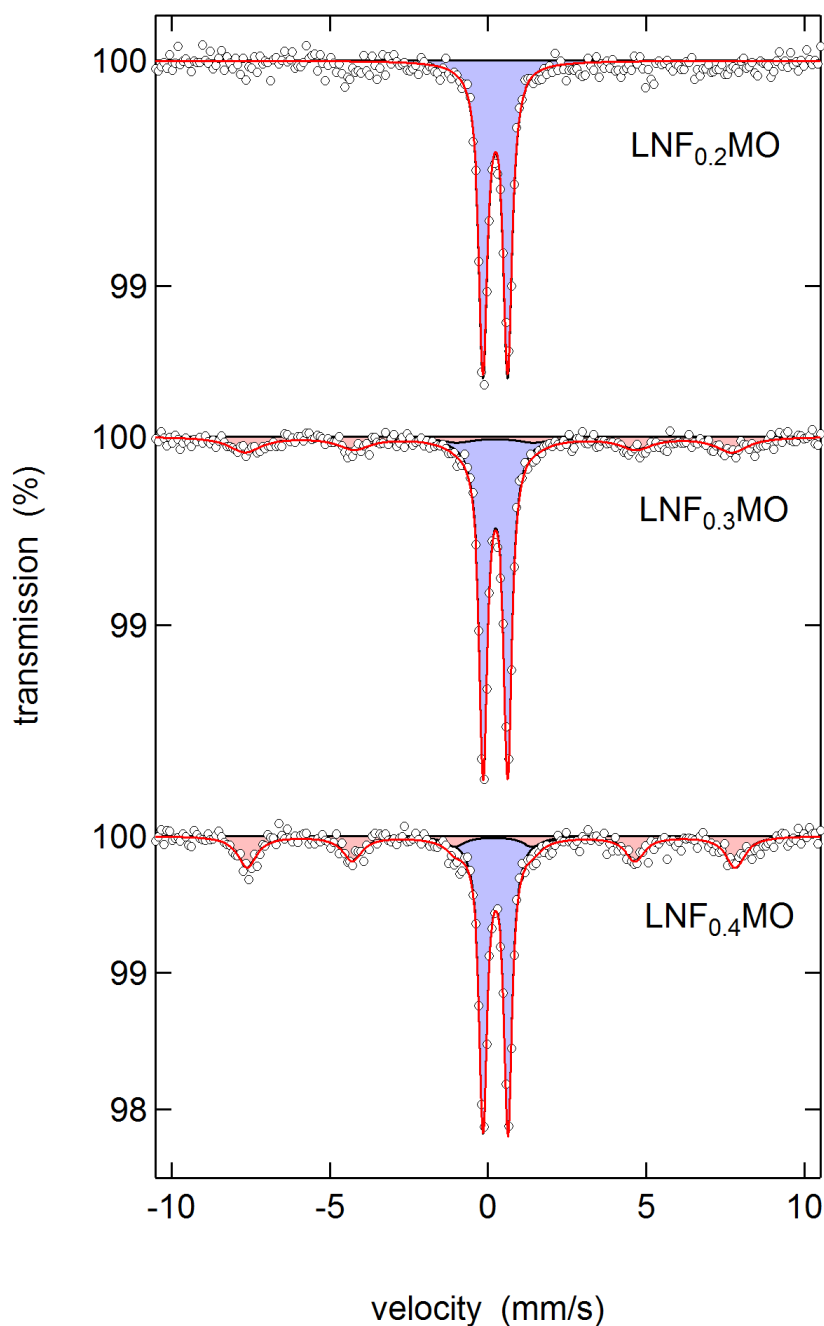
Figure 5.39: ^{57}Fe Mössbauer spectra of $LNF_{0.2}MO$, $LNF_{0.3}MO$ and $LNF_{0.4}MO$ samples at room temperature. (Experimental data points are shown as white spheres and the fits are shown as red lines. Subspectra are shown as blue doublets and red sextets).

Sample	Charge State	IS	QS	Line Width	B_{hf}	Area Fraction
LNF$_{0.2}$O	Fe^{3+}	0.335±0.002	0.781±0.004	0.328±0.005	-	100 %
LNF$_{0.3}$O	Fe^{3+}	0.339±0.001	0.775±0.002	0.309±0.003	-	71.9 %
	Fe^{3+}	0.235±0.044	-0.226±0.085	1.245±0.166	47.6±0.3	28.1 %
LNF$_{0.4}$O	Fe^{3+}	0.342±0.002	0.788±0.003	0.229±0.004	-	63.8 %
	Fe^{3+}	0.249±0.018	-0.075±0.036	0.740±0.065	47.8±0.1	36.2 %

Table 5.10: Fit parameters of the Mössbauer subspectra shown in Figure 5.39. Isomer shift IS, quadrupole splitting QS, and line width are given in mm/s. The hyperfine field B_{hf} is given in T.

5.3.4 Nuclear Magnetic Resonance (NMR) Spectroscopic Studies of LNF$_{0.2}$MO Cathode Material in comparison with the parent LNMO-1000 °C

Figure 5.40 shows ^{7}Li MAS NMR spectra of the LNMO-1000 °C and LNF$_{0.2}$MO samples. Both spectra exhibit large NMR shifts of the isotropic peaks and MAS spinning sideband manifolds with similar width.

In the LNMO-1000 °C several resonances are discernible in the range between 600 ppm and 1200 ppm. The line shape is very similar to the spectra obtained by Cabana *et al.* from samples synthesized at 700 °C and 800 °C [75]. Deconvolution of our spectrum requires at least six contributing resonances with shift values of 725, 829, 893, 959, 1031, and 1113 ppm. This result is consistent with the findings by Cabana *et al* [75]. The multiple NMR resonances found in their sample synthesized at 700 °C were explained by two models of the local Mn/Ni distribution based on different degrees of Mn/Ni disorder.
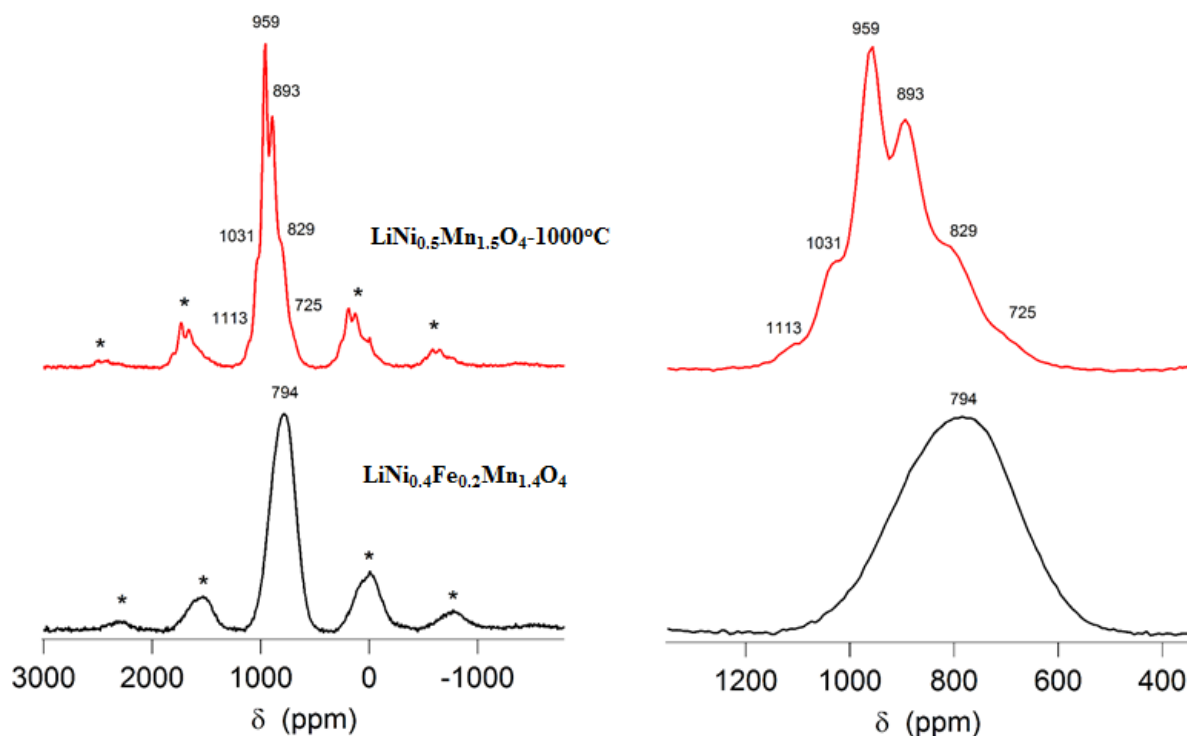
Figure 5.40: ^{7}Li MAS NMR spectra of LNMO-1000 °C and LNF$_{0.2}$MO. The isotropic
resonances are labelled with the corresponding shifts. The spinning sidebands
are marked with asterisks.

In the spectrum of LNF$_{0.2}$MO, one broad peak is observable in the range between
500 ppm and 1100 ppm without any indication of several distinct resonances. A sat-
isfactory fit was achieved by using a single Gaussian function yielding an NMR shift
of 794 ppm. The reduction of the average ^{7}Li NMR shift in the Fe-substituted sample
by about 100 ppm is caused by the substitution of Ni^{2+} and Mn^{4+} by Fe^{3+} in the first
cation coordination sphere around Li. This substitution also leads to a large variety of
local electronic configurations. Therefore, possibly assisted by additional local distor-
tions of the Mn/Ni/Fe-O-Li bonds, superposition of the different contributions might
result in the observed broad featureless peak. In summary NMR spectroscopy confirm

that the Fe ions are incorporated into the spinel lattice of LNMO-1000 °C.

5.3.5 Electrochemical Performances of LiNi$_{0.5-x}$Fe$_{2x}$Mn$_{1.5-x}$O$_4$ (x= 0.1; 0.15; 0.2) Cathode Materials at Room Temperature (RT)

5.3.5.1 Voltage Profile Comparison of Fe-doped and undoped LNMO-1000 °C Cathode Material

Figure 5.41 shows the voltage profile of the 3rd discharge of the Fe substituted samples compared with the undoped one.

The observation shows that the discharge plateau in the 4 V region where the Mn^{3+}/Mn^{4+} redox couple exists is bigger for Fe-doped samples than LNMO-1000 °C. Additionally, this 4 V electrochemical activity becomes more pronounced when the Fe amount increases in the material which shows that the amount of Mn^{3+} is getting higher in the spinel structure. The calculated amount of Mn^{3+} from the experimental data (voltage profiles) are 0.139 moles, 0.158 moles and 0.184 moles for LNF$_{0.2}$MO, LNF$_{0.3}$MO and LNF$_{0.4}$MO, respectively.
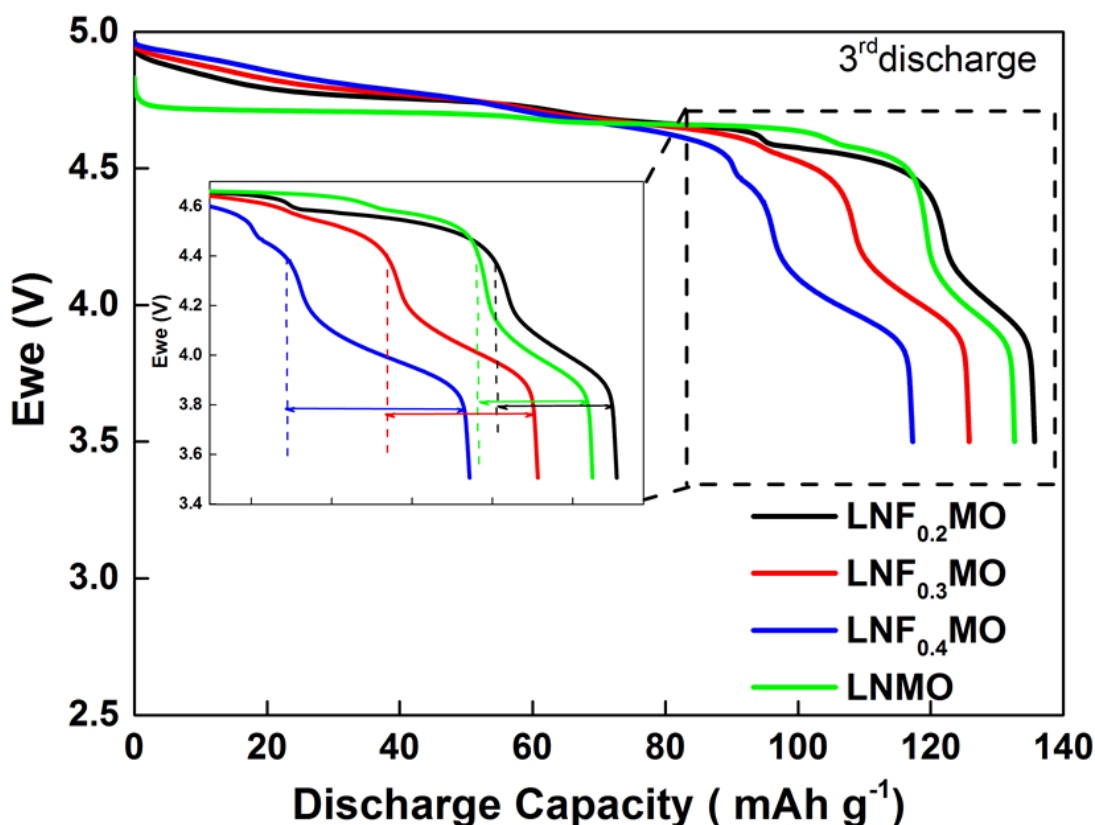
Figure 5.41: Voltage vs. 3rd discharge capacity curves of $LNF_{0.2}MO$, $LNF_{0.3}MO$ and $LNF_{0.4}MO$ cathode materials in comparison with the parent LNMO-1000 °C cycled at a charge/discharge rate of C/2 in a voltage range 3.5-5.0 V. Inset figure shows the 4 V region.

5.3.5.2   Cyclic Voltammetry (CV)

It has been reported earlier that there is an electrochemical reaction of $Fe^{3+} \rightleftharpoons Fe^{4+} + e^-$ at around 5.0 V in the Fe-containing spinel [1, 70, 76]. In order to investigate this effect, the voltage range for Fe-doped samples was increased to 3.5-5.3 V for CV experiments (see Figure 5.42).
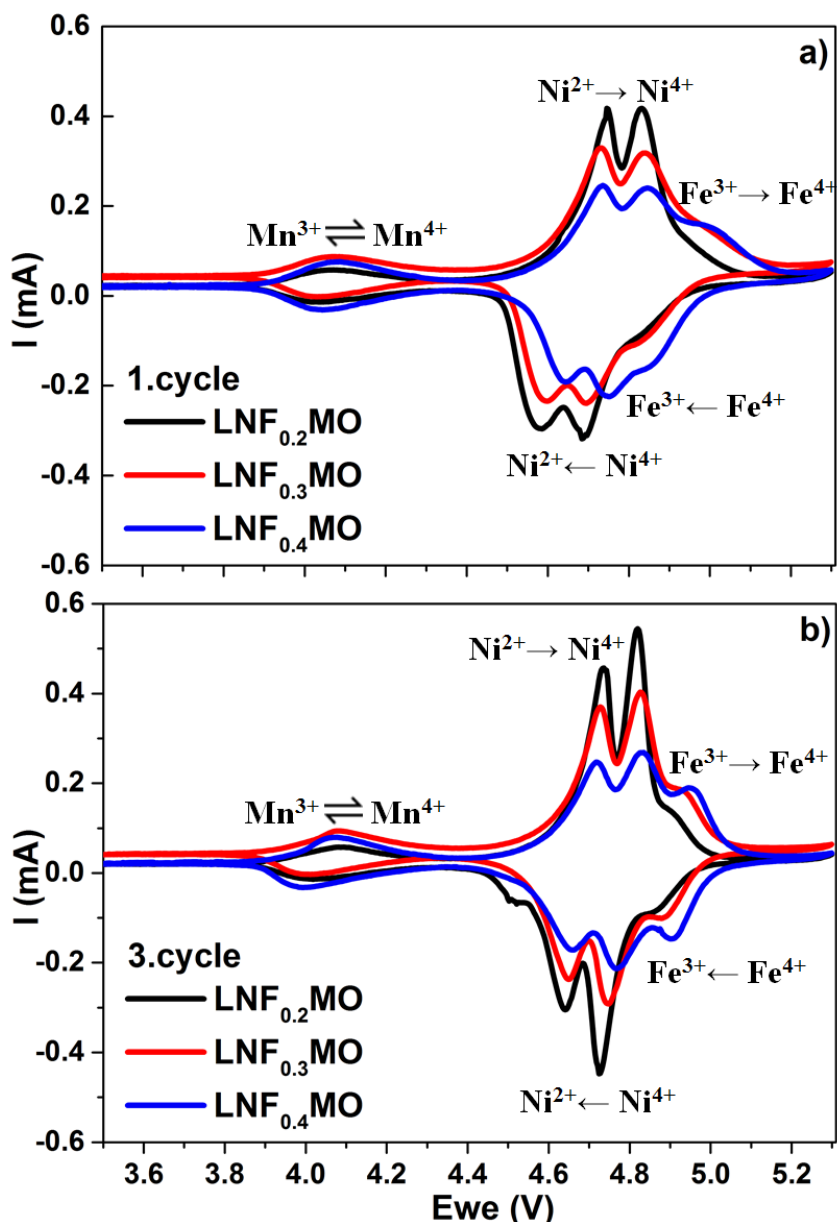
Figure 5.42: Cyclic Voltammograms of a) 1st cycle and b) 3rd cycle of $LNF_{0.2}MO$, $LNF_{0.3}MO$ and $LNF_{0.4}MO$ cathode materials with a scan rate of 0.1 mV s^{-1} in a voltage range 3.5-5.3 V.

In the CV curves of Fe containing materials, besides Mn^{3+}/Mn^{4+} (at round 4 V) and Ni^{2+}/Ni^{4+} (at around 4.7 V), there is an additional peak at around $\sim$5.0 V in the oxidation step which is reversible and observed at $\sim$4.9 V in the reduction step in the first cycle. This could be assigned to the Fe^{3+}/Fe^{4+} redox couple [1]. In the 3rd cycle, the peak separation decreases which is the indication of better kinetic for both oxidation and reduction steps. The Mn^{3+}/Mn^{4+} electrochemical activity is getting larger

when the amount of Fe increases in the structure, similar to the observation from the voltage profiles. Since the amount of Ni is decreasing and the amount of Fe is increasing for the $LNF_{0.2}MO$, $LNF_{0.3}MO$ and $LNF_{0.4}MO$ cathode materials the corresponding electrochemical activities are changing accordingly. As a result, the Ni^{2+}/Ni^{4+} electrochemical activity decreases and the Fe^{3+}/Fe^{4+} electrochemical activity increases with increasing amount of Fe doping into the LNMO, which can be seen more clearly in Figure 5.42b.

There could also be a contribution to the electrochemical activity from Li_2MnO_3 in the first charge at ~4.7 V and in the following discharge at ~3.5 V and charge eventhough the whole electrochemical activity cannot be reached [69]. However, this contribution cannot be seen clearly from the CV curves or voltage profiles due to the small amount of Li_2MnO_3 impurity phase in the Fe-doped samples.

5.3.5.3 Cycling Stability

Figure 5.43a shows the cycling stability of all Fe-doped cathode materials synthesized at 1000 °C compared to the undoped LNMO-1000 °C after 300 cycles at room temperature. They have been cycled with a current rate of C/2 in the voltage range of 3.5-5.0 V.

Among all cathode materials, the $LNF_{0.2}MO$ delivers the highest initial capacity which is ~134 mAh g^{-1}. The initial capacities delivered are 124 mAh g^{-1} and 117.4 mAh g^{-1} for $LNF_{0.3}MO$ and $LNF_{0.4}MO$ cathode materials, respectively. The highest absolute capacity is delivered by $LNF_{0.2}MO$ as it has the lowest amount of impurity phases, therefore, more electrochemically active fraction is available per gram. Concerning absolute capacity the samples can be ordered as $LNF_{0.2}MO > LNMO > LNF_{0.3}MO > LNF_{0.4}MO$. Moreover, the $LNF_{0.2}MO$ exhibits the highest capacity retention (92 %) after 300 cycles at RT.
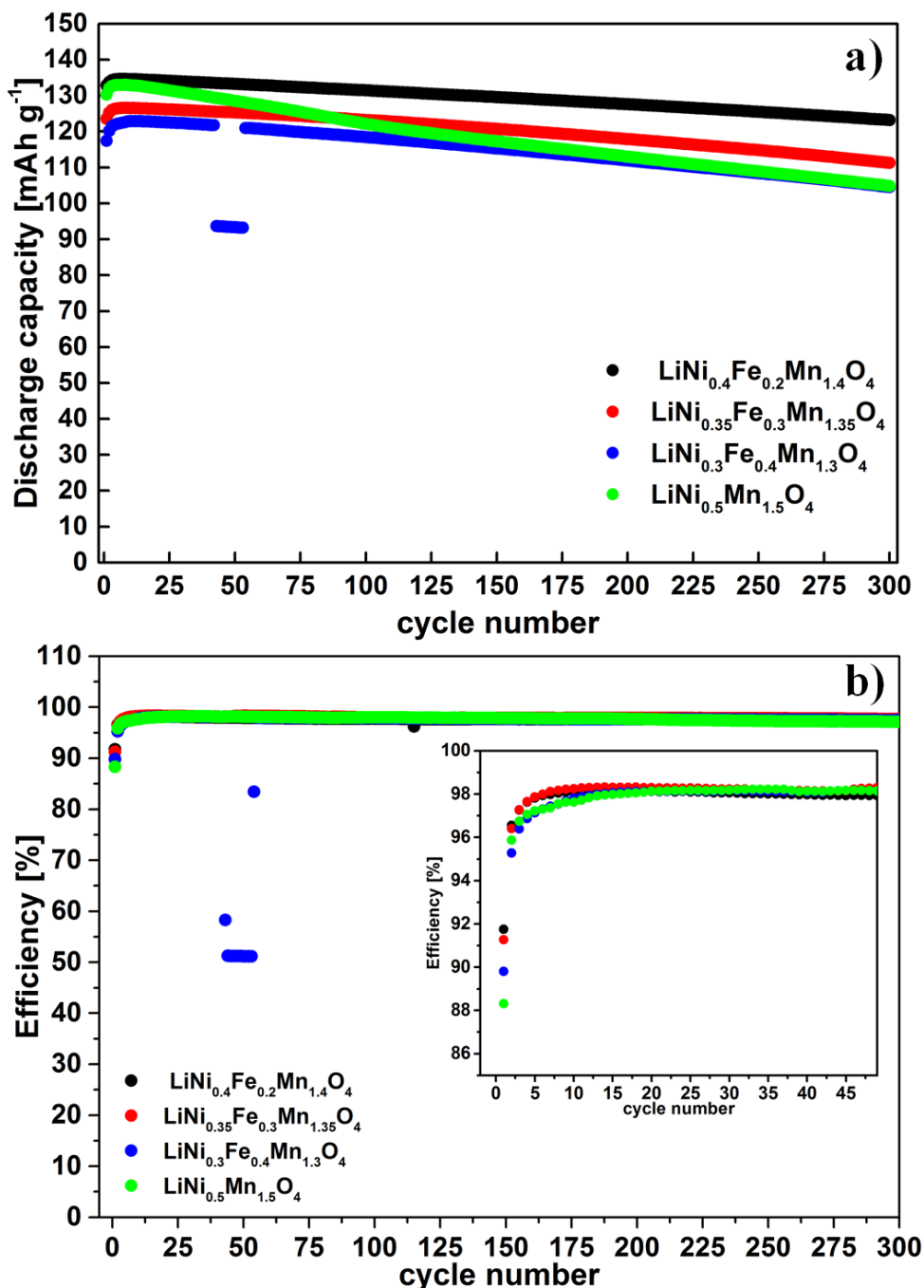
Figure 5.43: a) Discharge capacity vs. cycle number plots of Fe-doped and undoped LNMO-1000 °C cathode materials cycled at C/2 rate between 3.5-5.0 V at RT. b) Coulombic efficiencies vs. cycle number plots for the cycling mentioned in a). Inset figure shows the zoom region of coulombic efficiency plots for 50 cycles.

The inset in Figure 5.43b shows that $LNF_{0.2}MO$ has the highest first cycle coulombic efficiency. Moreover, all Fe-doped materials have higher first cycle coulombic efficiency than the parent LNMO. During the following cycles, the coulombic efficiency

increases for all materials and reaches $\sim$98 %. Hence, it can be concluded that the coulombic efficiency in the first cycle is improved by Fe-doping into the LNMO material.

Even though the $LNF_{0.3}MO$ and $LNF_{0.4}MO$ have lower BET surface area (4.87 m^2/g and 4.76 m^2/g, respectively) than the $LNF_{0.2}MO$ (11.16 m^2/g) material, their capacity retention is much lower (89 % and 87 % for $LNF_{0.3}MO$ and $LNF_{0.4}MO$, respectively, after 300 cycles). It should be noted that the capacity fading increases with increasing Fe-doping, i.e increasing impurity phases and amount of Mn^{3+} in the sample. Hence, the disproportionation of Mn^{3+} and the dissolution of divalent Mn-ions in the electrolyte as well as the adverse parasitic reactions of the impurity phases with the electrolyte could be suspected as reasons for this deteriorating electrochemical performance. Moreover, the involvement of Li_2MnO_3 phase in the electrochemical reaction could also be contributing to the deterioration. The lowest capacity retention is observed for LNMO-1000 °C (79.5 %). The reason for this inferior electrochemical performance of LNMO-1000 °C could be its highest BET surface area (13.40 m^2/g) compared to the Fe-doped derivatives. In addition, as it is presented in section 5.3.8 (*in situ* synchrotron diffraction investigations), the Fe-doped LNMO samples have a different electrochemical mechanism and an improved structural stability during electrochemical cycling which could also be a reason of the enhanced cycling stability [77].

5.3.5.4 Rate Capability

The rate capability performance of all Fe-doped cathodes is shown in Figure 5.44. The results were obtained in the voltage range 3.5-5.0 V by holding the charging current rate constant (C/2) and varying the discharging current rates. Table 5.11 shows the discharge capacities as percentages of the capacity delivered at C/2 current rate.
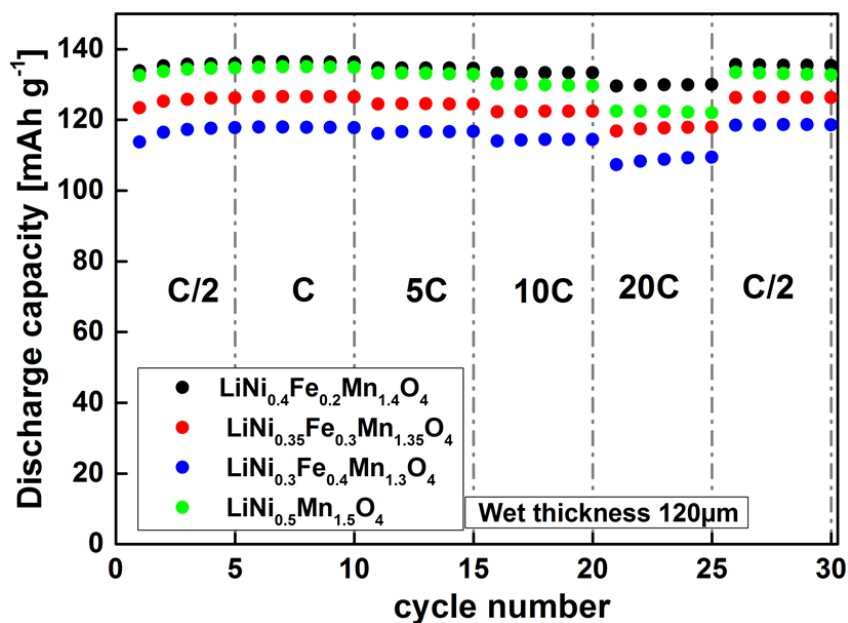
Figure 5.44: Discharge capacity vs. cycle number plots of Fe-doped cathode materials compared to LNMO-1000 °C at C/2 charge rate and varied discharge rates.

Sample	Discharge Capacity (mAh g^{-1}) at C/2	The discharge capacity as percentage of the capacity delivered at C/2			
		1C	5C	10C	20C
LNMO	134	100%	99%	97%	91%
LNF$_{0.2}$O	135	100%	100%	99%	96%
LNF$_{0.3}$O	125	100%	98%	98%	94%
LNF$_{0.4}$O	116	100%	100%	98%	93%

Table 5.11: The discharge capacities obtained at different C-rates for Fe-doped and undoped LNMO-1000 °C cathode materials.

The discharge capacities delivered by LNF$_{0.3}$MO and LNF$_{0.4}$MO samples are lower than LNF$_{0.2}$MO and LNMO-1000 °C cathode materials (see Figure 5.43). However, all Fe-doped samples have superior rate capability performance than the parent LNMO-1000 °C, especially at high C-rates applied (10 C and 20 C). Among all cathode materials, LNF$_{0.2}$MO has the best performance related to discharge capacities at all C-rates. This superior high-rate performance of Fe-doped LNMO derivatives could be again attributed to their high structural stability as well as the improved kinetics during

electrochemical Li-intercalation/deintercalation which will be discussed in detail in section 5.3.8.

Moreover, it was showed in previous section that the cycling stabilities of all Fe-doped samples are better that the parent LNMO-1000 °C. In addition, $LNF_{0.2}MO$ has higher initial absolute capacity than the parent LNMO-1000 °C. Taking into account that the higher rates, 10 C and 20 C, were applied from 15-25 cycles, the superior rate capability performance of Fe-doped samples at these rates might also be due to its less capacity degradation compared to LNMO-1000 °C. This might result in lower delivered capacities than $LNF_{0.2}MO$ especially at the higher rates 10 C and 20 C and poorer rate capability than all Fe-doped samples. In order to clarify the reason behind the enhanced high-rate behavior of Fe-doped samples, the cycling stability performance at high C-rate of LNMO-1000 °C and $LNF_{0.2}MO$ cathode materials were conducted with two different experimental conditions; 1) charging at C/2 - discharging at 20 C (see Figure 5.45a) and 2) charging at 20 C -discharging at 20 C (see Figure 5.45b). For the first condition, there is a different behavior for the first couple of cycles in discharge capacity values for both samples. That observation cannot be seen for the second condition. It is not clear but this behavior might relate with different charge and discharge rates. Different phenomena can contribute in this case such as structural conditioning, changing of the morphology of the electrodes or involvement of the SEI etc. Besides this different behavior, $LNF_{0.2}MO$ delivered a higher absolute capacity than the undoped LNMO-1000 °C at both experimental conditions applied. Additionally, its capacity retention is higher than the parent LNMO-1000 °C. The enhanced rate capability performance of Fe-doped samples may be due to their increased structural stability and improved Li intercalation/de-intercalation kinetics comparing to LNMO-1000 °C.
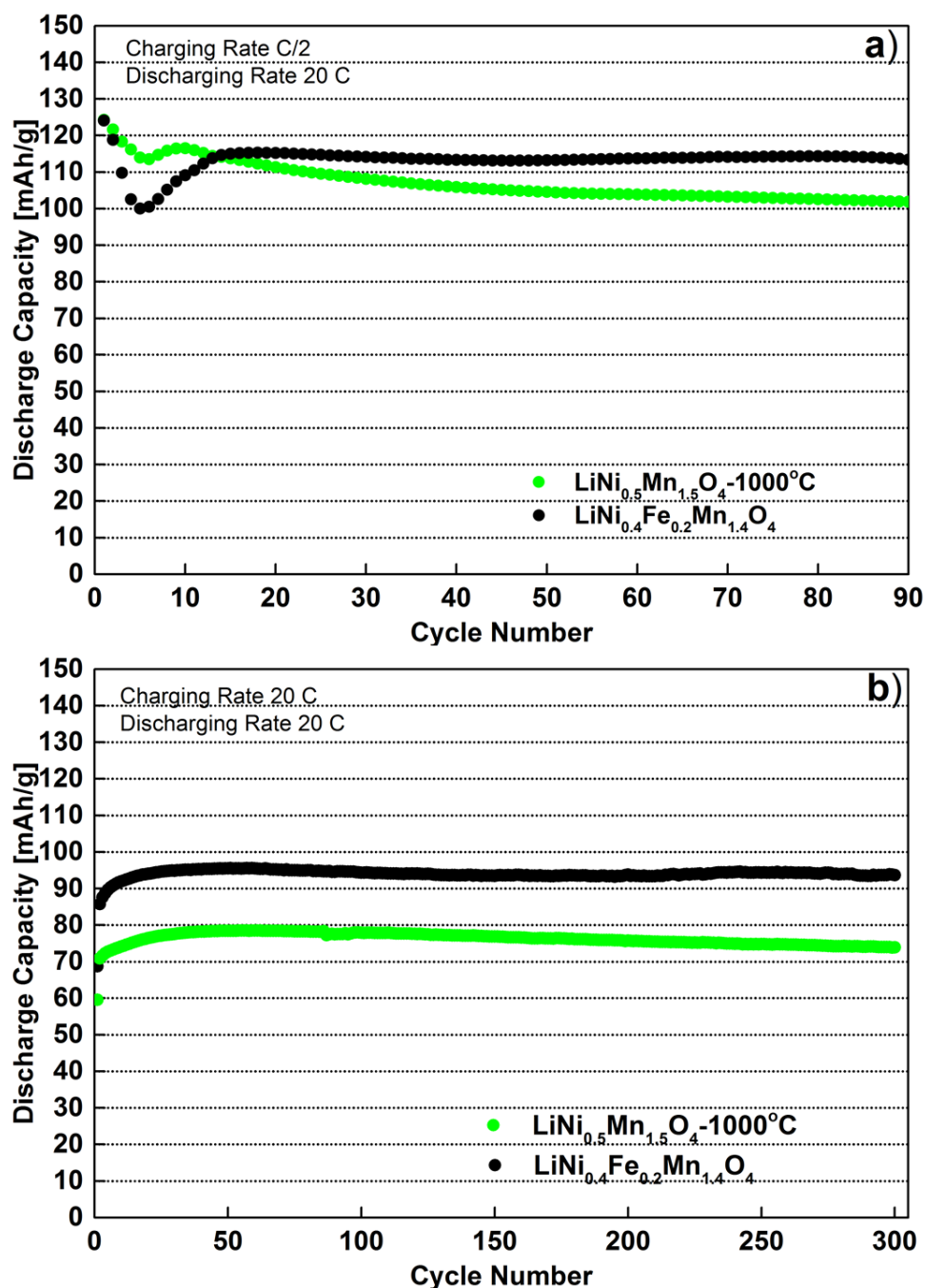
Figure 5.45: Cycle number vs. discharge capacity plots of Fe-doped and undoped LNMO-1000 °C cathode materials at a) C/2 charge and 20 C discharge rates and b) 20 C charge and discharge rate in the voltage range 3.5-5.0 V at RT.

5.3.6 Electrochemical Performances of $LiNi_{0.4}Fe_{0.2}Mn_{1.4}O_4$ in Comparison with $LiNi_{0.5}Mn_{1.5}O_4$-1000 °C Cathode Material at Elevated Temperature (55 °C)

5.3.6.1 Cycling Stability

Since the $LNF_{0.2}MO$ material exhibited the best cycling stability at RT among all Fe-doped LNMO spinel materials, its elevated temperature (55 °C) cycling performance was investigated. Figure 5.46 shows the comparison of cycling stabilities at 55 °C for $LNF_{0.2}MO$ and undoped LNMO-1000 °C. Minimum two cells of each material with similar electrode mass loadings were cycled at 55 °C. For the first 70 cycles, the cells of each material showed a reproducible behavior which started to differ greatly in the following cycles. As different from the RT cycling performance, the undoped LNMO-1000 °C exhibited a higher absolute capacity than $LNF_{0.2}MO$ which could be due to the increased Li^+ diffusion at high temperature. Moreover, the parasitic reactions taking place could also add contribution to this increased absolute capacity. Even though the absolute capacity delivered by LNMO-1000 °C is higher, the capacity retention is again slightly lower than $LNF_{0.2}MO$.
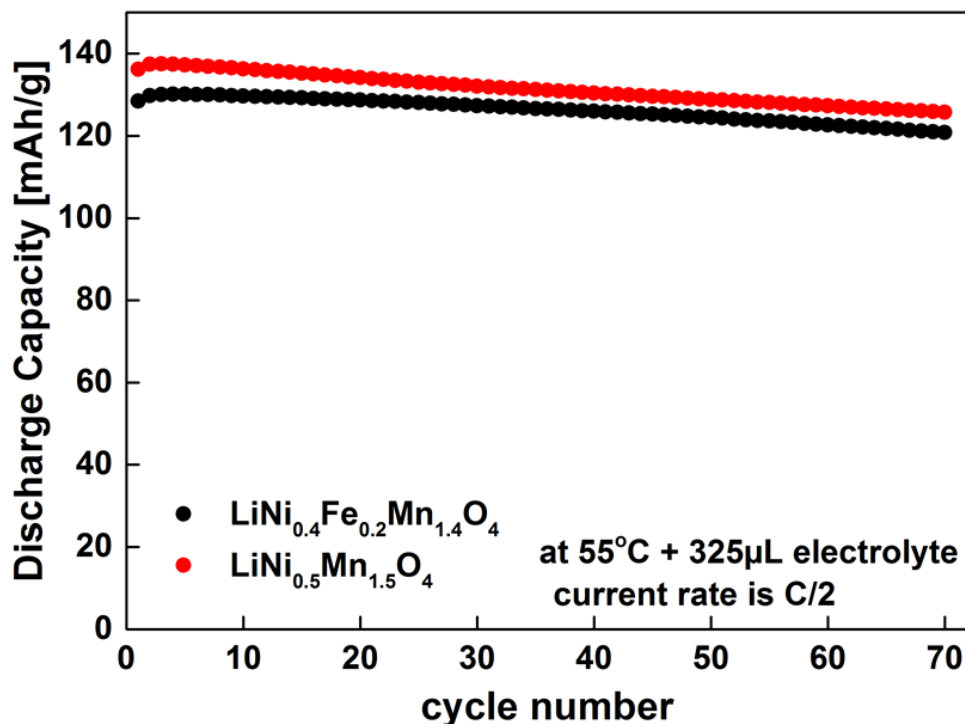
Figure 5.46: Discharge capacity vs. cycle number plots of $LNF_{0.2}MO$ and undoped LNMO-1000 °C cathode materials cycled at C/2 in the voltage range 3.5-5.0 V at 55 °C.

While $LNF_{0.2}MO$ exhibits 93 % capacity retention after 70 cycles, LNMO-1000 °C shows only 91 % capacity retention at 55 °C whereas it is 99 % and 95.5 % at RT after 70 cycles for $LNF_{0.2}MO$ and LNMO-1000 °C, respectively. The reason could be again the increased surface area, hence increased parasitic reactions occurring at elevated temperature for LNMO-1000 °C.

5.3.7 Thermal Stability of Initial and Completely Charged LNMO-1000 °C and $LNF_{0.2}MO$ Cathode Materials

Since various electrochemical reactions occur within the cell which might increase the temperature and can cause fires or explosions, thermal stability of the electrode materials is an important parameter for the battery safety. It has already been reported that Fe containing spinel cathode materials have an increased onset temperature for

106

thermal degradation [39]. The thermal stability experiments which are related to the structural stability of initial and charged samples were performed with TG-DSC analysis, as well as with XRD.

The TG-DSC analyses of the materials are shown in Figure 5.47. The experiment was conducted at a heating rate of 5 °C/min under Ar. The initial electrodes (which consist of the mixture of 80 % (w/w) the active material, 10 % (w/w) super C 65 carbon (TIMCAL) and 10 % (w/w) polyvinylidenefluoride (Solef PVdF 6020 binder, Solvay)) were heated until 400 °C. For the completely charged electrodes, the final temperature was limited to 270 °C as it is already reported that the onset temperature of degradation of completely charged LNMO is 220 °C ([39]). Hence, by chosing the temperature above 220 °C, it can be surely assumed that the thermal LNMO-1000 °C of degradation already started and a comparison with $LNF_{0.2}MO$ will illustrate if such a degradation exists for it as well.

TG profiles show that the weight loss is higher for the charged samples than the initial samples for both LNMO-1000 °C and $LNF_{0.2}MO$ cathode materials. Moreover, the weight loss is slightly higher for charged LNMO-1000 °C (1.15 % at 270 °C) sample than charged $LNF_{0.2}MO$ (1.1 % at 270 °C). In DSC profiles, the peak at 170 °C corresponds to the melting of PVdF which is the known melting point of commercial PVdF 6020 [39].
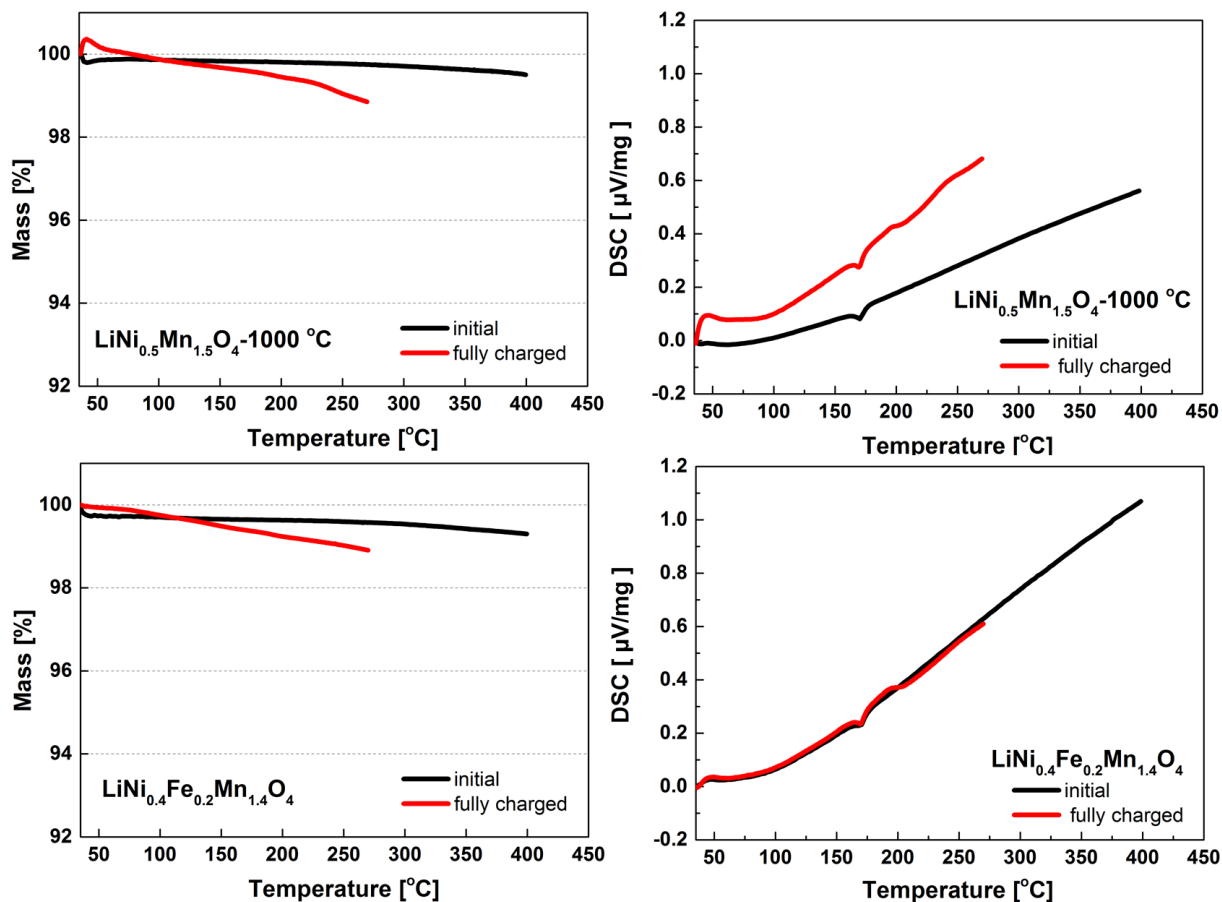
Figure 5.47: TG (left) and DSC (right) profiles in argon at a rate of 5 °C/min, for initial and charged state of LNMO-1000 °C and LNF$_{0.2}$MO cathode materials.

The initial and charged electrodes were subjected to XRD analyses (Mo-K$_{\alpha 1}$ radiation) before and after TG experiments and the results are shown in Table 5.12.

The bimixture contents in initial cathode mixtures of LNMO-1000 °C (3.26 %) and LNF$_{0.2}$MO (1.87 %) as well as the lattice parameter of main phases (8.1776(1) Å and 8.1970(1) Å, respectively) slightly increase after the TG experiments. This could be due to the slight oxygen loss in presence of C under Ar.

Two spinel phases with slightly different lattice parameters (8.0069(1) Å and 8.0839(1) Å) exist in case of LNMO-1000 °C after charging. The bimixture content is 3.59 %. The lattice parameters of these two main phases slightly increase (8.0091(1) Å and 8.091(1) Å), however, a third spinel phase phase was obtained after the TG experiments (270 °C) for charged LNMO-1000 °C cathode mixture with a small

phase fraction (4.4 %) and considerably increased lattice parameter (8.168(2) Å). The expansion of the lattice parameters after TG experiments are, 0.03 %, 0.09 % and 1.03 %. The disintegration of the structure reveals that the material is not stable to thermal degradation in charged state. This could be due to the increased oxygen loss in presence of C under Ar. Since the oxidation states of Ni and Mn are higher on the charged states which are less stable than their lower oxidation states together with the high temperature treatments, the material will lose more oxygen than its initial state.

Sample	Fraction of Impurity phase %	Fraction of Main phase %	Lattice Parameter (Main phase)	Lattice Parameter (Impurity phase)
LNMO initial before TG	3.26	96.74	8.1776(1) Å	8.298(1) Å
LNMO initial after TG	4.39	95.61	8.1779(1) Å	8.300(1) Å
LNMO charged before TG	3.59	89.12 7.29	8.0069(1) Å 8.0839(4) Å	8.290(3) Å
LNMO charged after TG	4.21	65.82 27.31 4.40	8.0091(1) Å 8.091(1) 8.168(2) Å	8.256(1) Å
LNF$_{0.2}$MO initial before TG	1.87	98.13	8.1970(1) Å	8.26(1) Å
LNF$_{0.2}$MO initial after TG	4.50	95.50	8.1992(1) Å	8.240(2) Å
LNF$_{0.2}$MO charged before TG	1.94	98.06	8.0458(1) Å	8.26(1) Å
LNF$_{0.2}$MO charged after TG	4.85	95.15	8.1157(2) Å	8.2482(1) Å

Table 5.12: Rietveld refinement results of initial and charged LNMO-1000 °C and LNF$_{0.2}$MO samples before and after TG experiments based on space group $Fd\bar{3}m$. The mentioned impurity phase in LNMO-1000 °C is rock-salt Ni$_6$MnO$_8$ phase and in LNF$_{0.2}$MO is Fe$_3$O$_4$ spinel phase.

There is only one main spinel phase in the case of charged LNF$_{0.2}$MO cathode material. The lattice parameter (8.04577 Å) slightly increase after the TG experiments (270 °C). The lattice parameter is 8.1157(2) Å after heat treatment and the expansion after TG experiment for charged LNF$_{0.2}$MO sample is 0.86 %. The observation shows that the LNF$_{0.2}$MO cathode material has different degradation mechanism than the parent LNMO-1000 °C sample which is more stable to a thermal degradation.

5.3.8 Investigations on Structural Evolutions of Fe-doped LNMO Cathode Materials During Electrochemical Cycling using Synchrotron Diffraction

5.3.8.1 Analysis of Synchrotron Diffraction Patterns Obtained during Charging and Discharging at C/2 Current Rate

$LNF_{0.2}MO$ cathode material was cycled with a charge/discharge rate of C/2 in the voltage range of 3.5-5.3 V in order to investigate the Li intercalation/deintercalation mechanism. The upper cut-off voltage was extended up to 5.3 V for the $LNF_{0.2}MO$ cathode for the *in situ* investigations in order to check any structural changes arising from the $Fe^{3+} \rightleftharpoons Fe^{4+} + e^-$ redox reactions. A re-intercalation of ~ 0.92 moles of lithium into $LNF_{0.2}MO$ at the end of the first discharge was observed. This electrochemical performance is almost the same as that observed with the Swagelok®-type cell.

The structural evolution during the charge and discharge processes for $LNF_{0.2}MO$ sample is displayed in Figure 5.48 with selected 2θ regions, where black and red lines correspond to the charge and discharge regions, respectively.
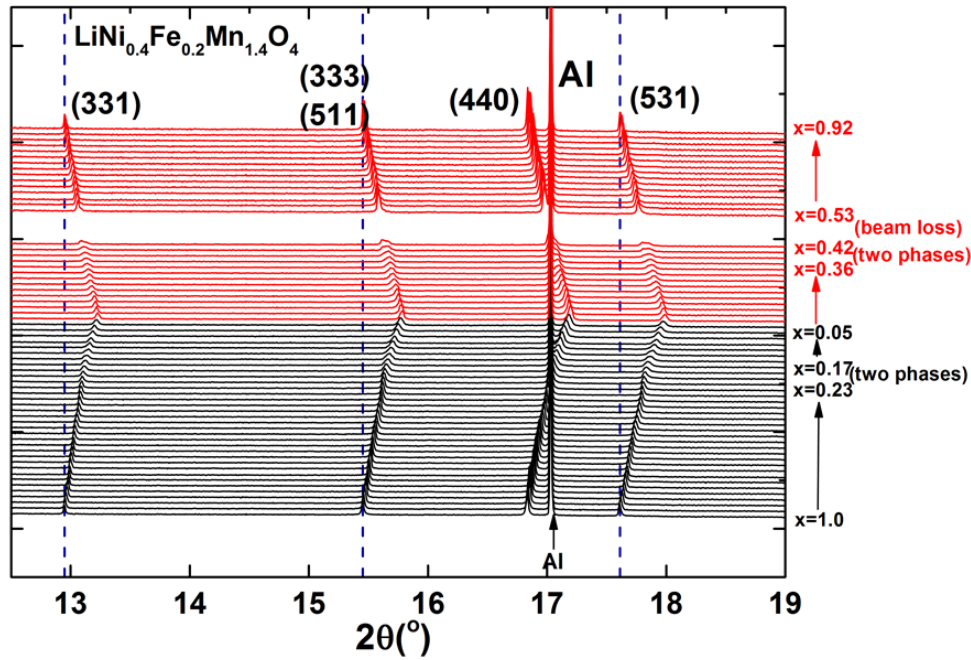
Figure 5.48: Selected 2θ regions of the *in situ* synchrotron diffraction patterns of $LNF_{0.2}MO$ cathode material measured at the MSPD Beamline during the 1^{st}cycle. The gap is due to beam loss during injection.

A different structural evolution is observed for the $LNF_{0.2}MO$ material in comparison with the parent LNMO-1000 °C. For the $LNF_{0.2}MO$ sample, the electrochemical mechanism is very similar to a solid-solution mechanism (see Figure 5.48), where mainly a single cubic spinel phase remains throughout the complete cycle with the lattice parameter decreasing during delithiation and increasing during lithiation. However, there is also a phase separation into a second cubic spinel phase ($Fd\bar{3}m$) in $LNF_{0.2}MO$ from x =0.23 to x = 0.017 during charging and it starts from x = 0.36 during discharging. Due to the beam loss, the two phase region is not clear during discharging process. The obtained lattice parameters for the two cubic spinel phases in $LNF_{0.2}MO$ are very close to each other, different to the LNMO material (see Figure 5.12). The above observations could imply that the origin of the phase separation in $LNF_{0.2}MO$ could be a kinetic limitation of the Li diffusion into/from the structure rather than a true phase-transition mechanism [78]. Figure 5.49 displays the evolution of the lattice parameter as a function of the Li content. For the $LNF_{0.2}MO$ sample, the

unit cell parameter of the second cubic spinel phase undergoes a constant decrease and increase during charging and discharging, respectively, similar to the main cubic spinel phase which proves that the new phase formed is also electrochemically active. Additionally, the formation of this second phase is reversible because it disappears at the end of the discharging process. Furthermore, the phase fraction analysis shown in Figure 5.50 supports this assumption, like in the case of the undoped LNMO-1000 °C cathode material.
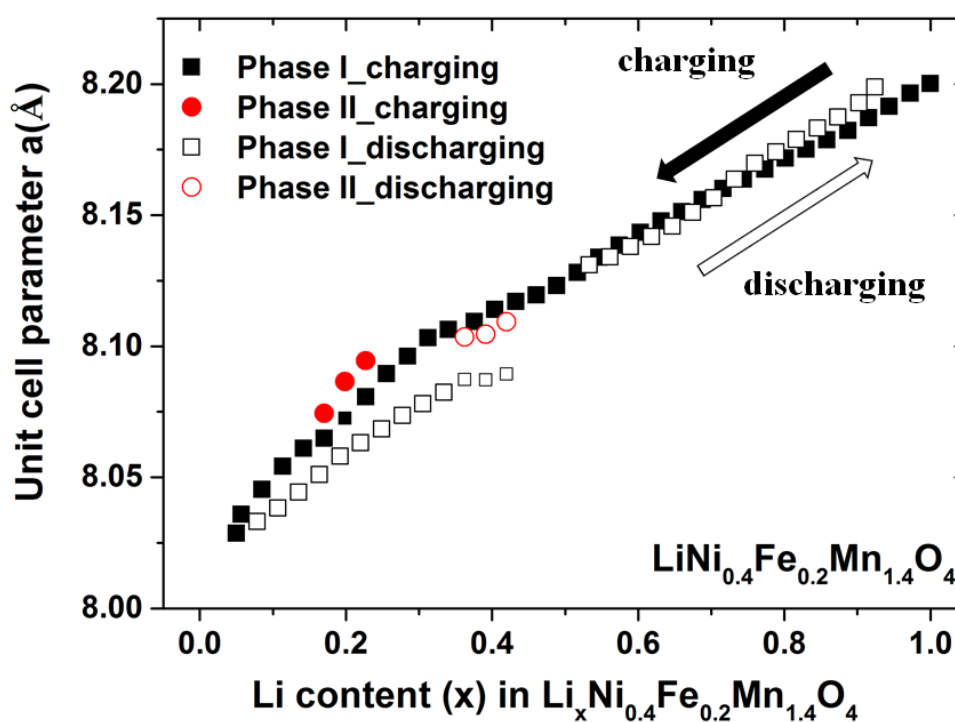
Figure 5.49: Change in the unit cell parameter as a function of number of moles of Li (x) remaining in the structure for $Li_xNi_{0.4}Fe_{0.2}Mn_{1.4}O_4$. The red circles represent the unit cell parameter changes of the additional spinel phase.
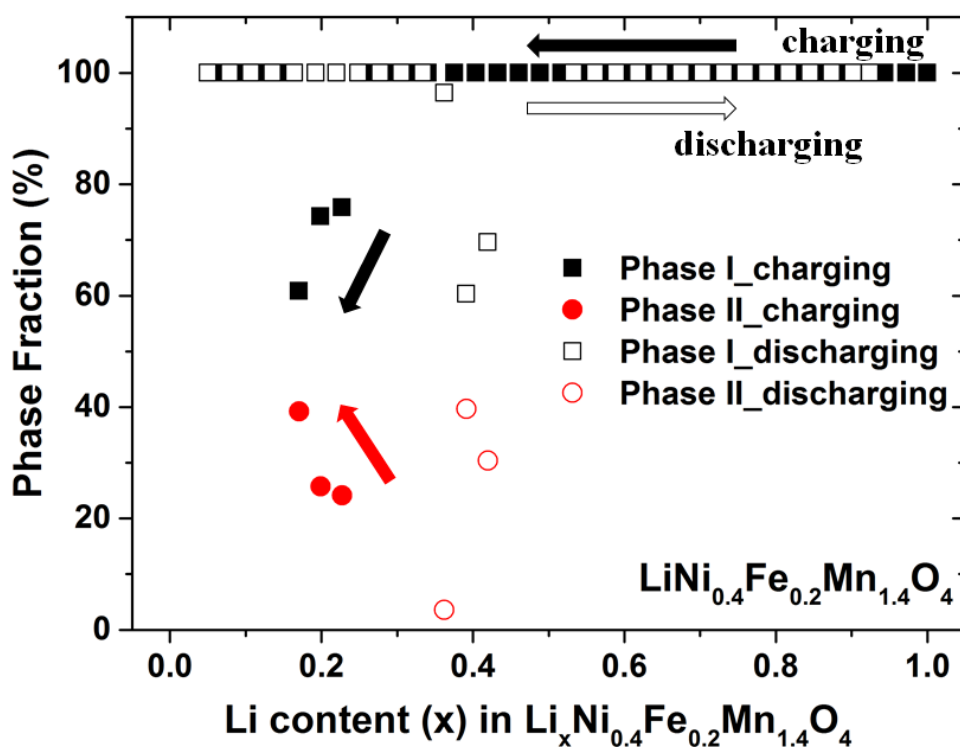
Figure 5.50: The phase ratios vs. Li content plots during cycling for $LiNi_{0.4}Fe_{0.2}Mn_{1.4}O_4$.

The shrinkage of the unit cell at the end of the first charge as calculated from the Rietveld refinement results is 2.09 % for $LNF_{0.2}MO$ (see table 5.13). The unit cell expansion at the end of discharge is 2.08 %. These unit cell contraction and expansion values are calculated from the lattice parameter differences between the beginning and the end of the 1st charge and discharge, respectively. This indicates the re-insertion of close to 1 mole of Li ions back into the structure.

LNF$_{0.2}$MO			
	Lithium content	a($\mathring{A}$)	Shrinkage/ Expansion(%)
Initial	1	8.2001(4)	
End of 1st charge	0.05008	8.0286(7)	2.09
End of 1st discharge	0.92422	8.1989(4)	2.08

Table 5.13: Rietveld refinement results of LNF$_{0.2}$MO based on the *in situ* synchrotron diffraction data. (The percentage of the shrinkage is the difference between the initial state and end of 1st charge and the percentage of the expansion is the difference between the end of 1st charge and end of 1st discharge state)

The micro-strain analysis obtained from Rietveld refinement is shown in Figure 5.51. The lattice strain increased for LNF$_{0.2}$MO cathode material at the voltage region where the Ni^{2+}/Ni^{4+} redox couple exists, similar to that observed for undoped LNMO-1000 °C and also where the Fe^{3+}/Fe^{4+} redox couple is active. The overall change in lattice strain that occurs during cycling is lower for LNF$_{0.2}$MO compared to LNMO-1000 °C (see Figure 5.14). Therefore, the LNF$_{0.2}$MO structure is more relaxed during Li intercalation/de-intercalation in comparison with its parent LNMO-1000 °C structure, which could result in a faster Li-ion diffusion. This improved structural stability for LNF$_{0.2}$MO during cycling is probably the reason for the enhanced cycling stability of this material.
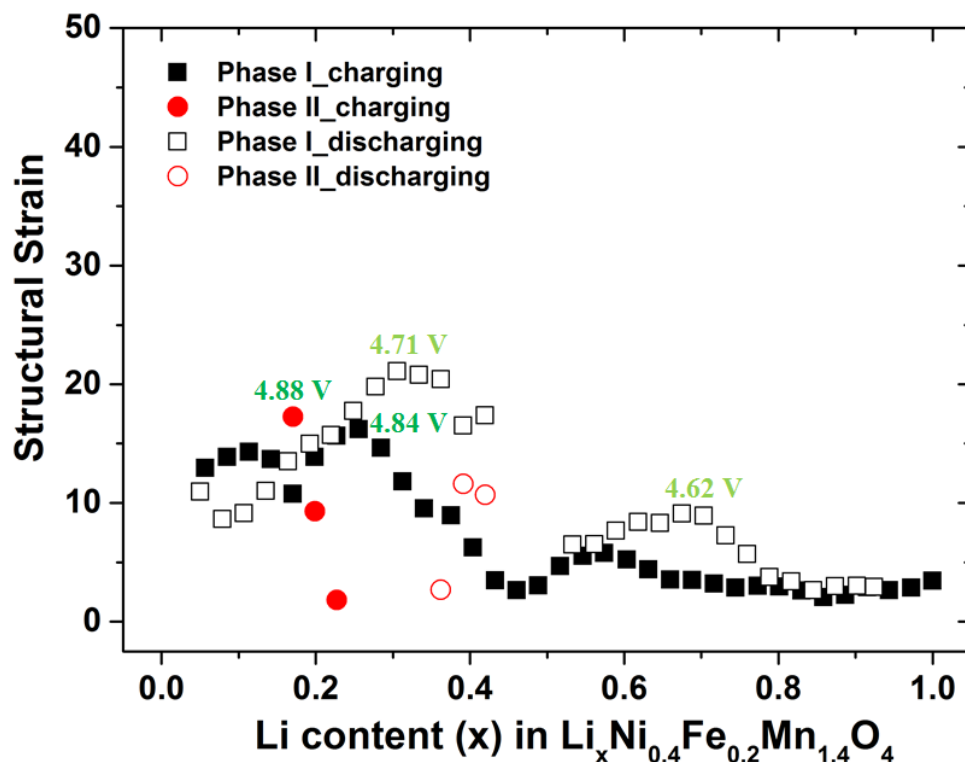
Figure 5.51: The micro-strain analysis of $LiNi_{0.4}Fe_{0.2}Mn_{1.4}O_4$ cathode material. The maximum strain is given in the Fullprof microstructural output file as $\frac{d}{\Delta d} \times 10^{-4}$.

In situ investigation of the lithium intercalation mechanism in $LNF_{0.3}MO$ and $LNF_{0.4}MO$ samples have also been performed in ALBA at the MSPD beamline using *in situ* coin cells. The cells were cycled at C/2 in the voltage range of 3.5-5.3 V. Figure 5.52 displays the structural evolution during charge and discharge with selected 2θ regions, where black and red lines correspond to the charge and discharge regions, respectively.
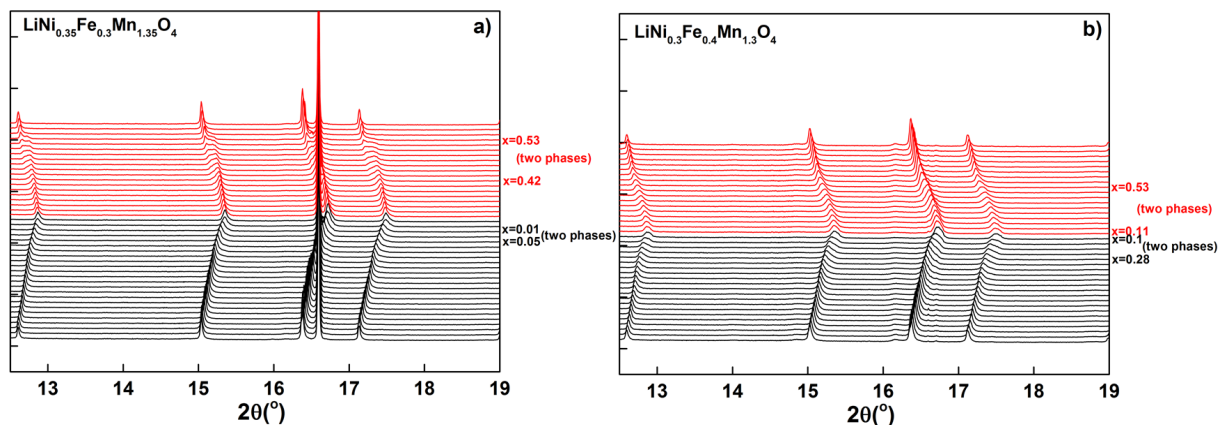
Figure 5.52: Selected 2θ regions of the *in situ* synchrotron diffraction patterns of a) $LNF_{0.3}MO$ and b) $LNF_{0.4}MO$ cathode materials measured at MSPD during the 1st cycle.

A similar lithium de-/intercalation mechanism occurs for the $LNF_{0.3}MO$ and $LNF_{0.4}MO$ samples as it was observed for $LNF_{0.2}MO$ material. The electrochemical mechanism is again close to a solid-solution mechanism for both cases. However, there is also a phase separation into a second cubic spinel phase during charging and discharging.

As it was mentioned before, all Fe-doped cathode materials contain an additional Fe_3O_4 spinel phase. The phase fraction of this phase is very small in $LNF_{0.2}MO$ as can bee seen in neutron measurements. Since the *in situ* cell consists of a stack of several components like Al current collector, lithium metal, separator etc. there is an increased background and this phase is not detectable in $LNF_{0.2}MO$ *in situ*. However, since the initial $LNF_{0.4}MO$ powder has the highest amount of Fe_3O_4 phase, this phase is detectable in the diffraction patterns obtained during *in situ* experiments for $LNF_{0.4}MO$. In principle, Fe_3O_4 is used as anode [79] material which is electrochemically active below 3.0 V. It is not expected to be active in the voltage range which is used in this work. It has been observed that the lattice parameters of Fe_3O_4 in $LNF_{0.4}MO$ obtained from Rietveld refinement are 8.318(2) Å, 8.314(3) Å and 8.319(1) Å before cycling, at the end of charging and at the end of discharging, respectively. In order to analyze the XRD patterns of $LNF_{0.4}MO$ by Rietveld refinements, several parameters, models

116

and the phases Al, Li, main spinel, Fe_3O_4 spinel and Li_2MnO_3 have been taken into account. Considering this point and taking into account the standard deviations, the differences among the lattice parameters obtained for initial, charged and discharged states of $LNF_{0.4}MO$ are negligible. It can be concluded that the Fe_3O_4 spinel phase is not active during cycling.

5.4 Rare Earth Elements doped $LiNi_{0.495}M_{0.01}Mn_{1.495}O_4$ and $LiNi_{0.425}M_{0.05}Mn_{1.5}O_4$ (*M* = La, Nd or Sm) Spinels as High-Volt Cathode Materials

In this section the effects of rare earth metal doping, specifically La, Nd and Sm, on the LNMO concerning structure, morphology and electrochemical performances will be studied. The rare earth elements are divided into two groups as light rare earth elements (La, Ce, Pr, Pm, Nd and Sm) and heavy rare earth elements (Eu, Gd, Tb, Dy, Ho, Er, Tm, Yb and Lu). The heavy rare earth elements are more expensive than the light rare earth elements. The rare earth metal doped LNMO materials were synthesized at 1000 °C final calcination temperature. For the construction of the compositions, two possibilities were taken into account: $LiNi_{0.5-x}^{2+}M_{2x}^{3+}Mn_{1.5-x}^{4+}O_4$ (x=0.005) which is completely stoichiometric (as the spinel structure AB_2O_4) and $LiNi_{0.5-3x}^{2+}M_{2x}^{3+}Mn_{1.5}^{4+}O_4$ (x= 0.025) which contains octahedral vacancies similar to the Ru-doped LNMO sample.

5.4.1 Structural Analyses

If the rare earth metal ions (La, Nd and Sm) having bigger size compared to 3d transition metal ions, could really be inserted into the spinel structure they would widen the main spinel lattice. As a result, the Li-diffusion kinetics may be improved which may lead to a better rate capability. The results of XRD refinements (see Figure 5.53) show that all rare-earth doped samples have cubic spinel structure with $Fd\bar{3}m$

space group and again an impurity phase with rock-salt structure (Ni_6MnO_8) exists in all of them. Besides that, the La-doped samples: $LiNi_{0.495}La_{0.01}Mn_{1.495}O_4$ ($LNLa_{0.01}MO$) and $LiNi_{0.425}La_{0.05}Mn_{1.5}O_4$ ($LNLa_{0.05}MO$) contain an additional $LaMnO_3$ phase with space group $R\bar{3}c$. The Nd-doped samples: $LiNi_{0.495}Nd_{0.01}Mn_{1.495}O_4$ ($LNNd_{0.01}MO$) and $LiNi_{0.425}Nd_{0.05}Mn_{1.5}O_4$ ($LNNd_{0.05}MO$) have an additional $NdMnO_3$ phase which belongs to the space group *Pnma* and there exists an additional $SmMn_2O_5$ phase (space group *Pbam*) in the Sm-doped samples: $LiNi_{0.495}Sm_{0.01}Mn_{1.495}O_4$ ($LNSm_{0.01}MO$) and $LiNi_{0.425}Sm_{0.05}Mn_{1.5}O_4$ ($LNSm_{0.05}MO$).
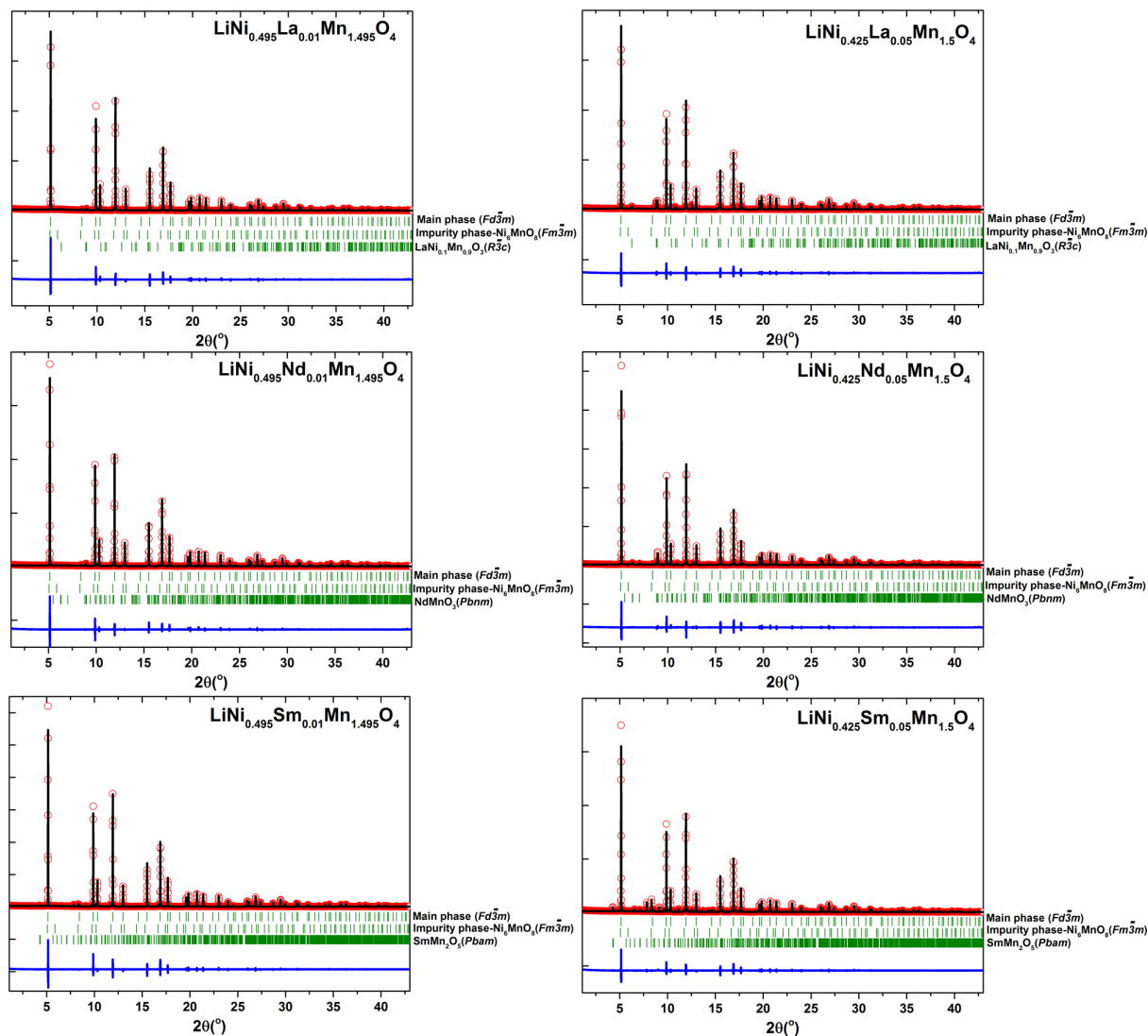
Figure 5.53: Rietveld refinement results based on synchrotron diffraction patterns of rare earth metal doped $LiNi_{0.495}M_{0.01}Mn_{1.495}O_4$ and $LiNi_{0.425}M_{0.05}Mn_{1.5}O_4$ ($M=$ La, Nd, Sm) materials measured in 0.5 mm capillaries.

The Rietveld refinement results based on synchrotron diffraction data are listed in Table 5.14. The lattice parameters of all rare earth doped samples are very similar to each other and also to parent undoped LNMO sample. By increasing the amount of rare earth metals inside the samples, the phase fraction of rock salt impurity phase decreased, instead, the fraction of the rare earth elements containing second impurity phase increased for all La, Nd and Sm doped LNMO materials (see Table 5.14).

Samples	Atom Site	x=y=z	a(Å)	Volume (Å^3)	Fraction of rock-salt phase % (Ni$_6$MnO$_8$)	Fraction of rare-earth phase %	R$_{wp}$(%)
LNLa$_{0.01}$MO	Li$_{8a}$	0.125	8.1737(1)	546.44(1)	3	2	11.1
	Ni$_{16d}$	0.500					
	Mn$_{16d}$	0.500					
	O$_{32e}$	0.2639(3)					
LNLa$_{0.05}$MO	Li$_{8a}$	0.125	8.1755(1)	546.44(1)	2	7	9.38
	Ni$_{16d}$	0.500					
	Mn$_{16d}$	0.500					
	O$_{32e}$	0.2639(3)					
LNNd$_{0.01}$MO	Li$_{8a}$	0.125	8.1765(1)	546.63(1)	5	2	10.6
	Ni$_{16d}$	0.500					
	Mn$_{16d}$	0.500					
	O$_{32e}$	0.2638(3)					
LNNd$_{0.05}$MO	Li$_{8a}$	0.125	8.1769(1)	546.72(1)	2	6	12.7
	Ni$_{16d}$	0.500					
	Mn$_{16d}$	0.500					
	O$_{32e}$	0.2639(5)					
LNSm$_{0.01}$MO	Li$_{8a}$	0.125	8.1751(1)	546.36(1)	4	2	11.7
	Ni$_{16d}$	0.500					
	Mn$_{16d}$	0.500					
	O$_{32e}$	0.2644(3)					
LNSm$_{0.05}$MO	Li$_{8a}$	0.125	8.1745(1)	546.23(1)	3	10	9.33
	Ni$_{16d}$	0.500					
	Mn$_{16d}$	0.500					
	O$_{32e}$	0.2640(3)					

Table 5.14: Rietveld refinement results of rare earth metal doped spinels based on synchrotron diffraction data (space group of main spinel phase $Fd\bar{3}m$).

The Rietveld refinements based on the obtained neutron diffraction data are shown in Figure 5.54. Neutron analyses show that the rare earth metals are not present inside the main spinel structure but they form an additional oxide phases belonging to different space groups. The stoichiometry calculation from site occupation factors were not taken into account since the rare earth metals are not inside the spinel phase.
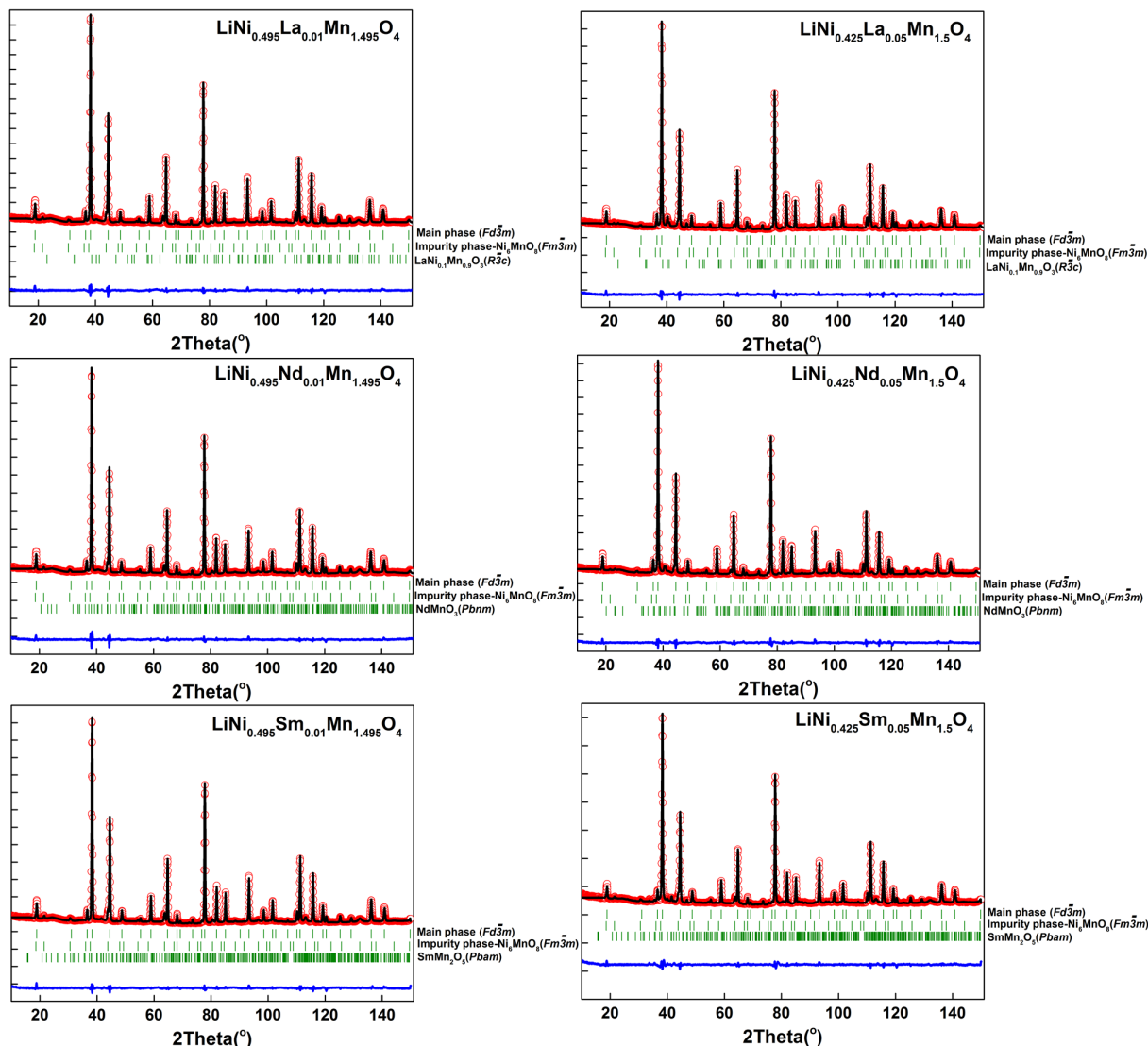
Figure 5.54: Rietveld refinement results based on neutron diffraction data of as prepared rare earth doped powders.

5.4.2 Morphology Studies of initial La, Nd or Sm-doped LNMO powders

SEM images of LNLa$_{0.01}$MO, LNNd$_{0.01}$MO, LNSm$_{0.01}$MO and LNLa$_{0.05}$MO, LNNd$_{0.05}$MO, LNSm$_{0.05}$MO are presented in Figure 5.55a-f, respectively. The particles of LiNi$_{0.495}$$M_{0.01}Mn_{1.495}O_4$ (M = La, Nd or Sm) materials exhibit also pseudo-octahedral shapes with smoother surfaces as the parent LNMO. The obtained particle sizes of LNLa$_{0.01}$MO, LNNd$_{0.01}$MO, LNSm$_{0.01}$MO are 0.5-1 μm, 1-2.5 μm and 1-2 μm, respec-

tively. The particle sizes of $LiNi_{0.425}M_{0.05}Mn_{1.5}O_4$ (M = La, Nd or Sm) samples are different than that of $LiNi_{0.495}M_{0.01}Mn_{1.495}O_4$. The $LiNi_{0.425}M_{0.05}Mn_{1.5}O_4$ samples contain particles with pseudo-octahedral shapes as well as small round shapes. The obtained particle sizes of $LNLa_{0.05}MO$, $LNNd_{0.05}MO$, $LNSm_{0.05}MO$ are 0.2-0.5 μm, 0.2-2 μm and 0.2-1 μm, respectively.
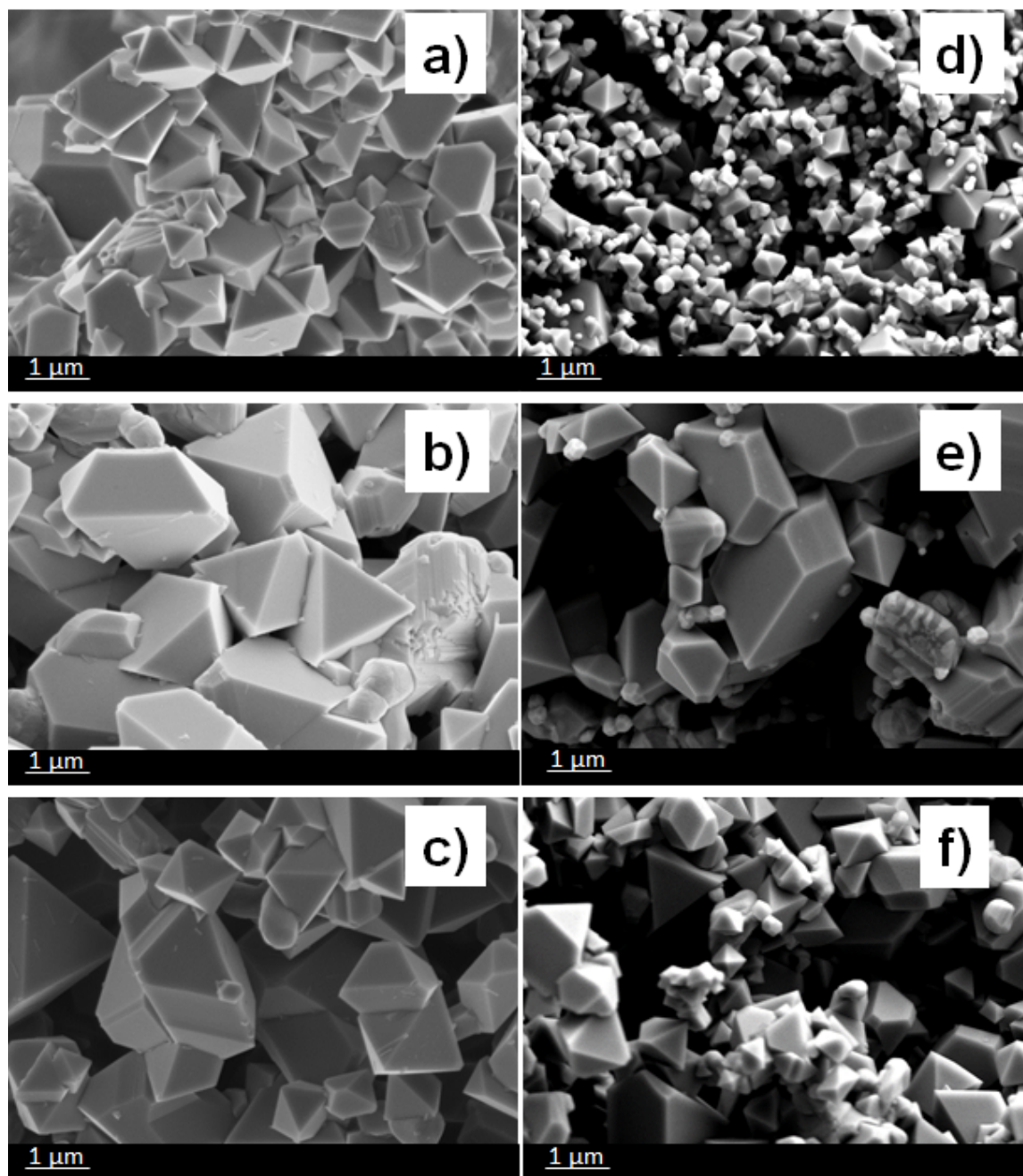
Figure 5.55: SEM images of as prepared a) $LNLa_{0.01}MO$, b) $LNNd_{0.01}MO$, c) $LNSm_{0.01}MO$, d) $LNLa_{0.05}MO$, e) $LNNd_{0.05}MO$ and f) $LNSm_{0.05}MO$ powders.

The particle sizes change greatly with a little change in the amount of rare earth metals inside the samples. To understand the reason for the large change in particle size, back scattered electron images were collected (see Figure 5.56). It has been observed that the small particles have different contrast and they are brighter than the big particles. The elements which have higher atomic number backscatter the electrons more strongly than the ones with lower atomic number resulting in brighter particles on the figure. This observation implies that the smaller particles belong to rare earth metal containing oxides which exist as additional phase inside the samples. Since the $LNLa_{0.05}MO$, $LNNd_{0.05}MO$ and $LNSm_{0.05}MO$ samples have higher amounts of rare earth metals, brighter particles can be seen in these samples more easily.
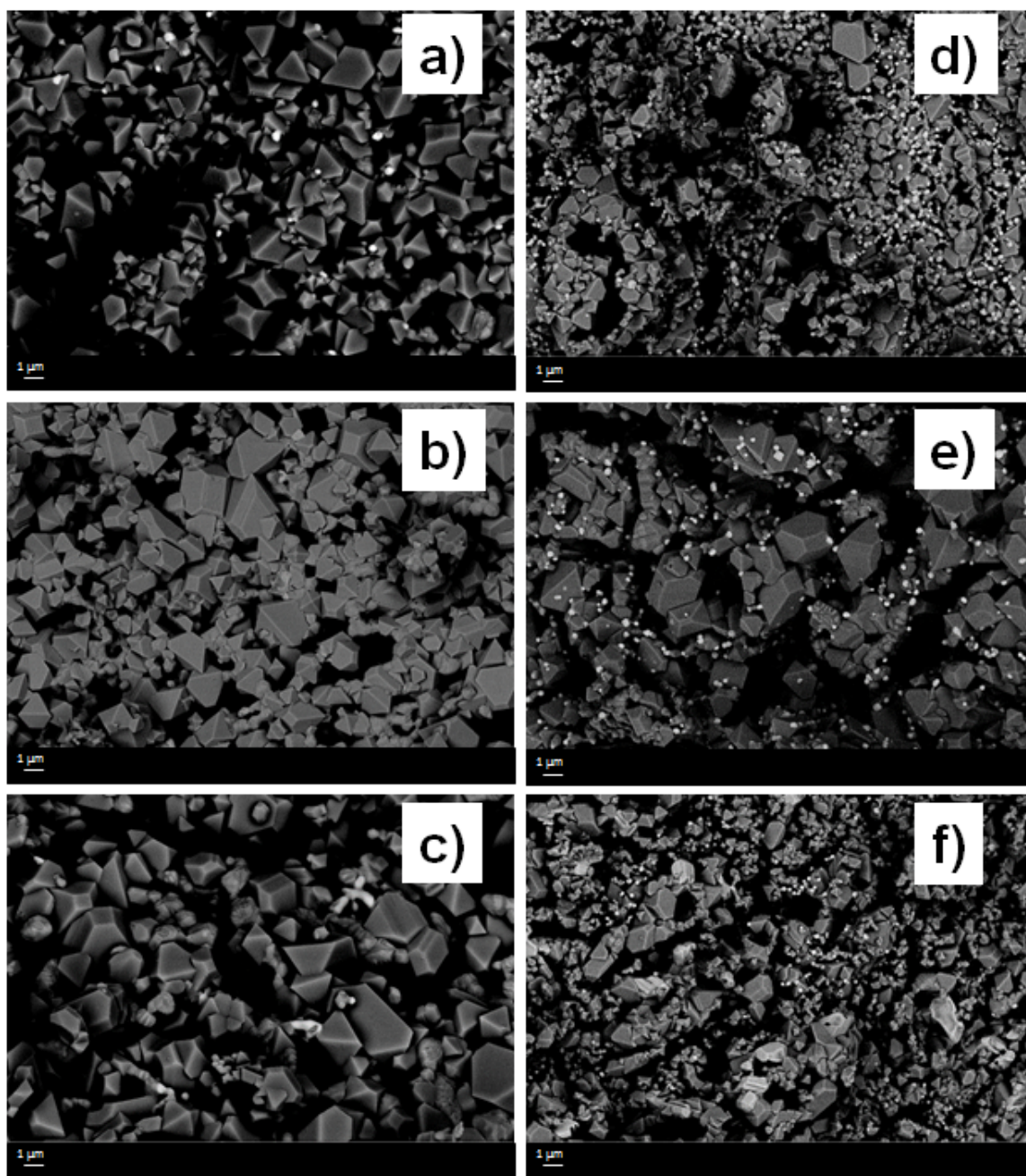
Figure 5.56: Back scattered electron images of as prepared a) $LNLa_{0.01}MO$, b) $LNNd_{0.01}MO$, c) $LNSm_{0.01}MO$, d) $LNLa_{0.05}MO$, e) $LNNd_{0.05}MO$ and f) $LNSm_{0.05}MO$ powders.

5.4.3 Electrochemical Performance of La, Nd or Sm-doped LNMO Cathode Materials at Room Temperature (RT)

5.4.3.1 Cyclic Voltammetry (CV)

The 1st and the 10th CV curves of "La, Nd and Sm-doped" LNMO samples compared to the parent LNMO sample are shown in Figures 5.57a-d. The electrochemical activities which belong to Mn^{3+}/Mn^{4+} and Ni^{2+}/Ni^{4+} redox couples can also be seen at around 4 V and 4.7 V, respectively, which are still present after 10 cycles.
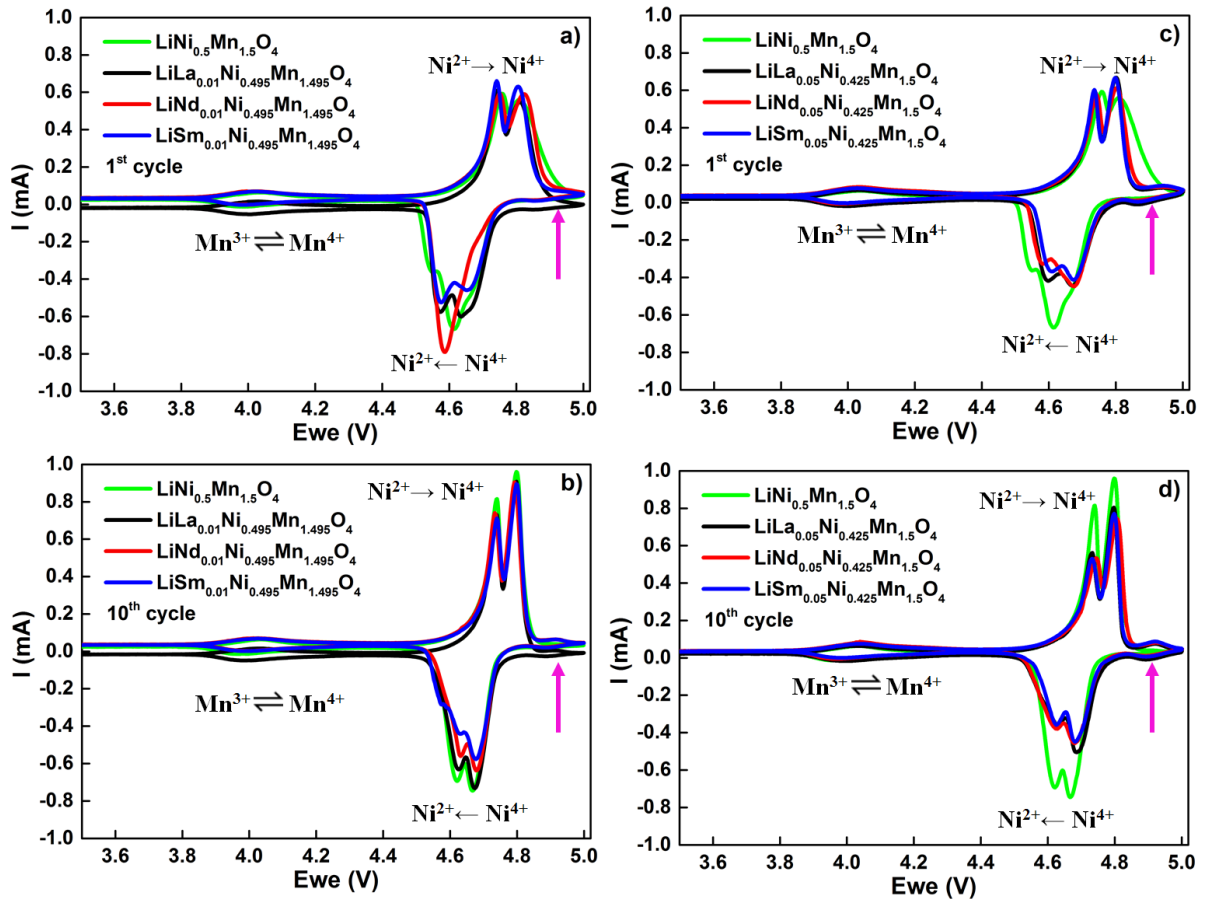
Figure 5.57: Cyclic Voltammograms of 1st cycle and 10th cycle of "La, Nd and Sm-doped" LNMO cathode materials with the scan rate of 0.1 mV s^{-1} in a voltage range 3.5-5.0 V.

The electrochemical test cells were cycled in the voltage range 3.5-5.0 V. No redox

activities are reported in this voltage range for the La, Nd or Sm. However, an additional electrochemical activity is observed at around 4.9 V for all samples pointed with pink arrow most probably due to the parasitic reactions.

5.4.3.2 Cycling Stability

The cycling stability results of the first 300 cycles of "La, Nd and Sm-doped" LNMO compared to undoped LNMO cathodes with a C/2 charge-discharge rate in the voltage window 3.5-5.0 V are shown in Figure 5.58. The initial capacities of $LNLa_{0.01}MO$, $LNNd_{0.01}MO$ and $LNSm_{0.01}MO$ are very close to the LNMO cathode. However, they have a higher capacity retention after 300 cycles. The slightly lower absolute capacities observed for $LNLa_{0.05}MO$, $LNNd_{0.05}MO$ and $LNSm_{0.05}MO$ cathode materials are due to the presence of electrochemically inactive impurity phases which are also included in the calculation of the active material. The capacity retentions after 300 cylces of $LNLa_{0.01}MO$, $LNNd_{0.01}MO$, $LNSm_{0.01}MO$, $LNLa_{0.05}MO$, $LNNd_{0.05}MO$ and $LNSm_{0.05}MO$ cathode materials are 89.2 %, 90.5 %, 88.4 %, 85 %, 85 % and 86 %, respectively, which was 79.5 % for LNMO. The rare earth metals are not present in the main structure, however, the results may indicate that the cycling of the main phase is stabilized by the bimixtures. The distributed impurity phases may contribute to the different mechanism of SEI formation.
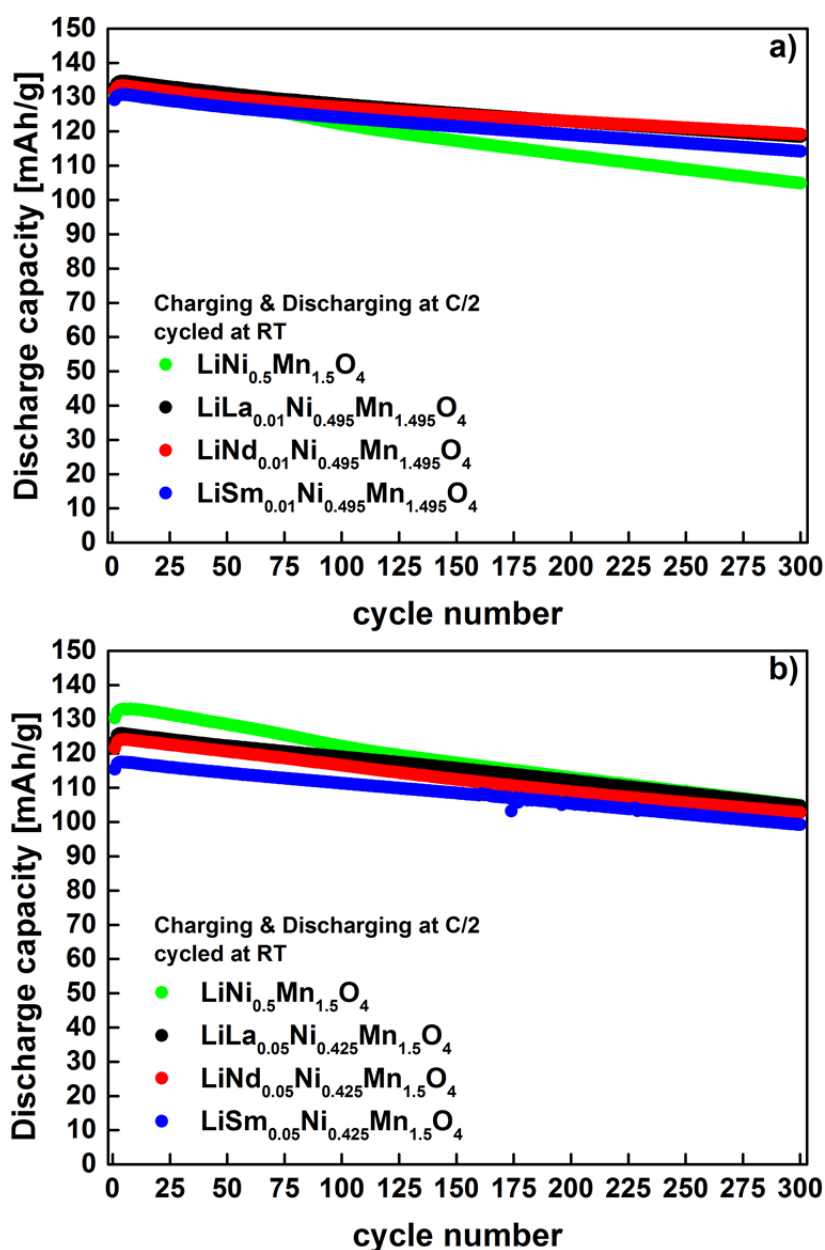
Figure 5.58: Discharge capacity vs. Cycle number plots for "La, Nd and Sm-doped" LNMO cathode materials in a voltage range 3.5-5.0 V at C/2 charge-discharge rate.

5.4.3.3 Rate Capability

The high-rate performance of "rare earth metal doped" LNMO compared to the undoped one is displayed in Figures 5.59a-b. The charging rate was hold constant at C/2 and the discharge rates were varied. The discharge capacities as percentages of the

capacity delivered at C/2 of the samples are also listed in Table 5.15, which shows that the discharge capacities up to 10 C as percentages of the capacity delivered at C/2 for all "rare earth matel doped" samples are very close to each other as well as to undoped LNMO. The compositions $LiNi_{0.495}M_{0.01}Mn_{1.495}O_4$ and $LiNi_{0.425}M_{0.05}Mn_{1.5}O_4$ (M = La, Nd or Sm) exhibited slightly higher rate capability at 20 C than the parent LNMO. The capacity obtained at 20 C is 91 % of the capacity at C/2 for LNMO whereas it is $\geq$94 % for "rare earth-doped" samples.
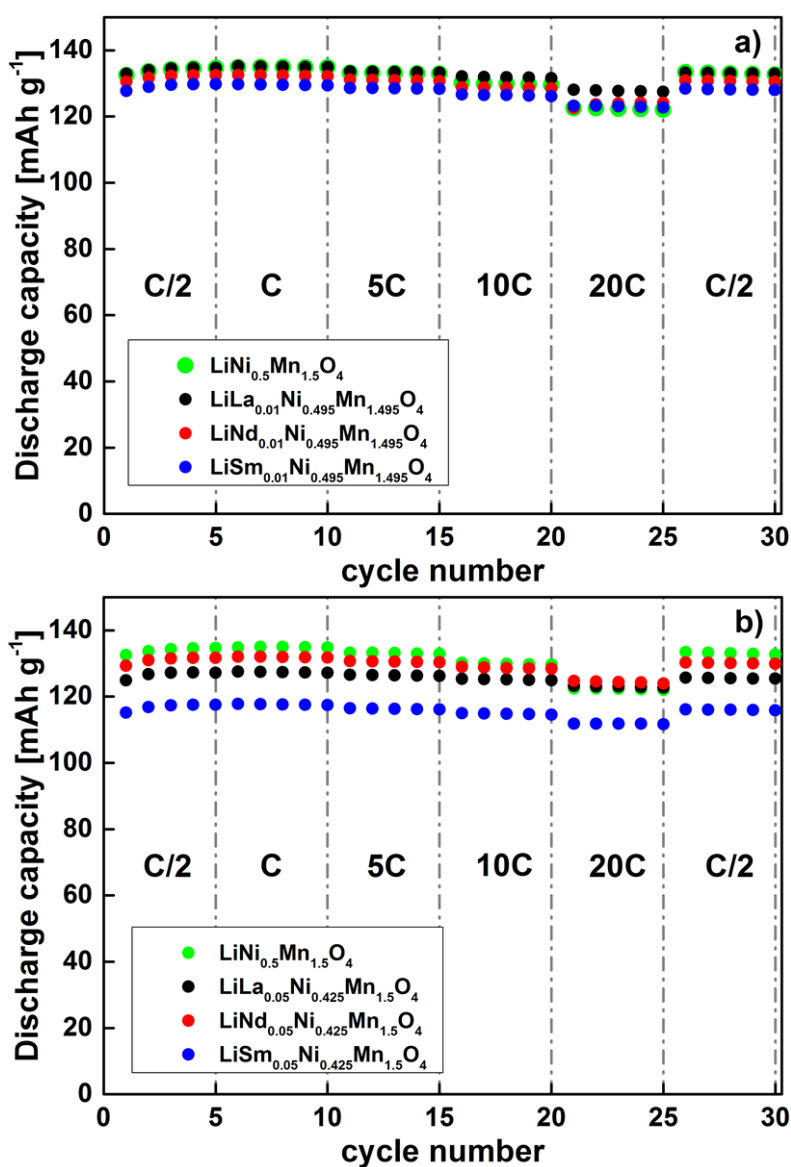
Figure 5.59: Discharge capacity vs. cycle number plots of "La, Nd and Sm-doped" LNMO cathode materials at C/2 charge rate and varied discharge rates.

Sample	Discharge Capacity (mAh g^{-1}) with C/2	The discharge capacity as percentage of the capacity delivered at C/2			
		1C	5C	10C	20C
LNMO	134	100%	99%	97%	91%
LNLa$_{0.01}$MO	134	100%	100%	98.5%	95.5%
LNNd$_{0.01}$MO	132	100%	99.2%	97.7%	94%
LNSm$_{0.01}$MO	130	100%	99.2%	98%	94%
LNLa$_{0.05}$MO	127	100%	99.2%	98.4%	97%
LNNd$_{0.05}$MO	126	100%	100%	98.4%	96%
LNSm$_{0.05}$MO	117	100%	99%	98.3%	96%

Table 5.15: The discharge capacities obtained at different C-rates for "La, Nd and Sm-doped" and undoped LNMO-1000 °C cathode materials.

5.4.4 Investigations on the Structural Evolution of LiNi$_{0.495}$M$_{0.01}$Mn$_{1.495}$O$_4$ and LiNi$_{0.425}$M$_{0.05}$Mn$_{1.5}$O$_4$ (M = La, Nd or Sm) Cathode Materials during Electrochemical Cycling using Synchrotron Diffraction

It is possible that the presence of the impurity phases can influence the electrochemical mechanism by participating in the electrochemical reactions. Although no clear evidence was observed for this behavior from CV experiments, a more reliable method is needed to rule out this possibility.

In order to elucidate the structural changes during the lithium de-/intercalation processes of "La, Nd and Sm-doped" LNMO samples, the cathode materials were cycled at C/2 in the voltage range of 3.5-5.0 V using the *in situ* coin cell setup. The evolution of the structural changes for all samples for selected 2θ regions are shown in Figure 5.60.

The formation of a second spinel phase during both, charging and discharging, is observed for all samples, like in the parent LNMO cathode material. This second phase

was formed reversibly which occured during cycling and disappeared at the end of the discharging process. The LNLa$_{0.01}$MO, LNNd$_{0.01}$MO and LNSm$_{0.01}$MO cathode materials contain 2 % of the La, Nd or Sm containing impurity phases and they are not easy to detect from the diffraction patterns obtained during cycling due to the contribution of additional background from *in situ* coin cell setup. However, the amount of these impurity phases which were obtained in initial powders are more and therefore more visible in the diffraction patterns obtained from the *in situ* coin cells of the LNLa$_{0.05}$MO, LNNd$_{0.05}$MO and LNSm$_{0.05}$MO cathode materials (see Figure 5.60d, e and f). The respective reflections are indicated with red arrows in the graphs. The observation shows that the lattice parameters of these La, Nd or Sm containing impurity phases do not change during cycling. This confirms that these phases have no contribution to the lithium de-/intercalation mechanism which means they are not electrochemically active.
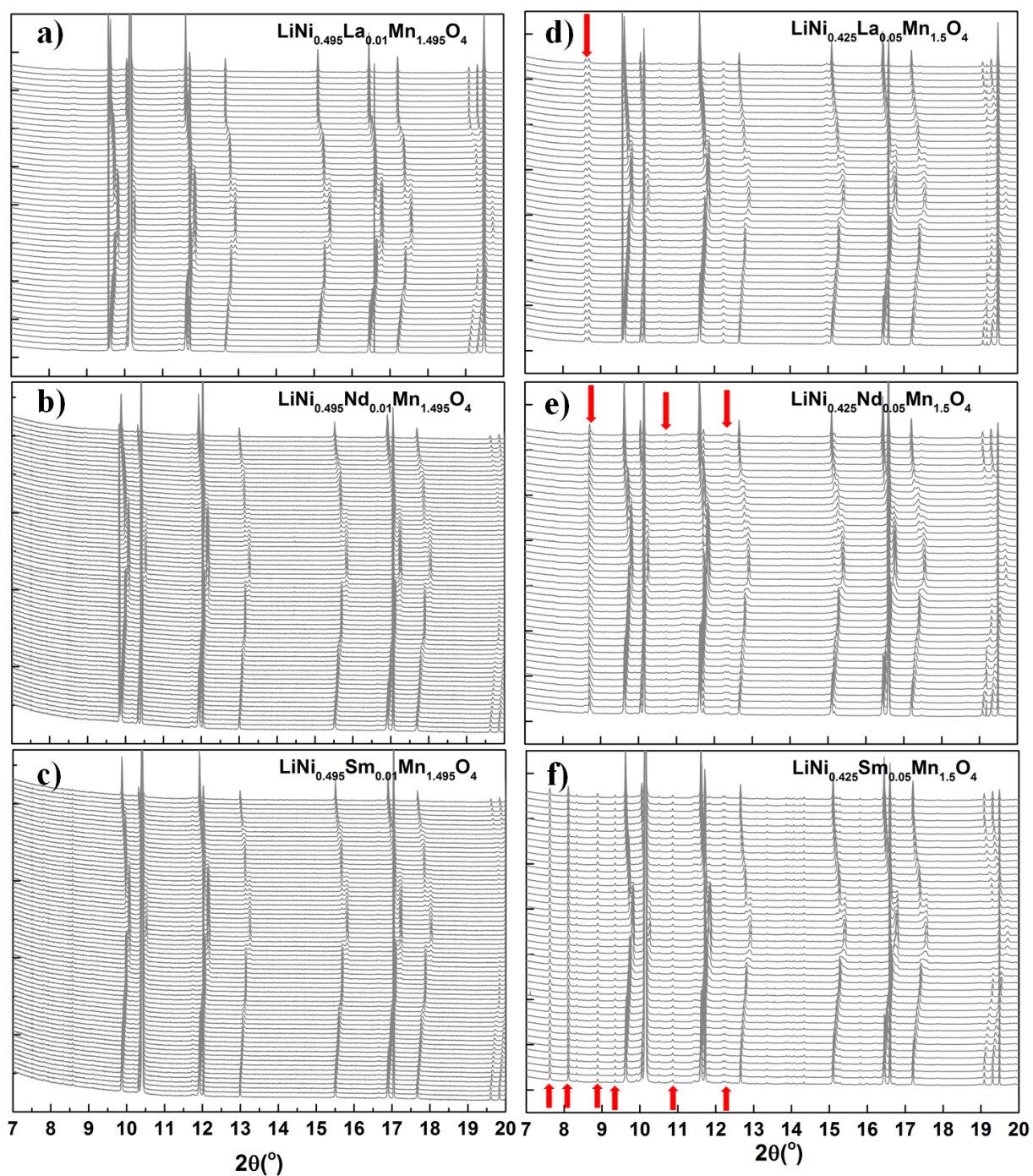
Figure 5.60: The structural evolution obtained during first charge-discharge process for a) $LNLa_{0.01}MO$ b) $LNNd_{0.01}MO$ c) $LNSm_{0.01}MO$ d) $LNLa_{0.05}MO$ e) $LNNd_{0.05}MO$ and f) $LNSm_{0.05}MO$ cathode materials in the voltage range 3.5-5.0 V cycled at C/2 charge-discharge rate.

Chapter 6

Summary and Conclusion

The aim of this work was to investigate the effect of metal ion doping on the structure, electrochemical performance and electrochemical mechanism in the high-voltage $LiNi_{0.5}Mn_{1.5}O_4$ cathode materials. The chosen dopant metals in this work are Ru, Fe, La, Nd and Sm. The Ru and Fe-doped materials were successfully synthesized with a citric acid-assisted sol-gel method. In the case of rare earth metals doping (the incorporation of the dopant cations into the spinel structure) could not be confirmed.

The undoped $LiNi_{0.5}Mn_{1.5}O_4$ samples annealed at 800 °C and 1000 °C crystallize in the cubic spinel structure with $Fd\bar{3}m$ space group. Small amounts of well-kown impurities with rock-salt structure were detected in both samples. Careful synchrotron and neutron diffraction analysis reveals that the impurity phase is not a $Li_zNi_{1-z}O$ phase as it was referred in the literature, but a Ni-rich phase with a stoichiometry Ni_6MnO_8. The LNMO samples synthesized at 1000 °C have superior capacity retention at RT after 300 cycles at C/2 (79.5 %) than the ones synthesized at 800 °C when cycled at the same C-rate (42 %), which is maybe due to a better crystallinity, superior particle morphology and lower surface area available for parasitic reactions. Since the material synthesized at 1000 °C has better performance than the one at 800 °C, cycling stability experiment at elevated temperature was carried out only for LNMO-1000 °C cathode material. Even

though the cycling stability deteriorates at elevated temperature, the LNMO-1000 °C cathode material showed quite a good capacity retention after 225 cycles when it was cycled with C/2 with an initial capacity of ~ 136 mAh g^{-1} and a capacity retention of 75 %. However, increased amount of electrolyte was necessary to achieve such performance.

The formation of impurity phase was suppressed by Ru-doping which indicates the increased tolerance of the structure towards an oxygen loss upon doping. The Ru doping in *16d* sites in the spinel structure was confirmed by neutron diffraction as well as Ru K-edge XAS studies. The amount of Mn^{3+} ions increases in Ru-doped samples comparing to undoped LNMO. The sample synthesized at 1000 °C have better capacity retention at RT after 300 cycles at C/2 (84 %) than the one synthesized at 800 °C when cycled at the same C-rate (8.6 %), as similar to the trend was observed for LNMO samples. LNRMO-1000 °C exhibits excellent electrochemical performances even at high C-rates (10 C and 20 C) compared to the LNMO-1000 °C sample which could be attributed to its high unit cell volume and the presence of additional octahedral vacancies. It shows the highest discharge capacity (136 mAh g^{-1} at 20 C) among the LNMO and LNRMO samples synthesized at both 800 °C and 1000 °C. Additionally the mass loadings of the cathodes significantly affect the delivered capacities especially at high C-rate.

In situ synchrotron powder diffraction shows that LNMO-1000 °C and LNRMO-1000 °C have similar structural evolution during electrochemical cycling. In both materials, Li de-/intercalation takes place via a phase transition mechanism or solid solution reaction depending on compositional range. In the two-phase region, the obtained lattice parameters for the two cubic spinel phases in LNRMO-1000 °C are closer to each other than for the LNMO-1000 °C material. Micro-strain analysis shows that the change in the lattice strain of LNRMO-1000 °C during cycling is less than LNMO-1000 °C which makes the structure more relaxed and helps to enhance the cycling performance.

The doping of Fe is found to suppress the formation of a rock-salt impurity phase, which is often formed during high-temperature synthesis of LNMO. However, neutron diffraction analyses show the existence of additional layered Li_2MnO_3 (*C2/m*) and spinel Fe_3O_4 (*Fd$\bar{3}$m*) phases. NMR and Mössbauer investigations confirm that Fe is incorporated into the spinel structure onto the octahedral sites with oxidation state of +3. According to the neutron diffraction analysis, it has been observed that increasing amount of Fe in LNMO leads to an increase in the amount of Li_2MnO_3 and second Fe containing spinel impurity phases. Among all Fe doped cathodes, the $LNF_{0.2}MO$ has the best capacity retention (92 %) after 300 cycles as well as the highest initial capacity (134 mAh g^{-1}). It is even higher than Ru-doped LNMO. The initial capacity decreases with increasing the amount of Fe in the nominal composition $LiNi_{0.5-x}Fe_{2x}Mn_{1.5-x}O_4$. However, for all Fe substituted samples, the capacity retention is higher than that of parent LNMO-1000 °C sample at RT. Also at high temperature (55 °C), the $LNF_{0.2}MO$ exhibits a higher capacity retention. All Fe-doped samples have superior rate capability performances according to delivered capacities at high C-rates (especially at 10 C and 20 C) compared to capacity delivered at C/2.

In contrast to LNMO and LNRMO the evolution of the Fe-doped spinel structure occurs via solid solution mechanism almost in the entire range of Li-content. However, $LNF_{0.2}MO$ undergoes inhomogeneous Li intercalation/extraction at certain x values (number of moles of Li remaining in the structure) which gives rise to appearance of an additional phase as revealed from the discontinuous behavior of the phase fraction and very small lattice parameter differences of the two phases. The $LNF_{0.2}MO$ material shows a different electrochemical reaction mechanism and an excellent cycling stability in comparison with the LNMO material. The improved kinetics reflected by the smaller difference of the lattice parameters between the two cubic phases and the reduced lattice strain in the structure during electrochemical cycling appears to be the reason for improved cycling stability. The smaller lattice strain seems to be correlated with an increased lattice parameter due to the iron doping. The lattice parameters of

the impurity phases in the Fe-doped samples remain constant throughout the cycling, indicating their electrochemical inactivity.

The neutron diffraction analyses of La, Nd and Sm doped LNMO show that these elements are not inserted inside the spinel structure. However, they form additional La, Nd or Sm containing phases. The existence of these rare earth metal containing bimixtures in the samples lead to broader particle size distribution than that observed for undoped LNMO. The rock salt ($Fm\bar{3}m$) impurity phase exists in all the compositions. According to *in situ* investigations of rare earth elements doped LNMO samples, there is no electrochemically active phase observed besides the main spinel ($Fd\bar{3}m$) phase.

Bibliography

[1] BHASKAR, AISWARYA, NATALIA N. BRAMNIK, ANATOLIY SENYSHYN, HARTMUT FUESS and HELMUT EHRENBERG: *Synthesis, Characterization, and Comparison of Electrochemical Properties of $LiM_{0.5}Mn_{1.5}O_4$ (M=Fe, Co, Ni) at Different Temperatures.* Journal of The Electrochemical Society, 157(6):A689, 2010.

[2] KIZILTAS-YAVUZ, NILÜFER, AISWARYA BHASKAR, DITTY DIXON, MURAT YAVUZ, KRISTIAN NIKOLOWSKI, LI LU, RÜDIGER-A. EICHEL and HELMUT EHRENBERG: *Improving the rate capability of high voltage Lithium-ion battery cathode material $LiNi_{0.5}Mn_{1.5}O_4$ by ruthenium doping.* Journal of Power Sources, 267:533–541, 2014.

[3] KRAYTSBERG, ALEXANDER and YAIR EIN-ELI: *Higher, Stronger, Better... A Review of 5 Volt Cathode Materials for Advanced Lithium-Ion Batteries.* Advanced Energy Materials, 2(8):922–939, 2012.

[4] LEE, EUN-SUNG and ARUMUGAM MANTHIRAM: *Influence of doping on the cation ordering and charge-discharge behavior of $LiMn_{1.5}Ni_{0.5-x}M_xO_4$ (M = Cr, Fe, Co, and Ga) spinels between 5.0 and 2.0 V.* Journal of Materials Chemistry A, 1(9):3118, 2013.

[5] BHASKAR, AISWARYA, DARIA MIKHAILOVA, NILÜFER KIZILTAS-YAVUZ, KRISTIAN NIKOLOWSKI, STEFFEN OSWALD, NATALIA N. BRAMNIK and HELMUT EHRENBERG: *3d-Transition Metal Doped Spinels as High-Voltage Cathode Materials*

for Rechargeable Lithium-Ion Batteries. Progress in Solid State Chemistry, 42(4):128–148, 2014.

[6] WU, P., X.L. ZENG, C. ZHOU, G.F. GU and D.G. TONG: *Improved electrochemical performance of LiNi$_{0.5-x}$Rh$_x$Mn$_{1.5}$O$_4$ cathode materials for 5V lithium ion batteries via Rh-doping.* Materials Chemistry and Physics, 138(2-3):716–723, 2013.

[7] YOON, TAEHO, SANGJIN PARK, JUNYOUNG MUN, JI HEON RYU, WONCHANG CHOI, YOON-SOK KANG, JIN-HWAN PARK and SEUNG M. OH: *Failure mechanisms of LiNi$_{0.5}$Mn$_{1.5}$O$_4$ electrode at elevated temperature.* Journal of Power Sources, 215:312–316, 2012.

[8] MIKHAILOVA, D., A. THOMAS, S. OSWALD, W. GRUNER, N. N. BRAMNIK, A. A. TSIRLIN, D. M. TROTS, A. SENYSHYN, J. ECKERT and H. EHRENBERG: *Structural Changes in the LiCrMnO$_4$ Cathode Material during Electrochemical Li Extraction and Insertion.* Journal of the Electrochemical Society, 160(5):A3082–A3089, 2013.

[9] ZHONG, QIMING, ARMAN BONAKCLARPOUR, MEIJIE ZHANG and J R DAHN: *Synthesis and Electrochemistry of $LiNi_xMn_{2-x}O_4$.* Journal of Electrochemical Society, 144(1):205–2013, 1997.

[10] GU, XIN, XIAOWEI LI, LIQIANG XU, HUAYUN XU, JIAN YANG and YITAI QIAN: *Synthesis of Spinel LiNi$_x$Mn$_{2-x}$O$_4$ (x=0, 0.1, 0.16) and Their High Rate Charge-Discharge Performances.* International Journal of Electrochemical Science, 7:2504–2512, 2012.

[11] PARK, SUNG BIN, WON SOB EOM, WON IL CHO and HO JANG: *Electrochemical properties of LiNi$_{0.5}$Mn$_{1.5}$O$_4$ cathode after Cr doping.* Journal of Power Sources, 159(1):679–684, 2006.

[12] XIONG, LILONG, YOULONG XU, TAO TAO, JIE SONG and JOHN B. GOODENOUGH: *Excellent stability of spinel LiMn$_2$O$_4$-based composites for lithium ion batteries.* Journal of Materials Chemistry, 22(47):24563, 2012.

138

[13] YI, TING-FENG, YING XIE, MING-FU YE, LI-JUAN JIANG, RONG-SUN ZHU and YAN-RONG ZHU: *Recent developments in the doping of LiNi$_{0.5}$Mn$_{1.5}$O$_4$ cathode material for 5 V lithium-ion batteries*. Ionics, 17(5):383–389, 2011.

[14] WANG, HAILONG, HUI XIA, MAN ON LAI and LI LU: *Enhancements of rate capability and cyclic performance of spinel LiNi$_{0.5}$Mn$_{1.5}$O$_4$ by trace Ru-doping*. Electrochemistry Communications, 11(7):1539–1542, 2009.

[15] WANG, HAILONG, TAI AIK TAN, PING YANG, MAN ON LAI and LI LU: *High-Rate Performances of the Ru-Doped Spinel LiNi$_{0.5}$Mn$_{1.5}$O$_4$: Effects of Doping and Particle Size*. The journal of Physical Chemistry, 115:6102–6110, 2011.

[16] LI, S. R., C. H. CHEN and J. R. DAHN: *Studies of LiNi$_{0.5}$Mn$_{1.5}$O$_4$ as a Positive Electrode for Li-Ion Batteries: M^{3+} Doping (M = Al, Fe, Co and Cr), Electrolyte Salts and LiNi$_{0.5}$Mn$_{1.5}$O$_4$/Li$_4$Ti$_5$O$_{12}$ Cells*. Journal of the Electrochemical Society, 160(11):A2166–A2175, 2013.

[17] PARK, S.H., S.-W. OH, S.H. KANG, I. BELHAROUAK, K. AMINE and Y.-K. SUN: *Comparative study of different crystallographic structure of LiNi$_{0.5}$Mn$_{1.5}$O$_{4-\delta}$ cathodes with wide operation voltage (2.0-5.0 V)*. Electrochimica Acta, 52(25):7226–7230, 2007.

[18] TAKAHASHI, KOH, MOTOHARU SAITOH, MITSURU SANO, MIHO FUJITA and KOICHI KIFUNE: *Electrochemical and Structural Properties of a 4.7 V-Class LiNi$_{0.5}$Mn$_{1.5}$O$_4$ Positive Electrode Material Prepared with a Self-Reaction Method*. Journal of The Electrochemical Society, 151(1):A173, 2004.

[19] PASERO, D., N. REEVES, V. PRALONG and A. R. WEST: *Oxygen Nonstoichiometry and Phase Transitions in LiMn$_{1.5}$Ni$_{0.5}$O$_{4-\delta}$*. Journal of The Electrochemical Society, 155(4):A282–A291, 2008.

[20] JULIEN, C. M. and A. MAUGER: *Review of 5-V electrodes for Li-ion batteries: status and trends*. Ionics, 19:951–988, 2013.

[21] KUNDURACI, M. and G. G. AMATUCCI: *The effect of particle size and morphology on the rate capability of 4.7 V LiMn$_{1.5+\delta}$Ni$_{0.5-\delta}$O$_4$ spinel lithium-ion battery cathodes.* Electrochimica Acta, 53:4193–4199, 2008.

[22] ZHONG, G.B., Y.Y. WANG, Y.Q. YU and C.H. CHEN: *Electrochemical investigations of the LiNi$_{0.45}$M$_{0.10}$Mn$_{1.45}$O$_4$ (M=Fe, Co, Cr) 5V cathode materials for lithium ion batteries.* Journal of Power Sources, 205:385–393, 2012.

[23] OH, SI HYOUNG, SANG HOON JEON, WON IL CHO, CHANG SAM KIM and BYUNG WON CHO: *Synthesis and characterization of the metal-doped high-voltage spinel LiNi$_{0.5}$Mn$_{1.5}$O$_4$ by mechanochemical process.* Journal of Alloys and Compounds, 452(2):389–396, 2008.

[24] SHIN, DONG WOOK, CRAIG A BRIDGES, M PARANS PARANTHAMAN and ARUMUGAM MANTHIRAM: *Role of Cation Ordering and Surface Segregation in High-Voltage Spinel LiMn$_{1.5}$Ni$_{0.5-x}$M$_x$O$_4$ (M = Cr, Fe, and Ga) Cathodes for Lithium-Ion Batteries.* Chemistry of Materials, 4(24):3720–3731, 2012.

[25] LIU, JUN and ARUMUGAM MANTHIRAM: *Understanding the Improved Electrochemical Performances of Fe-Substituted 5 V Spinel LiMn$_{1.5}$Ni$_{0.5}$O$_4$.* J.Phys.Chem C, 113(113):15073–15079, 2009.

[26] LIU, JIANHONG, ZHAOQIN SUN, JIAONA XIE, HONGYU CHEN, NINGNING WU and BORONG WU: *Synthesis and electrochemical properties of LiNi$_{0.5-x}$Cu$_x$Mn$_{1.5-y}$Al$_y$O$_4$ (x = 0, 0.05, y = 0, 0.05) as 5 V spinel materials.* Journal of Power Sources, 240:95–100, 2013.

[27] CHEMELEWSKI, KATHARINE R and ARUMUGAM MANTHIRAM: *Origin of Site Disorder and Oxygen Nonstoichiometry in LiMn$_{1.5}$Ni$_{0.5-x}$M$_x$O$_4$ (M = Cu and Zn) Cathodes with Divalent Dopant Ions.* The journal of Physical Chemistry, 4:6–12, 2013.

[28] HONG, KI-JOO and YANG-KOOK SUN: *Synthesis and electrochemical characteristics of LiCr$_x$Ni$_{0.5-x}$Mn$_{1.5}$O$_4$ spinel as 5 V cathode materials for lithium secondary batteries.* Journal of Power Sources, 109:427–430, 2002.

[29] ARUNKUMAR, T and A MANTHIRAM: *Influence of chromium doping on the electrochemical performance of the 5V spinel cathode LiMn$_{1.5}$Ni$_{0.5}$O$_4$.* Electrochimica Acta, 50(28):5568–5572, 2005.

[30] OH, SI HYOUNG, KYUNG YOON CHUNG, SANG HOON JEON, CHANG SAM KIM, WON IL CHO and BYUNG WON CHO: *Structural and electrochemical investigations on the LiNi$_{0.5-x}$Mn$_{1.5-y}$M$_{x+y}$O$_4$ (M=Cr, Al, Zr) compound for 5V cathode material.* Journal of Alloys and Compounds, 469(1-2):244–250, 2009.

[31] LOCATI, C., U. LAFONT, L. SIMONIN, F. OOMS and E.M. KELDER: *Mg-doped LiNi$_{0.5}$Mn$_{1.5}$O$_4$ spinel for cathode materials.* Journal of Power Sources, 174(2):847–851, 2007.

[32] KIM, HYUN-JU, BONG-SOO JIN, CHIL-HOON DOH, DONG-SIK BAE and HYUN-SOO KIM: *Improved electrochemical performance of doped-LiNi$_{0.5}$Mn$_{1.5}$O$_4$ cathode material for lithium-ion batteries.* Electronic Materials Letters, 9(6):851–854, 2013.

[33] SINGHAL, RAHUL, MAHARAJ S. TOMAR, SUPREM R. DAS, JUAN G. BURGOS, SURINDER P. SINGH, ARUN KUMAR and RAM S. KATIYAR: *Li-Ion Rechargeable Battery with LiMn$_{1.5}$Ni$_{0.46}$Rh$_{0.04}$O$_4$ Spinel Cathode Material.* Electrochemical and Solid-State Letters, 10(7):A163–A165, 2007.

[34] ZHONG, G.B., Y.Y. WANG, X.J. ZHAO, Q.S. WANG, Y. YU and C.H. CHEN: *Structural, electrochemical and thermal stability investigations on LiNi$_{0.5-x}$Al$_{2x}$Mn$_{1.5-x}$O$_4$ ($0\leq 2x\leq 1.0$) as 5 V cathode materials.* Journal of Power Sources, 216:368–375, 2012.

[35] REDDY, M. V., S. SUNDAR MANOHARAN, JIMMY JOHN, BRAJENDRA SINGH, G. V. SUBBA RAO and B. V. R. CHOWDARI: *Synthesis, Characterization, and Electrochemi-*

cal Cycling Behavior of the Ru-Doped Spinel, LiMn$_{2x}$Ru$_x$O$_4$ (x=0, 0.1, and 0.25). Journal of The Electrochemical Society, 156(8):A652, 2009.

[36] YI, TING-FENG, YING XIE, YAN-RONG ZHU, RONG-SUN ZHU and MING-FU YE: *High rate micron-sized niobium-doped LiMn$_{1.5}$Ni$_{0.5}$O$_4$ as ultra high power positive-electrode material for lithium-ion batteries*. Journal of Power Sources, 211:59–65, 2012.

[37] JANG, MIN-WOO, HUN-GI JUNG, BRUNO SCROSATI and YANG-KOOK SUN: *Improved Co-substituted, LiNi$_{0.5-x}$Co$_{2x}$Mn$_{1.5-x}$O$_4$ lithium ion battery cathode materials*. Journal of Power Sources, 220:354–359, 2012.

[38] LE, MY-LOAN-PHUNG, PIERRE STROBEL, FANNIE ALLOIN and THIERRY PAGNIER: *Influence of the tetravalent cation on the high-voltage electrochemical activity of LiNi$_{0.5}$Mn$_{1.5}$O$_4$ spinel cathode materials*. Electrochimica Acta, 56(1):592–599, 2010.

[39] BHASKAR, AISWARYA, WOLFGANG GRUNER, DARIA MIKHAILOVA and HELMUT EHRENBERG: *Thermal stability of Li$_{1-\Delta}$M$_{0.5}$Mn$_{1.5}$O$_4$ (M = Fe, Co, Ni) cathodes in different states of delithiation Δ*. RSC Advances, 4:5909–5916, 2013.

[40] MO, MINGYUE, K.S. HUI, XIAOTING HONG, JUNSHENG GUO, CHENGCONG YE, AIJU LI, NANQIAN HU, ZHENZE HUANG, JIANHUI JIANG, JINGZHI LIANG and HONGYU CHEN: *Improved cycling and rate performance of Sm-doped LiNi$_{0.5}$Mn$_{1.5}$O$_4$ cathode materials for 5V lithium ion batteries*. Applied Surface Science, 290:412–418, 2014.

[41] LIU, H., Y. P. WU, E. RAHM, R. HOLZE and H. Q. WU: *Cathode materials for lithium ion batteries prepared by sol-gel methods*. Journal of Solid State Electrochemistry, 8(7):450–466, 2004.

[42] RODRIGUEZ-CARVAJAL, JUAN: *Recent advances in magnetic structure determination neutron powder diffraction*. Physica B, 192:55–69, 1993.

[43] PECHARSKY, VITALIJ K. and PETER Y. ZAVALIJ: *Fundamentals of Powder Diffraction and Structural Characterization of Materials*. Kluwer Academic Publishers, Norwell, Massachusetts, 2003.

[44] HAMMERSLEY, A. P., S. O. SVENSSON, M. HANFLAND, A. N. FITCH and D. HAUSERMANN: *Two-dimensional detector software: From real detector to idealised image or two-theta scan*. High Pressure Research, 14(4-6):235–248, 1996.

[45] FAUTH, F., I. PERAL, C. POPESCU and M. KNAPP: *The new Material Science Powder Diffraction beamline at ALBA Synchrotron*. JCPDS-ICDD, 28:360–370, 2013.

[46] TILLEY, RICHARD J. D.: *Crystals and Crystal Structures*. John Willey and Sons, LTD, England, 2006.

[47] HOELZEL, M., A. SENYSHYN, N. JUENKE, H. BOYSEN, W. SCHMAHL and H. FUESS: *High-resolution neutron powder diffractometer SPODI at research reactor FRM II*. Nuclear Instruments and Methods in Physics Research Section A: Accelerators, Spectrometers, Detectors and Associated Equipment, 667:32–37, 2012.

[48] BUNKER, GRANT: *Introduction to XAFS, A Practical Guide to X-ray Absorption Fine Structure Spectroscopy*. Cambridge University Press, The Edinburgh Building, Cambridge, UK, 2010.

[49] RAVEL, B and M NEWVILLE: *ATHENA, ARTEMIS, HEPHAESTUS: data analysis for X-ray absorption spectroscopy using IFEFFIT*. Journal of synchrotron radiation, 12(Pt 4):537–41, 2005.

[50] MENIL, FRANCIS: *Systematic Trends of the ^{57}Fe Moessbauer Isomer Shifts in (FeO_n) and (FeF_n) Polyhedra*. Journal of Physics and Chemistry of Solids, 46(7):763–789, 1985.

[51] HEITJANS, PAUL and SYLVIO INDRIS: *Diffusion and ionic conduction in nanocrystalline ceramics*. Journal of Physics: Condensed Matter, 15:R1257–R1289, 2003.

[52] P. HEITJANS, A. SCHIRMER, S. INDRIS: *Chapter in Diffusion in Condensed Matter - Methods, Materials: NMR and -NMR Studies of Diffusion in Interface-Dominated and Disordered Solids.* Springer, Berlin, 2005.

[53] DUER, M. J.: *Introduction to Solid-State NMR Spectroscopy.* Blackwell Publishing, Oxford, 2004.

[54] GREY, CLARE P. and YOUNG JOO LEE: *Lithium MAS NMR studies of cathode materials for lithium-ion batteries.* Solid State Sciences, 5(6):883–894, 2003.

[55] GREY, CLARE P and NICOLAS DUPRÉ: *NMR studies of cathode materials for lithium-ion rechargeable batteries.* Chemical reviews, 104(10):4493–512, 2004.

[56] YANG, HUI, GUORONG V. ZHUANG and PHILIP N. ROSS: *Thermal stability of $LiPF_6$ salt and Li-ion battery electrolytes containing $LiPF_6$.* Journal of Power Sources, 161(1):573–579, 2006.

[57] GNANARAJ, J. S., E. ZINIGRAD, L. ASRAF, H. E. GOTTLIEB, M. SPRECHER, M. SCHMIDT, W. GEISSLER and D. AURBACH: *A Detailed Investigation of the Thermal Reactions of $LiPF_6$ Solution in Organic Carbonates Using ARC and DSC.* Journal of The Electrochemical Society, 150(11):A1533, 2003.

[58] HERKLOTZ, MARKUS, FRIEDER SCHEIBA, MANUEL HINTERSTEIN, KRISTIAN NIKOLOWSKI, MICHAEL KNAPP, ANN-CHRISTIN DIPPEL, LARS GIEBELER, JÜRGEN ECKERT and HELMUT EHRENBERG: *Advances in in situ powder diffraction of battery materials: a case study of the new beamline P02.1 at DESY, Hamburg.* Journal of Applied Crystallography, 46(4):1117–1127, 2013.

[59] TERADA, YASUKO, KENJI YASAKA, FUMISHIGE NISHIKAWA, TOKUZO KONISHI, MASAKI YOSHIO and IZUMI NAKAI: *In Situ XAFS Analysis of $Li(Mn, M)_2O_4$ (M=Cr, Co, Ni) 5V Cathode Materials for Lithium-Ion Secondary Batteries.* Journal of Solid State Chemistry, 156(2):286–291, 2001.

[60] KIM, J.-H., C. S. YOON, S.-T. MYUNG, JAI PRAKASH and Y.-K. SUN: *Phase Transitions in Li$_{1-\delta}$Ni$_{0.5}$Mn$_{1.5}$O$_4$ during Cycling at 5 V*. Electrochemical and Solid-State Letters, 7(7):A216, 2004.

[61] SUN, YANYAN, YIFU YANG, HUI ZHAN, HUIXIA SHAO and YUNHONG ZHOU: *Synthesis of high power type LiMn$_{1.5}$Ni$_{0.5}$O$_4$ by optimizing its preparation conditions.* Journal of Power Sources, 195(13):4322–4326, 2010.

[62] SHANNON, R. D.: *Revised Effective Ionic Radii and Systematic Studies of Interatomie Distances in Halides and Chaleogenides*. Acta Crystallographica Section A Foundations of Crystallography, 32:751, 1976.

[63] LIU, G. Q., L. WEN and Y. M. LIU: *Spinel LiNi$_{0.5}$Mn$_{1.5}$O$_4$ and its derivatives as cathodes for high-voltage Li-ion batteries*. Journal of Solid State Electrochemistry, 14(12):2191–2202, 2010.

[64] SHA, OU, ZHI QIAO, SHAOLIANG WANG, ZHIYUAN TANG, HAO WANG, XINHE ZHANG and QIANG XU: *Improvement of cycle stability at elevated temperature and high rate for LiNi0.5xCuxMn1.5O4 cathode material after Cu substitution*. Materials Research Bulletin, 48(4):1606–1611, 2013.

[65] LIU, DONGQIANG, YUHAO LU and JOHN B. GOODENOUGH: *Rate Properties and Elevated-Temperature Performances of LiNi0.5xCr2xMn1.5xO4 (02x0.8) as 5 V Cathode Materials for Lithium-Ion Batteries*. Journal of The Electrochemical Society, 157(11):A1269–A1273, 2010.

[66] KIM, JUNG-HYUN, NICHOLAS P.W. PIECZONKA, ZICHENG LI, YAN WU, STEPHEN HARRIS and BOB R. POWELL: *Understanding the capacity fading mechanism in LiNi$_{i0.5}$Mn$_{1.5}$O$_4$/graphite Li-ion batteries*. Electrochimica Acta, 90:556–562, 2013.

[67] WANG, LI-FANG, CHIN-CHING OU, KATHRYN A. STRIEBEL and JENN-SHING CHEN: *Study of Mn Dissolution from LiMn$_2$O$_4$ Spinel Electrodes Using Rotating Ring-*

Disk Collection Experiments. Journal of The Electrochemical Society, 150(7):A905, 2003.

[68] RANA, JATINKUMAR, SVEN GLATTHAAR, HOLGER GESSWEIN, NEERAJ SHARMA, JOACHIM R. BINDER, ROMAN CHERNIKOV, GERHARD SCHUMACHER and JOHN BANHART: *Local structural changes in LiMn$_{1.5}$Ni$_{0.5}$O$_4$ spinel cathode material for lithium-ion batteries.* Journal of Power Sources, 255:439–449, 2014.

[69] BHASKAR, AISWARYA, STEFFEN KRUEGER, VASSILIOS SIOZIOS, JIE LI, SASCHA NOWAK and MARTIN WINTER: *Synthesis and Characterization of High-Energy, High-Power Spinel-Layered Composite Cathode Materials for Lithium-Ion Batteries.* Advanced Energy Materials, November 2014.

[70] OHZUKU, TSUTOMU, KINGO ARIYOSHI, SACHIO TAKEDA and YOICHI SAKAI: *Synthesis and characterization of 5 V insertion material of LiFe$_y$Mn$_{2y}$O$_4$ for lithium-ion batteries.* 46:2327–2336, 2001.

[71] ALCÁNTARA, R, M. JARABA, P. LAVELA, J.L. TIRADO, J.C. JUMAS and J.OLIVER FOURCADE: *Changes in oxidation state and magnetic order of iron atoms during the electrochemical reaction of lithium with NiFe$_2$O$_4$.* Electrochemistry Communications, 5:16–21, 2003.

[72] ALCÁNTARA, R., M. JARABA, P. LAVELA, J.L. TIRADO, J.C. JUMAS and J. OLIVIER FOURCADE: *^{57}Fe Mössbauer spectroscopy and surface modification with zinc and magnesium of LiCo$_{0.8}$Fe$_{0.2}$MnO$_4$ 5V electrodes.* Journal of Power Sources, 135(1-2):281–285, 2004.

[73] PERMIEN, STEFAN, HOLGER HAIN, MARCO SCHEUERMANN, STEFAN MANGOLD, VALERIU MEREACRE, ANNIE K. POWELL, SYLVIO INDRIS, ULRICH SCHÜRMANN, LORENZ KIENLE, VIOLA DUPPEL, SVENJA HARM and WOLFGANG BENSCH: *Electrochemical insertion of Li into nanocrystalline MnFe$_2$O$_4$: a study of the reaction mechanism.* RSC Advances, 3(45):23001, 2013.

[74] OH, SEI J, D. C COOK and H.E. TOWNSEND: *Characterization of iron oxides commonly formed as corrosion products on steel.* 112:59–65.

[75] CABANA, JORDI, FREDRICK O OMENYA, NATASHA A CHERNOVA, DONGLI ZENG, M STANLEY WHITTINGHAM and CLARE P GREY: *Composition-Structure Relationships in the Li-Ion Battery Electrode Material LiNi$_{0.5}$Mn$_{1.5}$O$_4$.* Chemistry of Materials, 24:2952–2964, 2012.

[76] FEY, G: *Preparation and electrochemical properties of high-voltage cathode materials, LiM$_y$Ni$_{0.5-y}$Mn$_{1.5}$O$_4$ (M=Fe, Cu, Al, Mg; y=0.00.4).* Journal of Power Sources, 115(2):332–345, 2003.

[77] YAVUZ, MURAT, NILÜFER KIZILTAS-YAVUZ, AISWARYA BHASKAR, MARCO SCHEUERMANN, SYLVIO INDRIS, FRANCOIS FAUTH, MICHAEL KNAPP and HELMUT EHRENBERG: *Influence of Iron on the Structural Evolution of LiNi$_{0.4}$Fe$_{0.2}$Mn$_{1.4}$O$_4$ during Electrochemical Cycling Investigated by in situ Powder Diffraction and Spectroscopic Methods.* Zeitschrift für anorganische und allgemeine Chemie (ZAAC), page doi: 10.1002/zaac.201400247.

[78] BHASKAR, AISWARYA, NATALIA N. BRAMNIK, DMYTRO M. TROTS, HARTMUT FUESS and HELMUT EHRENBERG: *In situ synchrotron diffraction study of chargedischarge mechanism of solgel synthesized LiM$_{0.5}$Mn$_{1.5}$O$_4$ (M=Fe, Co).* Journal of Power Sources, 217:464–469, 2012.

[79] ZENG, ZHIPENG, HAILEI ZHAO, JIE WANG, PENGPENG LV, TIANHOU ZHANG and QING XIA: *Nanostructured Fe$_3$O$_4$@C as anode material for lithium-ion batteries.* Journal of Power Sources, 248:15–21, 2014.

Acknowledgement

Curriculum Vitae

Personal Information

Name: Nilüfer

Surname: KIZILTAŞ-YAVUZ

Date of Birth: 31/05/1985

Place of Birth: Ankara, Turkey

Nationality: Turkish

Marital Status: Married

Education

10/2011–04/2015 **Karlsruhe Institute of Technology (KIT)**, *Karlsruhe, Germany, PhD at the department of Inorganic Chemistry and at Institute of Applied Materials-Energy Storage Systems (IAM-ESS)*

10/2009–04/2011 **Technical University of Munich (TUM), University of Munich (LMU) and University of Augsburg** *Munich, Germany, Master of Advanced Materials Science (AMS), Masters Course of the Elite Network of Bavaria*

09/2003–06/2008 **Ankara University** *Ankara, Turkey, Bachelor at the department of*

Physics Engineering

Academic Experience

10/2012-present **Karlsruhe Institute of Technology (KIT) / Institute of Applied Materials-Energy Storage Systems (IAM-ESS)**, *Karlsruhe, Germany, (Research Associate)*

10/2011–10/2012 **Technical University of Darmstadt-Collaborative Research Center (SFB) 595** *Darmstadt, Germany, Project: Electrical Fatigue of Functional Materials (One Year Doctoral Scholarship)*

10/2010–06/2011 **Leibniz Institute for Solid State and Materials Research Dresden (IFW)** *Dresden, Germany, Project : Investigation and Characterization of Functional Oxide Materials for High-Energy Li-ion Batteries (Master's Thesis Research)*

08/2010–10/2010 **Leibniz Institute for Solid State and Materials Research Dresden (IFW)** *Dresden, Germany, Project : Degradation of functional materials in high-power Li-ion batteries ((Eight weeks Training, a part of master program)*

09/2007–01/2008 **Ankara University** *Ankara, Turkey, Project : Atomic Force Microscopy and Magnetic Force Microscopy (Bachelor's Thesis Research)*

07/2007–08/2007 **Helmholtz-Zentrum Dresden-Rossendorf (HZDR)** *Dresden, Germany, Institute of Ion Beam Physics and Materials Research (2 months Graduation Training)*

Practical Experience

09/2011–Present **Synchrotron Diffraction Experiments at different Beam lines** *DESY (Hamburg) ; ESRF and ILL (Grenoble) ; ALBA (Barcelona)*

09/2012 **European Synchrotron Radiation Facility (ESRF) and Institut Lau-Langevin (ILL**, *Grenoble, France, HERCULES (**H**igher **E**uropean **R**esearch **C**ourse for **U**sers of **L**arge **E**xperimental **S**ystems) Specialised Course on Neutrons and Synchrotron Radiation in Materials for Energy (HSC14) (One week). Poster Presentation: PDF Experiments and In-situ Investigations of Li-ion Battery Electrode Materials; Murat Yavuz, Nilufer K. Yavuz, Kristian Nikolowski, Michael Knapp, Helmut Ehrenberg.*

02/2010–03/2010 **Unternehmer TUM, Technical University of Munich**, *Munich, Germany, Business Planning and Prototyping (Two weeks Spring School)*

Scientific Publications

✓ **N. Kiziltas-Yavuz**, *M. Herklotz, A. M. Hashem, H. M. Abuzeid, B. Schwarz, H. Ehrenberg, A. Mauger, C. M. Julien; Synthesis, structural, magnetic and electrochemical properties of* $LiNi_{1/3}Mn_{1/3}Co_{1/3}O_2$ *prepared by a solgel method using table sugar as chelating agent, Electrochimica Acta, 113 (2013) 313-321.*

✓ *A.Bhaskar, D. Mikhailova,* **N. Kiziltas-Yavuz**, *K. Nikolowski, S. Oswald, N. N. Bramnik, H. Ehrenberg; 3d-Transition Metal Doped Spinels as High-Voltage Cathode Materials for Rechargeable Lithium-Ion Batteries, Progress in Solid State Chemistry (PSSC), 42 (2014) 128-148.*

✓ **N. Kiziltas-Yavuz**, *A.Bhaskar, Ditty Dixon, Murat Yavuz, K.Nikolowski, L. Lu, R.-A. Eichel, H. Ehrenberg; Improving the rate capability of high voltage lithium-ion battery cathode material* $LiNi_{0.5}Mn_{1.5}O_4$ *by ruthenium doping, Journal of Power Sources, 267 (2014) 533-541.*

✓ *M. Yavuz,* **N. Kiziltas-Yavuz**, *A.Bhaskar, M.Scheuermann, S.Indris, F.Fauth, M.Knapp, H. Ehrenberg; Influence of Fe on the structural evolution of* $LiNi_{0.4}Fe_{0.2}Mn_{1.4}O_4$ *during electrochemical cycling investigated by in situ powder*

diffraction and spectroscopic methods, Zeitschrift für Anorganische und Allgemeine Chemie, 640 (2014) 3118- 3126.

Declaration

Hiermit erkläre ich, dass ich die Arbeit selbständig angefertigt und keine anderen als die angegebenen Quellen und Hilfsmittel benutzt sowie die wörtlich oder inhaltlich übernommenen Stellen als solche kenntlich gemacht und die Satzung der Universität Karlsruhe (TH) zur Sicherung guter wissenschaftlicher Praxis in der jeweils gültigen Fassung beachtet habe.

Karlsruhe, den 02.03.2015

M. Sc. Nilüfer KIZILTAŞ-YAVUZ

I hereby declare that I have made this work independently and used no other than the specified sources and tools, as well as, whether verbatim or with regards to content, indicated all citations as such and I have paid attention to the statute of the University of Karlsruhe (TH) in the current version to ensure good scientific practice.

Karlsruhe, 02.03.2015

M. Sc. Nilüfer KIZILTAŞ-YAVUZ

KIT

Karlsruhe Institute of Technology

Influence of M- doping (M= Ru, Fe, La, Nd, Sm) on the Performance of Lithium Nickel-Manganese Spinels as High-Voltage Cathode Materials for Lithium Ion Batteries

Nilüfer KIZILTAŞ-YAVUZ

Faculty of Chemistry and Biosciences - Institute of Inorganic Chemistry

Institute of Applied Materials (IAM) - Institute of Energy Storage Systems (ESS)

Karlsruhe, 2015